LWR Fuel Reactivity Depletion Verification Using 2D Full Core MOC and Flux Map Data

by

Geoffrey Alexander Gunow

B.S.E., University of Michigan (2012)

Submitted to the Department of Nuclear Science and Engineering
in partial fulfillment of the requirements for the degree of

Master of Science in Nuclear Science and Engineering

at the

MASSACHUSETTS INSTITUTE OF TECHNOLOGY

February 2015

Author .... Signature redacted ....
Department of Nuclear Science and Engineering
January 9, 2015

Certified by.... Signature redacted ....
Kord Smith
KEPCO Professor of the Practice of Nuclear Science and Engineering
Thesis Supervisor

Certified by....... Signature redacted ....
Benoit Forget
Associate Professor of Nuclear Science and Engineering
Thesis Supervisor

Accepted by .... Signature redacted ....
Mujid S. Kazimi
TEPCO Professor of Nuclear Engineering
Chairman, Committee on Graduate Students

LWR Fuel Reactivity Depletion Verification Using 2D Full Core MOC and Flux Map Data

by

Geoffrey Alexander Gunow

Submitted to the Department of Nuclear Science and Engineering
on January 9, 2015, in partial fulfillment of the
requirements for the degree of
Master of Science in Nuclear Science and Engineering

Abstract

Experimental quantification of PWR fuel reactivity burnup decrement biases and uncertainties using in-core flux map data from operating power reactors has previously been conducted employing analytical methods to systematically determine experimental fuel reactivities that best match measured fission rate distributions. This optimal core reactivity distribution that best matches the measured fission rate distribution is assumed to be associated with the true fuel reactivity distribution. Some parties have questioned whether fortuitous cancellation of errors between various approximations inherent in the 3D nodal diffusion core analysis models might have caused reactivity decrement biases and uncertainties to be unrealistically small. In this study, the BEAVRS benchmark is modeled with both 2D, full-core, multi-group transport calculations and 2D and 3D nodal diffusion calculations. The calculated reaction rates are compared with measured in-core detector reaction rates supplied in the benchmark. These models are used in conjunction with analytical methods to obtain fuel reactivity biases and uncertainties. Results demonstrate that fuel batch reactivities inferred from flux map data using full-core transport calculations are nearly identical to those inferred using nodal diffusion calculations. Consequently, nodal methods do not contribute significantly to reactivity decrement biases. Fuel reactivity biases and uncertainties inferred from 3D nodal diffusion calculations remain valid.

Thesis Supervisor: Kord Smith
Title: KEPCO Professor of the Practice of Nuclear Science and Engineering

Thesis Supervisor: Benoit Forget
Title: Associate Professor of Nuclear Science and Engineering

Acknowledgments

I am very grateful for the excellent guidance and support of my research advisors Professor Kord Smith and Professor Benoit Forget throughout this research and my own personal academic career. I would also like to thank everyone at Studsvik Scandpower for their hospitality and providing the computational resources and assistance to complete this research. I would like to acknowledge the tremendous work accomplished by Nick Horelik and Bryan Herman in compiling the BEAVRS benchmark which made this work possible. I would like to personally thank Koroush Shirvan for his help in developing the SIMULATE-3 models used in this study which were particularly helpful at the beginning of this research.

This work was supported by the Electric Power Research Institute and Nuclear Energy University Programs (NEUP) under the graduate fellowship program.

Contents

List of Figures

List of Tables

Chapter 1

Introduction

1.1 Motivation

Spent fuel pool (SFP) and cask criticality analyses rely on lattice physics codes to predict nuclide inventories of spent fuel assemblies. Current procedures follow the guidance of the 1998 NRC "Kopp Memo" [1] which instructs analysts to use 5 % of computed fuel delta-k reactivity decrement to account for uncertainties. These uncertainties could arise from many sources, most notably uncertainties in predicted nuclide number densities and fundamental neutron cross sections. Recently the NRC has requested justification for use of the Kopp Memo with respect to SFP criticality.

In a 2011 EPRI-sponsored study [2], an experimental quantification of PWR fuel reactivity burnup decrement biases and uncertainties was conducted. The investigation utilized the Studsvik CMS suite along with measured data from 44 PWR operating cycles. The comparison of simulated core behavior using SIMULATE-3 with measured fission reaction rates provided a framework to infer fuel assembly reactivity and thus infer biases and uncertainties. The report concluded that the resulting uncertainties in measured HFP sub-batch reactivity decrement errors are less than 250 pcm for burnups up to 55 GWd/T. Therefore, the authors assert that the 5% uncertainty assumption is both valid and conservative for cold SFP criticality calculations.

Some have questioned the validity of the conclusions from the EPRI-sponsored study due to assumptions inherent to nodal methods which are utilized in SIMULATE-3. In this investigation we aim to determine the magnitude of any bias introduced by nodal methods by comparing nodal method solutions with fine spatial mesh, multi-group transport solutions which do not incorporate assumptions inherent to nodal methods.

1.2 Outline of Standard Full-Core Modeling Procedure

The EPRI-sponsored study mentioned above utilized what has become the standard full-core modeling procedure for reactor physics. In this process, first a standard library of many-group cross sections are formed. CASMO, the lattice physics code used in the Studsvik CMS suite [5] utilizes a 495 group cross section library that is pre-generated using the NJOY code [13]. This library contains cross section information for each isotope for various temperatures and background cross sections. Using this library, lattice physics calculations are performed and cross sections are condensed to a few groups.

This few-group cross section library is used to solve the neutron transport problem over the specified geometry. It is common practice to solve for each unique assembly type loaded into the core. This problem is typically solved in two dimensions using a transport method, such as the method of characteristics (MOC) used in CASMO. Although the lattice physics codes are used to solve only for single assemblies, the transport methods are very general and in theory can be used for full-core calculations as well. Due to computational constraints, solving full-core problems with MOC is not common. Instead, each unique assembly is simulated at a variety of reactor conditions by varying parameters such as fuel temperature, moderator temperature, and boron concentration. The resulting solutions are used to condense accurate two group cross sections and assembly discontinuity factors (ADFs) to be used by a nodal code. Nodal codes interpolate the case matrix to determine appropriate cross sections for use with the local reactor conditions. Due to the extremely coarse mesh associated with nodal methods, the calculation time is orders of magnitude less than MOC. Therefore, this procedure requires only solving many MOC calculations on a much smaller domain. Then full-core problems are solved with a computationally fast nodal simulator allowing proper core analysis (which involves many full-core depletion calculations) to become tractable.

Although the immense reduction in computation requirements allowed by nodal methods are desirable, nodal methods do introduce a variety of assumptions and approximations. Most notably, in this analysis, nodal methods rely on two-group cross sections which might not fully describe neutronic behavior with the desired fidelity. In this investigation we compare solutions calculated with nodal methods to those calculated with full-core MOC multi-group transport models to determine the magnitude of errors introduced by nodal methods, specifically as it relates to fuel assembly reactivity. To better understand the background of this investigation, it is helpful to have a basic understanding of MOC and nodal methods.

1.3 Description of the Method of Characteristics (MOC)

This section serves as a brief introduction to the method of characteristics (MOC) and follows the derivation given in Boyd's thesis [3]. Readers interested in the finer details of MOC and it's underlying assumptions should refer to the thesis.

MOC is a common method of solving partial differential equations. In particular, we apply this method to solving the Boltzmann form of the neutron transport equation given in Eq. 1.1. This equation characterizes the behavior of neutrons in a reactor with few assumptions. The assumptions that are made such as isotropic emission of fission neutrons and no neutron-neutron collisions are deeply rooted in physical theory as well as observation.

$$
\begin{aligned}
&\boldsymbol{\Omega} \cdot \nabla \Psi(\mathbf{r}, \boldsymbol{\Omega}, E) + \Sigma^T(\mathbf{r}, E)\Psi(\mathbf{r}, \boldsymbol{\Omega}, E) \\
&= \int_0^\infty \mathrm{d}E' \int_{4\pi} \mathrm{d}\boldsymbol{\Omega}' \Sigma^S(\mathbf{r}, \boldsymbol{\Omega}' \to \boldsymbol{\Omega}, E' \to E)\Psi(\mathbf{r}, \boldsymbol{\Omega}', E') \\
&\quad + \frac{\chi(\mathbf{r}, E)}{4\pi k_{eff}} \int_0^\infty \mathrm{d}E' \nu \Sigma^F(\mathbf{r}, E') \int_{4\pi} \mathrm{d}\boldsymbol{\Omega}' \Psi(\mathbf{r}, \boldsymbol{\Omega}', E')
\end{aligned}
\tag{1.1}
$$

The underlying principle of Eq. 1.1 is to balance neutron losses and gains through the eigenvalue k_{eff}. A summary of the variables involved in the equation is given in Table 1.1.

Table 1.1: Variables in the Boltzmann neutron transport equation

Variable	Description
$\mathbf{r}$	Spatial position vector
$\boldsymbol{\Omega}$	Angular direction vector
E	Neutron energy
Ψ	Angular neutron flux
k_{eff}	Effective neutron multiplication factor
Σ^T	Neutron total cross-section
Σ^S	Neutron scattering cross-section
Σ^F	Neutron fission cross-section
χ	Energy spectrum for fission neutron emission
ν	Number of neutrons emitted per fission

This equation is given generally for continuous energy cross sections. However, in many methods such as MOC, it is necessary to use discrete multi-group cross sections. This is an approximation since cross sections do indeed depend continuously on energy. Continuous energy cross sections are collapsed to group cross sections by calculating the average cross section over the energy interval of interest weighted by the neutron scalar flux. The physical interpretation of weighting by the neutron flux is to preserve reaction rates within the phase space of interest.

Once group cross sections are formed, MOC can be used to solve the neutron transport problem. First, the polar and azimuthal angular flux components are discretized by forming neutron tracks. Many tracks are created to cover the geometry that is divided into source regions. In a given source region the neutron source is assumed to have a certain shape, such as flat or of higher order. Tracks contribute to the scalar flux of each source region they pass through. The bulk of the computational work occurs during transport sweeps in which angular fluxes along tracks are solved.

As long as there are sufficiently many tracks covering the geometry, a fine enough spatial refinement of the neutron source, and sufficiently broad angular distribution of tracks to cover the phase space, MOC will converge to the solution of the Boltzmann neutron transport equation for the selected set of discrete multi-group cross sections.

1.4 Description of Nodal Methods

Nodal diffusion methods represent a significant simplification from detailed transport solutions. In particular, the angular variable is completely integrated out by assuming that fluxes are at most linearly dependent on angle which leads to the neutron diffusion equation that has no angular dependence. In addition, the CASMO detailed spatial, angular, and energy distribution of fluxes is used to spatially homogenize and energy collapse cross sections to two energy groups. The homogenized diffusion equations with assembly or quarter-assembly nodalization are then solved with the heterogeneity effects of the lattice approximated using assembly discontinuity factors [15]. Detector fission rates and individual pin powers are approximated using traditional flux reconstruction techniques.

In the spatial domain, nodal methods utilize the transverse leakage approximation to reduce the full 3D diffusion equations to a set of three coupled 1D equations that can be solved very accurately [14]. In SIMULATE-3 the transverse leakage is represented by a quadratic polynomial and the flux shape for the 1-D flux solution is modeled with fourth-order polynomials. The intra-nodal spatial shapes of xenon, fuel temperature, and cross sections are approximated using quadratic shape functions within each radial node.

Fuel depletion effects in the SIMULATE-3 nodal model are treated using a macroscopic depletion model in which all cross sections are modeled principally as functions of burnup (GWd/T) with history-effects corrections for moderator temperature, fuel temperature, and boron. All two-group cross sections, discontinuity factors, fission rate form functions and pin power form functions are treated with this macroscopic depletion model, and all parameters are tabulated from CASMO-5 single-assembly depletion calculations.

Radial reflector data models for SIMULATE-3 are generated by performing CASMO-5 calculations with one fuel assembly, the baffle, and the barrel in a pseudo 1D model. Two-group cross sections and discontinuity factors are computed for the homogenized baffle/reflector nodes as a function of coolant density and boron concentrations. Similar calculations are performed for the upper and lower axial reflectors in which radial details are homogenized for the CASMO-5 computations.

Coolant temperature/density and fuel temperature are computed using one characteristic fuel pin/channel for each radial node of the core model with the same axial nodalization as the diffusion equation (usually 24-25 nodes).

1.5 Comparison of Transport and Nodal Methods

Two models are developed in this investigation to compare inferred reactivities. The first uses the standard modeling process with the SIMULATE-3 [6] nodal diffusion simulator intended for full-core simulation. In this standard modeling process, a transport solver is used to simulate each unique assembly with reflected boundary conditions under a variety of reactor conditions. In this study, we utilize CASMO-5 for this purpose which generates a case matrix of neutron cross sections, discontinuity factors, and pin powers as a function of fuel temperature, moderator temperature, and boron concentration. These assembly calculations form a cross-section library which SIMULATE-3 interpolates for desired reactor conditions to solve the full-core problem using 2-group nodal diffusion theory and one-channel-per-assembly thermal hydraulic models. The radial discretization that SIMULATE-3 uses is one node per quarter-assembly, as illustrated in Fig. 1-1.

Approximations inherent to nodal diffusion theory are present and we would seek

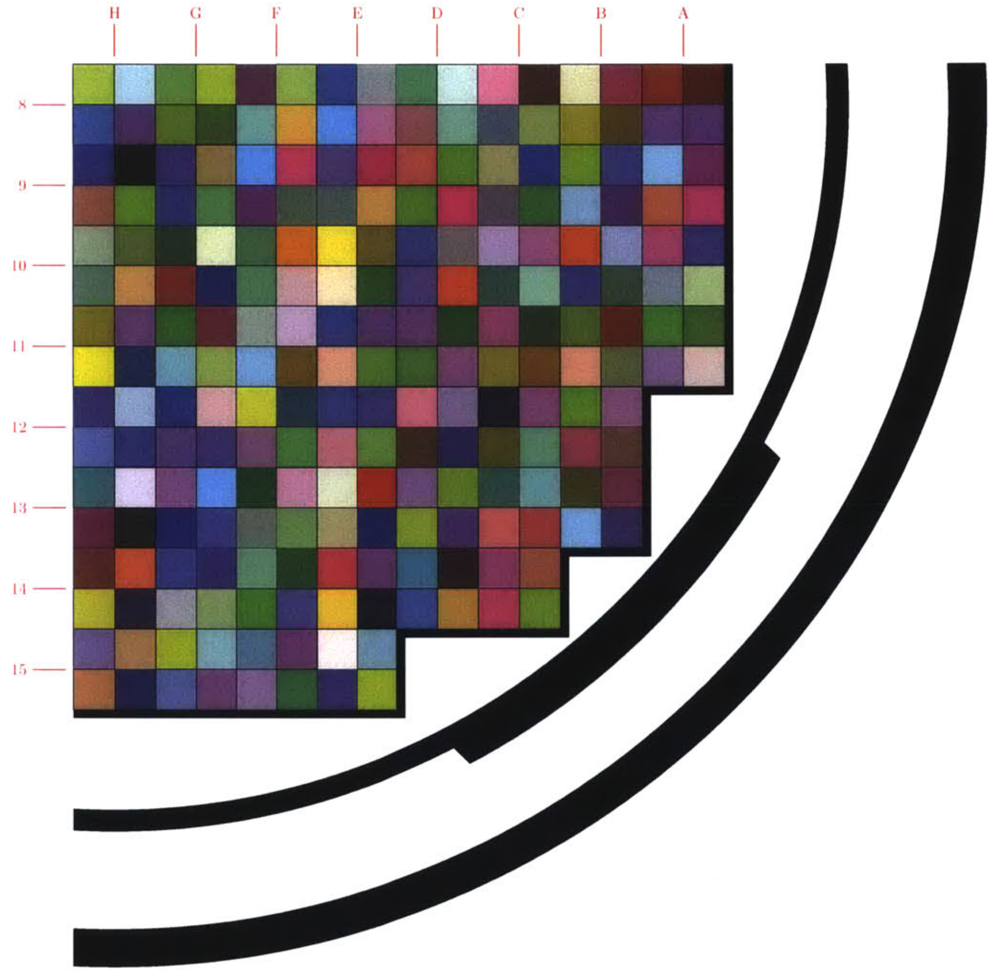

Figure 1-1: Quarter assembly SIMULATE-3 discretization for the quarter core model.

to compare with results computed using transport methods that do not incorporate such coarse discretization.

To accomplish this, the second model utilizes the MOC solver CASMO-5 M×N which is an extension of CASMO-5 for full-core simulation. The MOC solution is desirable for: 1) elimination of diffusion approximations, 2) increased spatial resolution, and 3) increased energy resolution. In the CASMO-5 M×N implementation, the core geometry is split into flat-source regions within which the neutron source from scattering and fission is assumed to be constant. The flat-source regions in the CASMO-5 M×N model are depicted in Fig. 1-2.

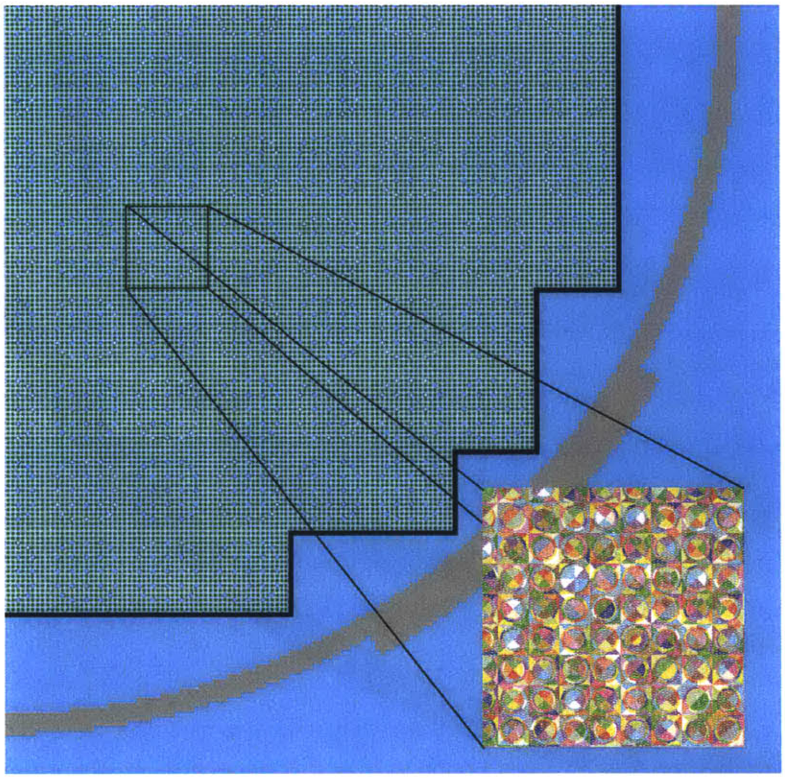

Figure 1-2: Spatial CASMO-5 M×N discretization given by the distribution of flat-source regions

As seen from the number of flat-source regions, the spatial resolution provided by MOC is much finer than that provided by nodal diffusion. These two models therefore involve fundamentally different assumptions and can provide a basis for examination of nodal approximations.

Chapter 2

BEAVRS Benchmark

The results of the various simulations using both MOC and nodal methods will be compared against the BEAVRS benchmark [7] to evaluate the errors introduced by nodal approximations. The BEAVRS benchmark contains information for the first two operating cycles of a PWR in the form of measured fission reaction rates for U-235 fission chamber measurements in the central instrument tube of each instrumented assembly. The axial distributions are integrated into 2D radial fission rate maps to form the basis of our comparison with measured data in this investigation.

2.1 Cycle 1

The first cycle of the BEAVRS benchmark introduces entirely fresh fuel. This allows high confidence in the initial isotopic distribution. The core loading is quarter-core rotationally symmetric with enrichments of 1.6%, 2.4%, and 3.1% enriched U-235 fuel. In addition to being quarter-core symmetric, the loading is also octant symmetric. This will become relevant later when developing the full-core model since only a quarter-core geometry needs to be solved with rotational *or* reflected boundary conditions.

In addition to a varied enrichment distribution, burnable poisons are placed throughout the core, once again with octant symmetry. The burnable poisons are borosilicate glass rods inserted in guide tube locations. Fig. 2-1 illustrates the enrichment distribution and burnable poison placement in cycle 1 and Fig. 2-2 shows a more detailed view of burnable poison placement. In this analysis we do not consider instrument tubes, which are not inserted symmetrically. This leads to a slight asymmetry that is not accounted for, but the effect is small.

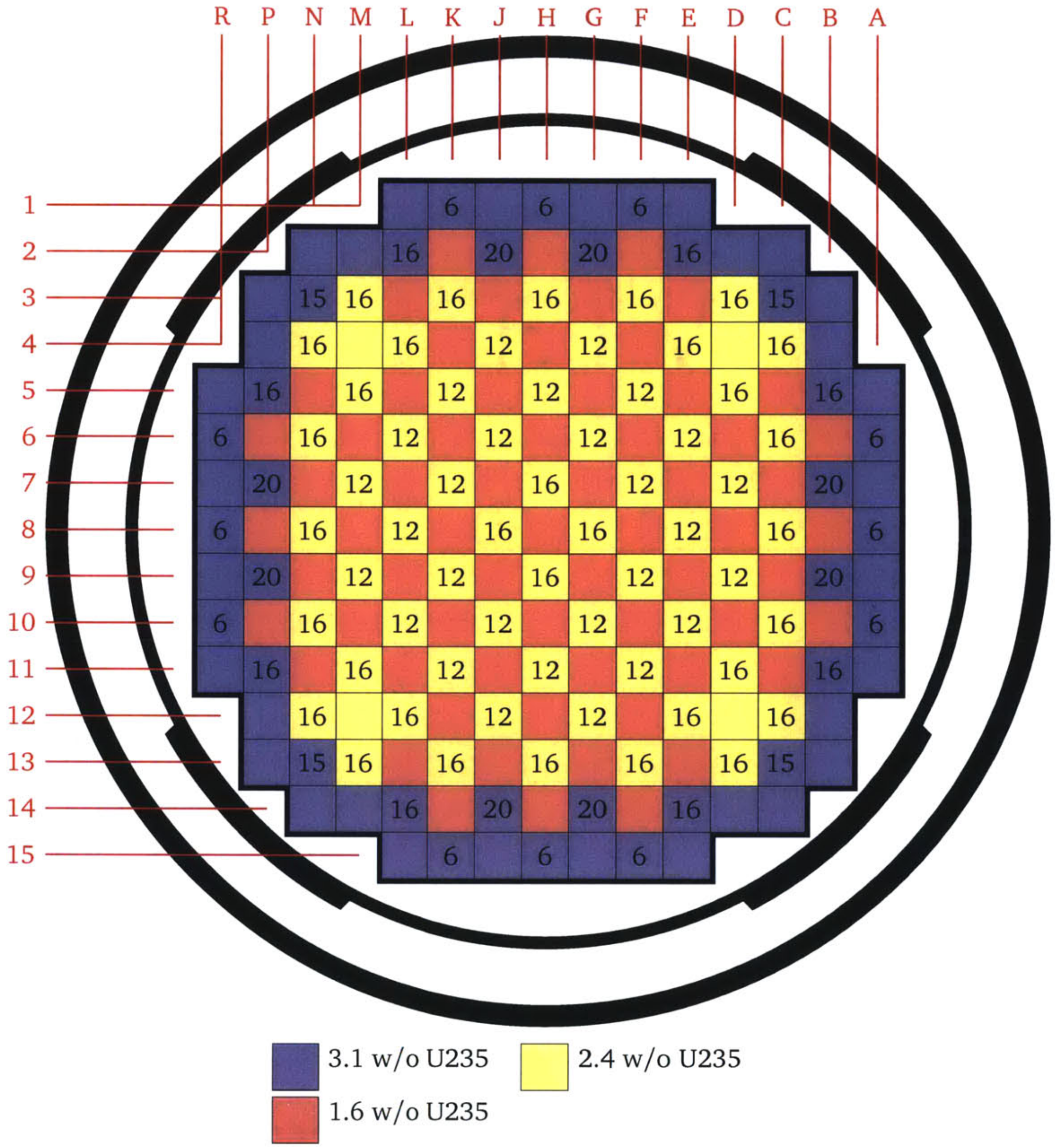

	R	P	N	M	L	K	J	H	G	F	E	D	C	B	A
1					🟦	🟦 6	🟦	🟦 6	🟦	🟦 6	🟦				
2			🟦	🟦	🟦 16	🟥	🟦 20	🟥	🟦 20	🟥	🟦 16	🟦	🟦		
3		🟦	🟦 15	🟨 16	🟥	🟨 16	🟥	🟨 16	🟥	🟨 16	🟥	🟨 16	🟦 15	🟦	
4		🟦	🟨 16	🟨	🟨 16	🟥	🟨 12	🟥	🟨 12	🟥	🟨 16	🟨	🟨 16	🟦	
5	🟦	🟦 16	🟥	🟨 16	🟥	🟨 12	🟥	🟨 12	🟥	🟨 12	🟥	🟨 16	🟥	🟦 16	🟦
6	🟦 6	🟥	🟨 16	🟥	🟨 12	🟥	🟨 12	🟥	🟨 12	🟥	🟨 12	🟥	🟨 16	🟥	🟦 6
7	🟦	🟦 20	🟥	🟨 12	🟥	🟨 12	🟥	🟨 16	🟥	🟨 12	🟥	🟨 12	🟥	🟦 20	🟦
8	🟦 6	🟥	🟨 16	🟥	🟨 12	🟥	🟨 16	🟥	🟨 16	🟥	🟨 12	🟥	🟨 16	🟥	🟦 6
9	🟦	🟦 20	🟥	🟨 12	🟥	🟨 12	🟥	🟨 16	🟥	🟨 12	🟥	🟨 12	🟥	🟦 20	🟦
10	🟦 6	🟥	🟨 16	🟥	🟨 12	🟥	🟨 12	🟥	🟨 12	🟥	🟨 12	🟥	🟨 16	🟥	🟦 6
11	🟦	🟦 16	🟥	🟨 16	🟥	🟨 12	🟥	🟨 12	🟥	🟨 12	🟥	🟨 16	🟥	🟦 16	🟦
12		🟦	🟨 16	🟨	🟨 16	🟥	🟨 12	🟥	🟨 12	🟥	🟨 16	🟨	🟨 16	🟦	
13		🟦	🟦 15	🟨 16	🟥	🟨 16	🟥	🟨 16	🟥	🟨 16	🟥	🟨 16	🟦 15	🟦	
14			🟦	🟦	🟦 16	🟥	🟦 20	🟥	🟦 20	🟥	🟦 16	🟦	🟦		
15					🟦	🟦 6	🟦	🟦 6	🟦	🟦 6	🟦				

Figure 2-1: BEAVRS cycle 1 enrichment and burnable poison distribution. The number of burnable poisons in each assembly is given by the number in the assembly whereas the color refers to enrichment.

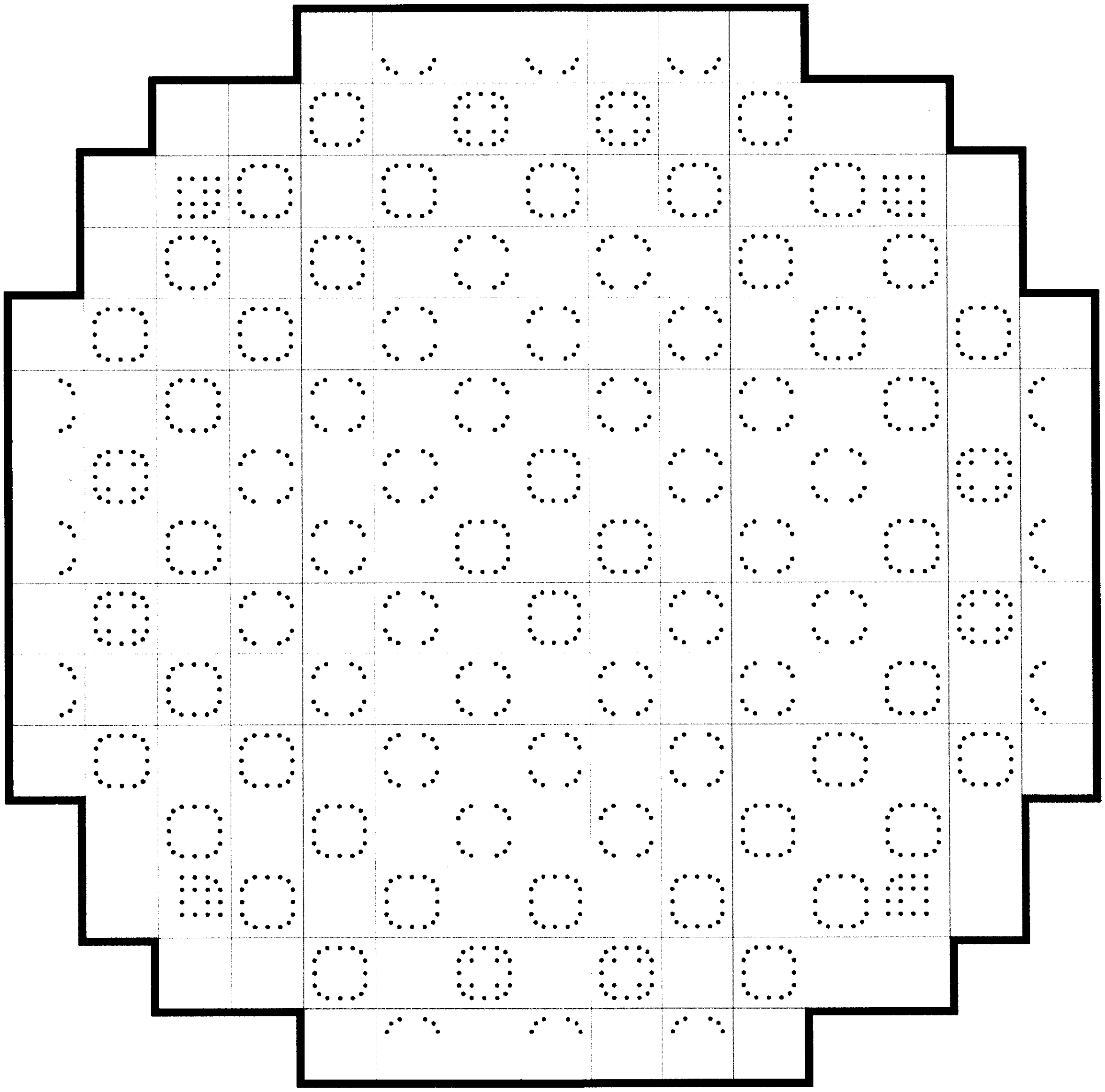

Figure 2-2: BEAVRS cycle 1 refined burnable poison distribution.

2.2 Cycle 2

In the second cycle, much of the once burned 2.4% enriched and 3.1% fuel is reloaded into the core. One 1.6% enriched bundle is placed at the center of the core. In addition, there is a split feed of 3.2% and 3.4% enriched fresh fuel. The core is designed to be quarter-core rotationally symmetric. However, it is *no longer* octant symmetric. Therefore *only* rotationally symmetric boundary conditions can be used when modeling the reactor core in quarter-core geometry. Additionally, the core loading is not strictly quarter-core symmetric since the central fuel bundle is shuffled from an outside location from cycle 1 and has a large burnup gradient. However, since the enrichment of the bundle is low, results show that the resulting computed power distributions are quarter-core symmetric to the precision provided by CASMO. The reloading pattern for cycle 2 is shown in Fig. 2-3. All burnable poisons are removed from the reloaded fuel.

It is often interesting to understand the initial burnup distribution which indicates the magnitude of fuel depletion that has occurred in each bundle in the first cycle and dictates the remaining reactivity of the fuel. The CASMO-5 M$\times$N simulated burnup distribution at the beginning of cycle 2 is illustrated in Fig. 2-4.

A summary of both cycles is given in Table 2.1.

Table 2.1: Reactor Cycle and Fuel Data

Unit	Cycle	Cycle Length (EFPD)	Enrichment Range (%)	HZP Boron (ppm)	Maximum Poison Pins per Assembly
BEAVRS	1	326	1.6 - 3.1	975	24
BEAVRS	2	285	3.2 - 3.4	1405	12

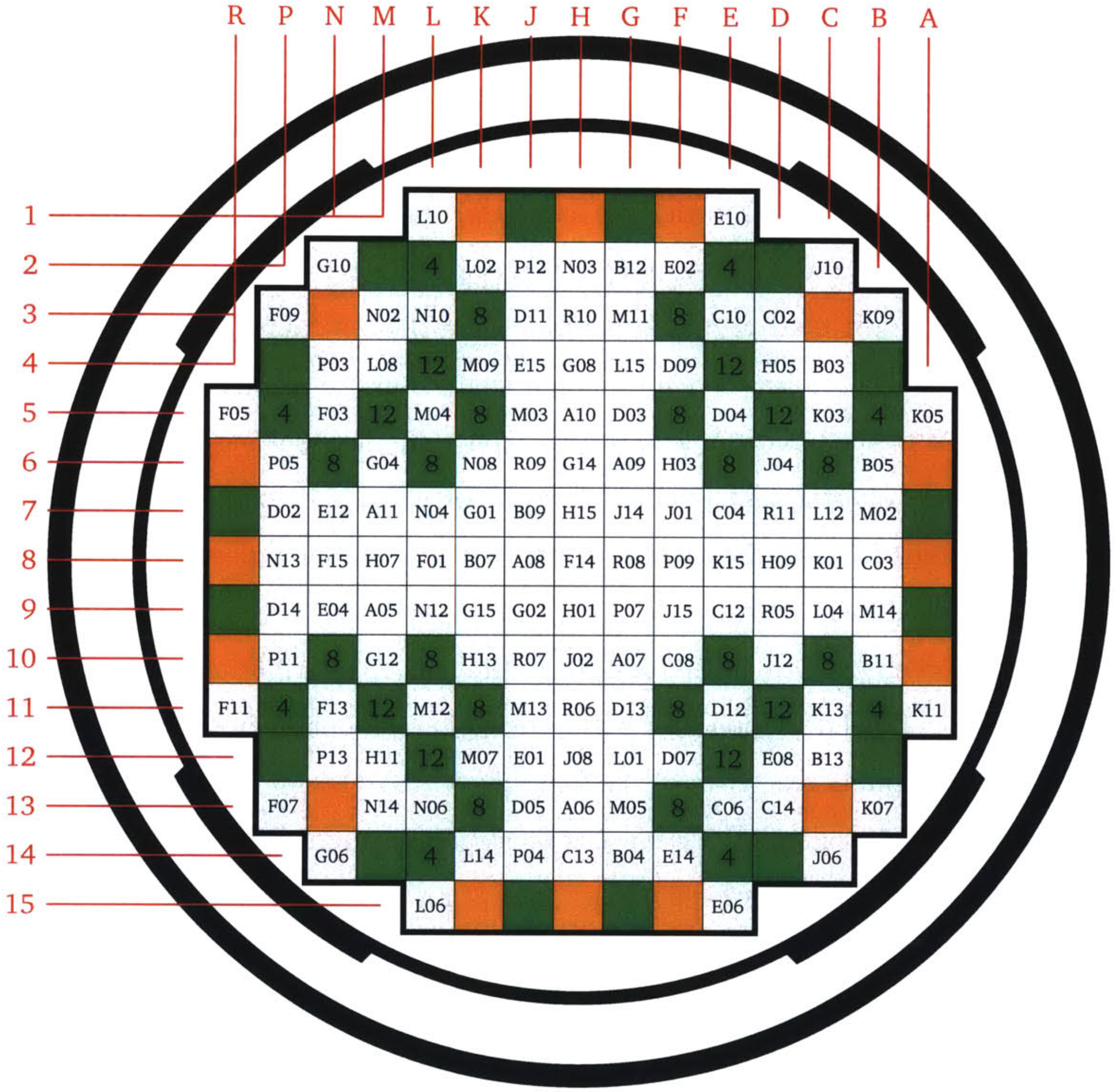

	R	P	N	M	L	K	J	H	G	F	E	D	C	B	A
1					L10	🟧	🟩	🟧	🟩	🟧	E10				
2			G10	🟩	🟩 4	L02	P12	N03	B12	E02	🟩 4	🟩	J10		
3		F09	🟧	N02	N10	🟩 8	D11	R10	M11	🟩 8	C10	C02	🟧	K09	
4		🟩	P03	L08	🟩 12	M09	E15	G08	L15	D09	🟩 12	H05	B03	🟩	
5	F05	🟩 4	F03	🟩 12	M04	🟩 8	M03	A10	D03	🟩 8	D04	🟩 12	K03	🟩 4	K05
6	🟧	P05	🟩 8	G04	🟩 8	N08	R09	G14	A09	H03	🟩 8	J04	🟩 8	B05	🟧
7	🟩	D02	E12	A11	N04	G01	B09	H15	J14	J01	C04	R11	L12	M02	🟩
8	🟧	N13	F15	H07	F01	B07	A08	F14	R08	P09	K15	H09	K01	C03	🟧
9	🟩	D14	E04	A05	N12	G15	G02	H01	P07	J15	C12	R05	L04	M14	🟩
10	🟧	P11	🟩 8	G12	🟩 8	H13	R07	J02	A07	C08	🟩 8	J12	🟩 8	B11	🟧
11	F11	🟩 4	F13	🟩 12	M12	🟩 8	M13	R06	D13	🟩 8	D12	🟩 12	K13	🟩 4	K11
12		🟩	P13	H11	🟩 12	M07	E01	J08	L01	D07	🟩 12	E08	B13	🟩	
13		F07	🟧	N14	N06	🟩 8	D05	A06	M05	🟩 8	C06	C14	🟧	K07	
14			G06	🟩	🟩 4	L14	P04	C13	B04	E14	🟩 4	🟩	J06		
15					L06	🟧	🟩	🟧	🟩	🟧	E06				

🟩 Fresh 3.2 w/o U235
🟧 Fresh 3.4 w/o U235
⬜ Shuffled Assembly

Figure 2-3: BEAVRS cycle 2 enrichment and burnable poison distribution. The number of burnable poisons in each assembly is given by the number in the assembly for fresh fuel. For shuffled shuffled assemblies, the position of the assembly in the cycle 1 configuration is presented. The color refers to enrichment for fresh fuel.

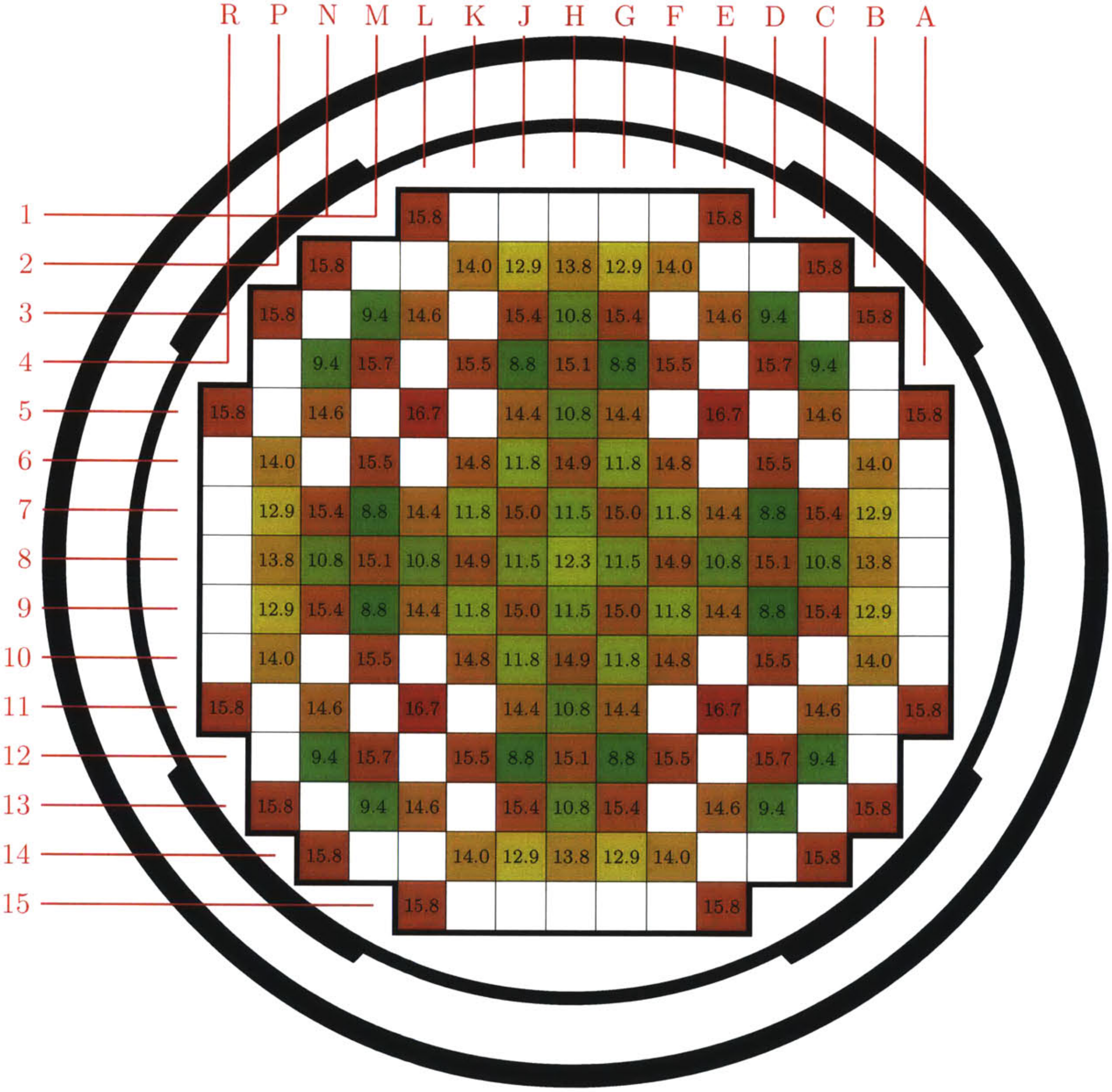

	R	P	N	M	L	K	J	H	G	F	E	D	C	B	A
1					15.8						15.8				
2			15.8			14.0	12.9	13.8	12.9	14.0			15.8		
3		15.8		9.4	14.6		15.4	10.8	15.4		14.6	9.4		15.8	
4			9.4	15.7		15.5	8.8	15.1	8.8	15.5		15.7	9.4		
5	15.8		14.6		16.7		14.4	10.8	14.4		16.7		14.6		15.8
6		14.0		15.5		14.8	11.8	14.9	11.8	14.8		15.5		14.0	
7		12.9	15.4	8.8	14.4	11.8	15.0	11.5	15.0	11.8	14.4	8.8	15.4	12.9	
8		13.8	10.8	15.1	10.8	14.9	11.5	12.3	11.5	14.9	10.8	15.1	10.8	13.8	
9		12.9	15.4	8.8	14.4	11.8	15.0	11.5	15.0	11.8	14.4	8.8	15.4	12.9	
10		14.0		15.5		14.8	11.8	14.9	11.8	14.8		15.5		14.0	
11	15.8		14.6		16.7		14.4	10.8	14.4		16.7		14.6		15.8
12			9.4	15.7		15.5	8.8	15.1	8.8	15.5		15.7	9.4		
13		15.8		9.4	14.6		15.4	10.8	15.4		14.6	9.4		15.8	
14			15.8			14.0	12.9	13.8	12.9	14.0			15.8		
15					15.8						15.8				

Figure 2-4: Axially averaged burnup distribution at the beginning of cycle 2 in GWd/T. Blank squares indicate fresh fuel.

Chapter 3

Overview of Core Models

In the introduction, we examined approximations involved in the SIMULATE-3 nodal code that are not present in CASMO-5. Therefore results obtained by full-core CASMO-5 M×N simulations allow for examination of errors introduced by nodal approximations. However, since CASMO-5 is generally used for lattice calculations instead of full-core modeling, some complications arise.

3.1 Modeling Approximations

3.1.1 Thermal Hydraulic Feedback

The first complication is the absence of a thermal hydraulic feedback model in CASMO-5. Whereas SIMULATE-3 utilizes a simple thermal feedback model to determine appropriate temperatures and cross sections, CASMO-5 is designed for lattice calculations which rely on temperature as input. To test how much effect thermal feedback has on core power distributions, the SIMULATE-3 3D model using thermal hydraulic feedback is compared to a model with thermal feedback disabled. A comparison of axially-integrated fission rate distributions from these two models is shown in Fig. 3-1.

Results show it is indeed important to include thermal feedback information. Therefore to include thermal information for correct cross section calculation, the resulting fuel and moderator temperatures from SIMULATE-3 simulations are used

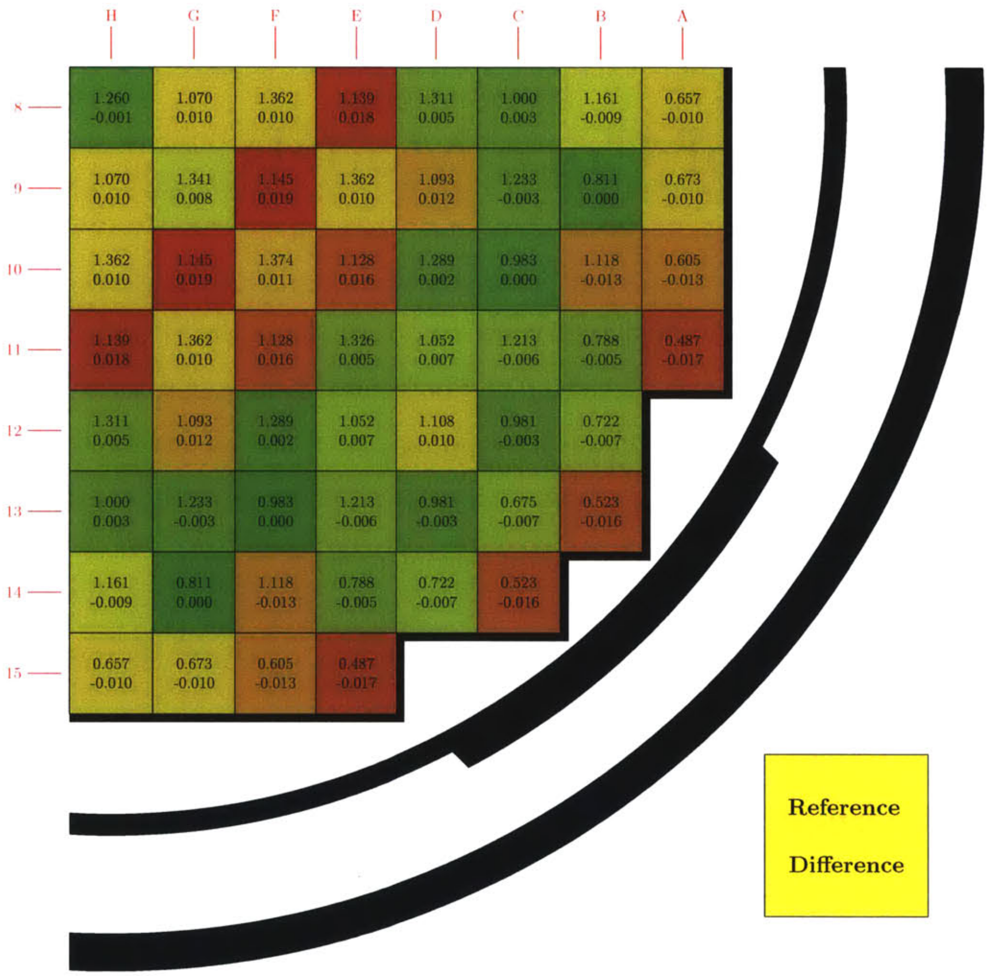

	H	G	F	E	D	C	B	A
8	1.260 -0.001	1.070 0.010	1.362 0.010	1.139 0.018	1.311 0.005	1.000 0.003	1.161 -0.009	0.657 -0.010
9	1.070 0.010	1.341 0.008	1.145 0.019	1.362 0.010	1.093 0.012	1.233 -0.003	0.811 0.000	0.673 -0.010
10	1.362 0.010	1.145 0.019	1.374 0.011	1.128 0.016	1.289 0.002	0.983 0.000	1.118 -0.013	0.605 -0.013
11	1.139 0.018	1.362 0.010	1.128 0.016	1.326 0.005	1.052 0.007	1.213 -0.006	0.788 -0.005	0.487 -0.017
12	1.311 0.005	1.093 0.012	1.289 0.002	1.052 0.007	1.108 0.010	0.981 -0.003	0.722 -0.007	
13	1.000 0.003	1.233 -0.003	0.983 0.000	1.213 -0.006	0.981 -0.003	0.675 -0.007	0.523 -0.016	
14	1.161 -0.009	0.811 0.000	1.118 -0.013	0.788 -0.005	0.722 -0.007	0.523 -0.016		
15	0.657 -0.010	0.673 -0.010	0.605 -0.013	0.487 -0.017				

Figure 3-1: Difference in reaction rates of the SIMULATE-3 3D model without thermal hydraulic feedback relative to the model with thrmal hydraulic feedback at 2.16 GWd/T exposure in cycle 1. The RMS difference is 0.0103.

as input into CASMO-5 M×N. This is accomplished by first conducting depletion calculations in SIMULATE-3 from beginning of cycle to end of cycle in steps of 0.1 GWd/T which is generally considered to be a fine discretization for depletion calculations. Next, 50 statepoints are selected from the depletion cases. For each statepoint selected, temperature maps which include average fuel and moderator temperatures for each assembly are edited from SIMULATE-3 and copied into the CASMO-5 M×N input. The data is used to determine the correct temperature at each depletion statepoint assuming that over small depletion steps temperatures are constant. The temperatures are always edited from the final SIMULATE-3 model with which CASMO-5 results are compared so that hydraulic parameters are consistent between the models.

The CASMO-5 calculation also includes the fine discretization of 0.1 GWd/T during its depletion calculations so some statepoint temperatures do vary slightly from those used in SIMULATE-3 since CASMO-5 assumes constant temperatures between input statepoint temperatures.

The temperatures that are used as input for CASMO-5 will be from the final SIMULATE-3 comparison model, which is two-dimensional. The reason for using temperatures from the two-dimensional model is to directly test the impact of the differences in the neutron physics models. As much as possible, we would like to remove other variables from impacting the results, such as differences in temperature distributions.

3.1.2 Thermal Expansion

The next complication is the necessity of no thermal expansion in CASMO-5 M×N. Whereas CASMO-5 used for lattice physics calculations includes thermal expansion to hot operating dimensions to form cross sections and model single assemblies, CASMO-5 M×N does not have this ability due to interference between assemblies. Therefore, it is important to determine the effect of thermal expansion on fission rate distributions. To do this SIMULATE-3 results using the default cross-section library from CASMO-5 with thermal expansion included are compared to SIMULATE-3 results using a library produced with thermal expansion disabled. The results given in Fig. 3-2 show the effect of thermal expansion is much less than that from thermal feedback. Since there is no simple way to incorporate the effect of thermal expansion without rewriting the underlying code, the CASMO-5 M×N model will deal only with cold dimensions.

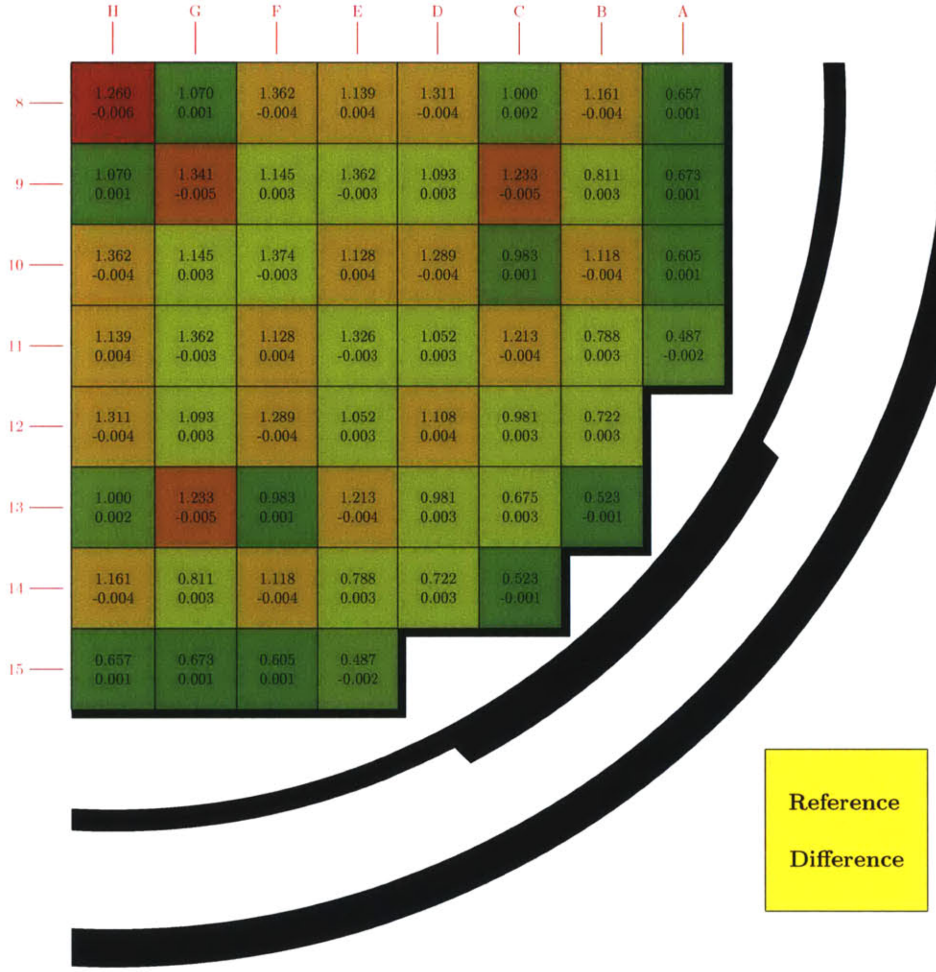

	H	G	F	E	D	C	B	A
8	1.260 -0.006	1.070 0.001	1.362 -0.004	1.139 0.004	1.311 -0.004	1.000 0.002	1.161 -0.004	0.657 0.001
9	1.070 0.001	1.341 -0.005	1.145 0.003	1.362 -0.003	1.093 0.003	1.233 -0.005	0.811 0.003	0.673 0.001
10	1.362 -0.004	1.145 0.003	1.374 -0.003	1.128 0.004	1.289 -0.004	0.983 0.001	1.118 -0.004	0.605 0.001
11	1.139 0.004	1.362 -0.003	1.128 0.004	1.326 -0.003	1.052 0.003	1.213 -0.004	0.788 0.003	0.487 -0.002
12	1.311 -0.004	1.093 0.003	1.289 -0.004	1.052 0.003	1.108 0.004	0.981 0.003	0.722 0.003	
13	1.000 0.002	1.233 -0.005	0.983 0.001	1.213 -0.004	0.981 0.003	0.675 0.003	0.523 -0.001	
14	1.161 -0.004	0.811 0.003	1.118 -0.004	0.788 0.003	0.722 0.003	0.523 -0.001		
15	0.657 0.001	0.673 0.001	0.605 0.001	0.487 -0.002				

Figure 3-2: Difference in reaction rates of the SIMULATE-3 3D model without thermal expansion relative to the model with thrmal expansion at 2.16 GWd/T exposure in cycle 1. The RMS difference is 0.0032.

3.1.3 Effect of 2D Modeling

CASMO-5 is a two-dimensional code whereas SIMULATE-3 is usually designed for three-dimensional modeling with a user-specified number of axial nodes. Since the purpose is to compare two similar models, the number of axial nodes in SIMULATE-3 is set to one to create a two-dimensional model. In doing so, all axial information is lost. This includes axial rod positions. To further complicate the issue, CASMO-5 M×N cannot easily change power density as a function of burnup as is possible with SIMULATE-3. Therefore, the behavior is approximated by depleting at full power and only comparing at depletion steps where true operating power is near full power. At these near full power statepoints, rods are almost completely withdrawn. However, the D bank is slightly inserted (step 213 of 225). To understand how great the effect of neglecting rod insertions and power history at near full power stateponits, the 3D SIMULATE-3 model which depicts the exact power history and rod movements is compared with a SIMULATE-3 model that runs at full power with no rod insertions at a near full power statepoint. We call this model with no rod insertions and full power operation the 3D ARO (all rods out) model with results shown in Fig. 3-3.

The differences are nearly unnoticeable except for a couple of locations. These two locations correspond to D-bank locations. This is the effect of the slight D-bank insertion. It is noticeable at the insertion locations but outside these locations there is very little effect on fission rate distributions. Since partial rod insertions cannot be accurately modeled in two dimensions, we are forced to neglect rod insertions. Next we move to truly 2D modeling which is compared with the 3D ARO model in Fig. 3-4.

There is noticeable disagreement between the models near the center and edge of the reactor, particularly near the reactor barrel. One source of error is the lack of axial leakage information. To counteract this, axial buckling is extracted from the 3D ARO model and input into the two-dimensional model as a function of burnup. Comparison of the new 2D model including axial buckling factors with the 3D ARO model is given in Fig. 3-5.

The new 2D model with axial buckling is in much closer agreement with the 3D ARO model as the RMS difference of normalized fission rates has declined from 0.0042 to 0.0019. This 2D model with axial buckling as a function of burnup will form the basis of the SIMULATE-3 modeling and comparison with CASMO-5 M×N.

In CASMO-5 M×N there is also an option to insert axial buckling but it cannot be burnup-dependent. Therefore an average representative buckling factor is selected for all burnup steps. The effect of this axial buckling factor relative to the CASMO-5

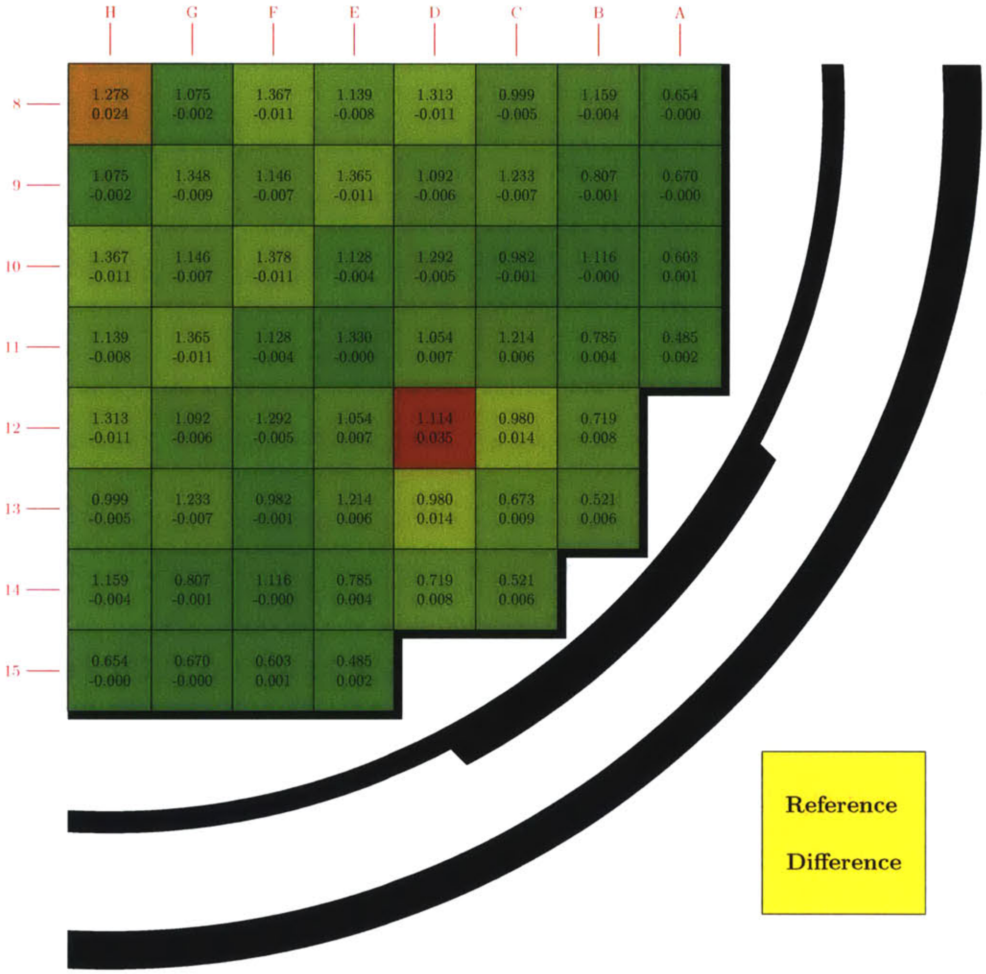

	H	G	F	E	D	C	B	A
8	1.278 0.024	1.075 -0.002	1.367 -0.011	1.139 -0.008	1.313 -0.011	0.999 -0.005	1.159 -0.004	0.654 -0.000
9	1.075 -0.002	1.348 -0.009	1.146 -0.007	1.365 -0.011	1.092 -0.006	1.233 -0.007	0.807 -0.001	0.670 -0.000
10	1.367 -0.011	1.146 -0.007	1.378 -0.011	1.128 -0.004	1.292 -0.005	0.982 -0.001	1.116 -0.000	0.603 0.001
11	1.139 -0.008	1.365 -0.011	1.128 -0.004	1.330 -0.000	1.054 0.007	1.214 0.006	0.785 0.004	0.485 0.002
12	1.313 -0.011	1.092 -0.006	1.292 -0.005	1.054 0.007	1.114 0.035	0.980 0.014	0.719 0.008	
13	0.999 -0.005	1.233 -0.007	0.982 -0.001	1.214 0.006	0.980 0.014	0.673 0.009	0.521 0.006	
14	1.159 -0.004	0.807 -0.001	1.116 -0.000	0.785 0.004	0.719 0.008	0.521 0.006		
15	0.654 -0.000	0.670 -0.000	0.603 0.001	0.485 0.002				

Figure 3-3: Difference in reaction rates of the SIMULATE-3 3D ARO model relative to the 3D with partially rods inserted at 2.16 GWd/T exposure in cycle 1. The RMS difference is 0.0086.

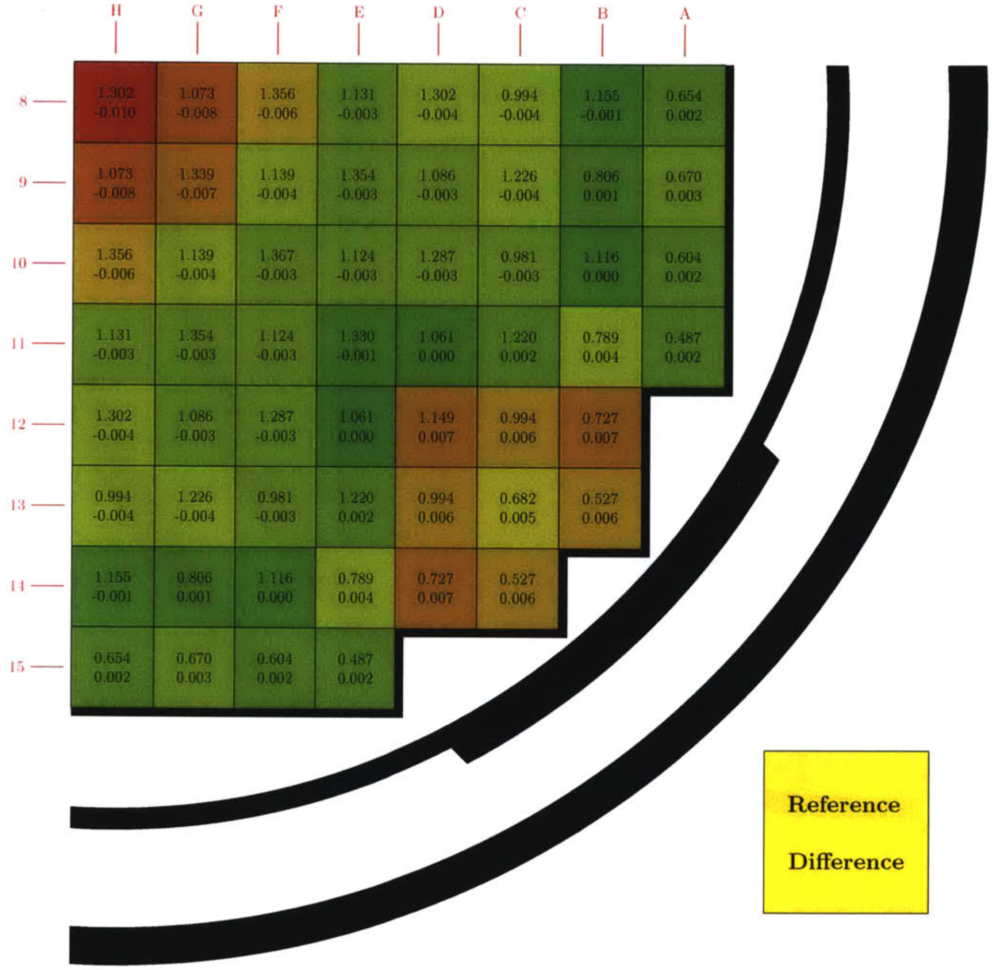

	H	G	F	E	D	C	B	A
8	1.302 -0.010	1.073 -0.008	1.356 -0.006	1.131 -0.003	1.302 -0.004	0.994 -0.004	1.155 -0.001	0.654 0.002
9	1.073 -0.008	1.339 -0.007	1.139 -0.004	1.354 -0.003	1.086 -0.003	1.226 -0.004	0.806 0.001	0.670 0.003
10	1.356 -0.006	1.139 -0.004	1.367 -0.003	1.124 -0.003	1.287 -0.003	0.981 -0.003	1.116 0.000	0.604 0.002
11	1.131 -0.003	1.354 -0.003	1.124 -0.003	1.330 -0.001	1.061 0.000	1.220 0.002	0.789 0.004	0.487 0.002
12	1.302 -0.004	1.086 -0.003	1.287 -0.003	1.061 0.000	1.149 0.007	0.994 0.006	0.727 0.007	
13	0.994 -0.004	1.226 -0.004	0.981 -0.003	1.220 0.002	0.994 0.006	0.682 0.005	0.527 0.006	
14	1.155 -0.001	0.806 0.001	1.116 0.000	0.789 0.004	0.727 0.007	0.527 0.006		
15	0.654 0.002	0.670 0.003	0.604 0.002	0.487 0.002				

Figure 3-4: Difference in reaction rates of the SIMULATE-3 2D model without axial buckling relative to the 3D ARO model at 2.16 GWd/T exposure in cycle 1. The RMS difference is 0.0042.

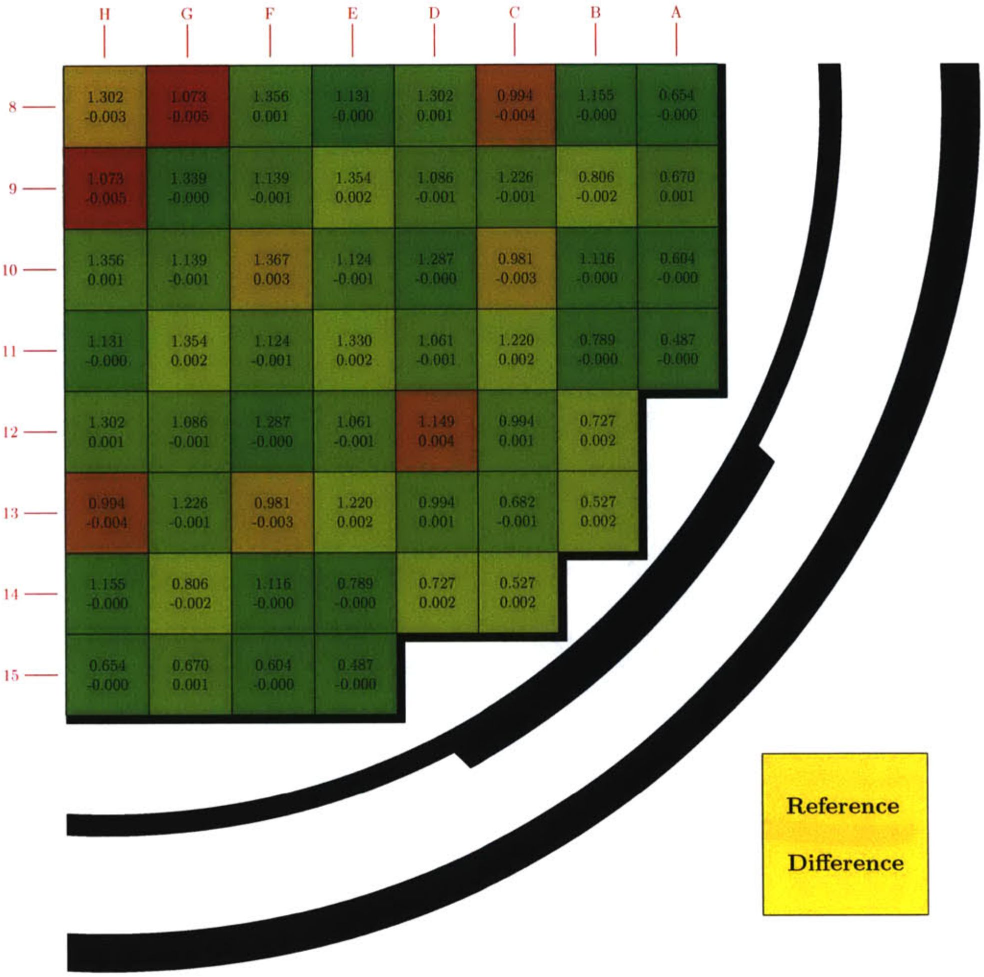

	H	G	F	E	D	C	B	A
8	1.302 -0.003	1.073 -0.005	1.356 0.001	1.131 -0.000	1.302 0.001	0.994 -0.004	1.155 -0.000	0.654 -0.000
9	1.073 -0.005	1.339 -0.000	1.139 -0.001	1.354 0.002	1.086 -0.001	1.226 -0.001	0.806 -0.002	0.670 0.001
10	1.356 0.001	1.139 -0.001	1.367 0.003	1.124 -0.001	1.287 -0.000	0.981 -0.003	1.116 -0.000	0.604 -0.000
11	1.131 -0.000	1.354 0.002	1.124 -0.001	1.330 0.002	1.061 -0.001	1.220 0.002	0.789 -0.000	0.487 -0.000
12	1.302 0.001	1.086 -0.001	1.287 -0.000	1.061 -0.001	1.149 0.004	0.994 0.001	0.727 0.002	
13	0.994 -0.004	1.226 -0.001	0.981 -0.003	1.220 0.002	0.994 0.001	0.682 -0.001	0.527 0.002	
14	1.155 -0.000	0.806 -0.002	1.116 -0.000	0.789 -0.000	0.727 0.002	0.527 0.002		
15	0.654 -0.000	0.670 0.001	0.604 -0.000	0.487 -0.000				

Reference

Difference

Figure 3-5: Difference in reaction rates of the SIMULATE-3 2D model with axial buckling relative to the 3D ARO model at 2.16 GWd/T exposure in cycle 1. The RMS difference is 0.0019.

M×N model without the axial buckling factor is given in Fig. 3-6.

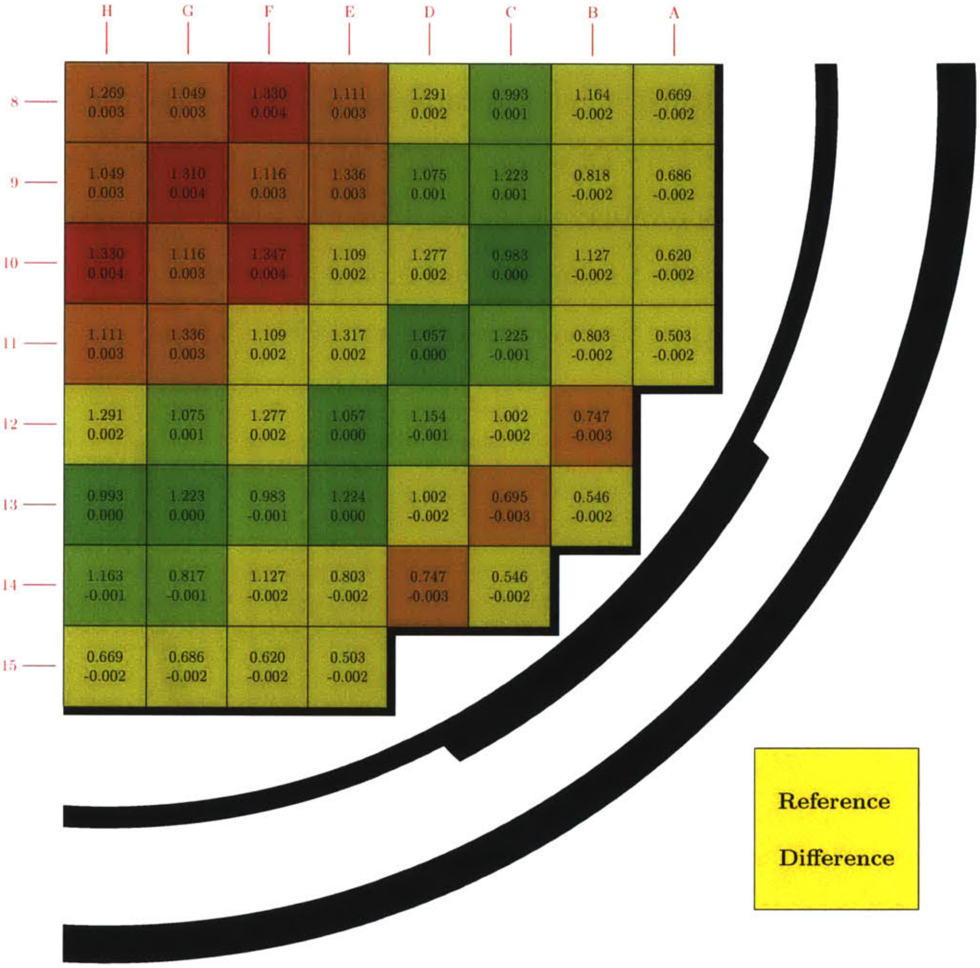

	H	G	F	E	D	C	B	A
8	1.269 0.003	1.049 0.003	1.330 0.004	1.111 0.003	1.291 0.002	0.993 0.001	1.164 -0.002	0.669 -0.002
9	1.049 0.003	1.310 0.004	1.116 0.003	1.336 0.003	1.075 0.001	1.223 0.001	0.818 -0.002	0.686 -0.002
10	1.330 0.004	1.116 0.003	1.347 0.004	1.109 0.002	1.277 0.002	0.983 0.000	1.127 -0.002	0.620 -0.002
11	1.111 0.003	1.336 0.003	1.109 0.002	1.317 0.002	1.057 0.000	1.225 -0.001	0.803 -0.002	0.503 -0.002
12	1.291 0.002	1.075 0.001	1.277 0.002	1.057 0.000	1.154 -0.001	1.002 -0.002	0.747 -0.003	
13	0.993 0.000	1.223 0.000	0.983 -0.001	1.224 0.000	1.002 -0.002	0.695 -0.003	0.546 -0.002	
14	1.163 -0.001	0.817 -0.001	1.127 -0.002	0.803 -0.002	0.747 -0.003	0.546 -0.002		
15	0.669 -0.002	0.686 -0.002	0.620 -0.002	0.503 -0.002				

Figure 3-6: Difference in reaction rates of the CASMO-5 M×N model without axial buckling relative to the same model with axial buckling at 2.16 GWd/T exposure in cycle 1. The RMS difference is 0.0022.

From Fig. 3-6 notice that the effect of the axial buckling factor is an in-out tilt that decreases fission rates near the center of the reactor core. This is consistent with the difference observed in SIMULATE-3. Therefore, we can be comfortable using a 2D model to produce results that are relatively comparable with 3D models.

3.1.4 Baffle Thickness

One last issue that is encountered when using CASMO-5 M×N is baffle thickness. In BEAVRS, the baffle is given as being 2.22 cm and this can be directly input into the

SIMULATE-3 model with no issue. However, in CASMO-5 M×N the baffle thickness needs to be input as an integer number of pin pitches. Since the pin pitch is 1.26, the correct number of pin pitches should be 1.76. To account for the fact that this is not an integer, density of baffle material is corrected to preserve the product of baffle thickness and material density. Of course, this is an approximation since neutrons can traverse the baffle from a variety of angles. To model a baffle that is closest to the true baffle dimensions, a baffle thickness of one or two pin pitches should be selected. The comparison between their fission rates is shown in Fig. 3-7.

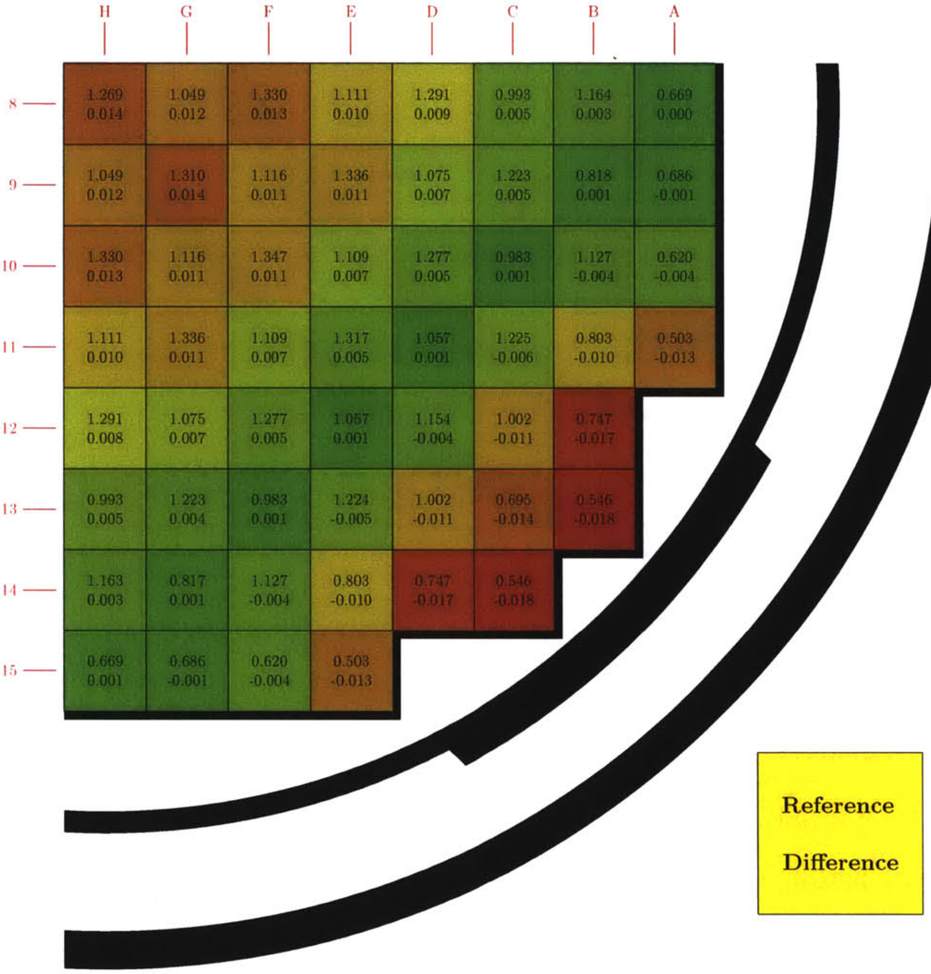

	H	G	F	E	D	C	B	A
8	1.269 0.014	1.049 0.012	1.330 0.013	1.111 0.010	1.291 0.009	0.993 0.005	1.164 0.003	0.669 0.000
9	1.049 0.012	1.310 0.014	1.116 0.011	1.336 0.011	1.075 0.007	1.223 0.005	0.818 0.001	0.686 -0.001
10	1.330 0.013	1.116 0.011	1.347 0.011	1.109 0.007	1.277 0.005	0.983 0.001	1.127 -0.004	0.620 -0.004
11	1.111 0.010	1.336 0.011	1.109 0.007	1.317 0.005	1.057 0.001	1.225 -0.006	0.803 -0.010	0.503 -0.013
12	1.291 0.008	1.075 0.007	1.277 0.005	1.057 0.001	1.154 -0.004	1.002 -0.011	0.747 -0.017	
13	0.993 0.005	1.223 0.004	0.983 0.001	1.224 -0.005	1.002 -0.011	0.695 -0.014	0.546 -0.018	
14	1.163 0.003	0.817 0.001	1.127 -0.004	0.803 -0.010	0.747 -0.017	0.546 -0.018		
15	0.669 0.001	0.686 -0.001	0.620 -0.004	0.503 -0.013				

Figure 3-7: Difference in reaction rates of the CASMO-5 M×N model with a one pincell thick baffle relative to the same model with a two pincell thick baffle at 2.16 GWd/T exposure in cycle 1. The RMS difference is 0.0092.

A noticeable difference is observed between the models. Since 1.76 is numerically closer to 2, we choose a baffle thickness to two pin pitches for the final CASMO-5

M×N model with appropriate density correction.

3.2 Influence of Approximations on Results

Now the models using the approximations previously mentioned are compared with measured data to determine their merits. To begin, the 3D SIMULATE-3 model that includes rod positions and power history is compared with measured data. The resulting error distribution at the hot full power (HFP) point (2.16 GWd/T) is shown in Fig. 3-8.

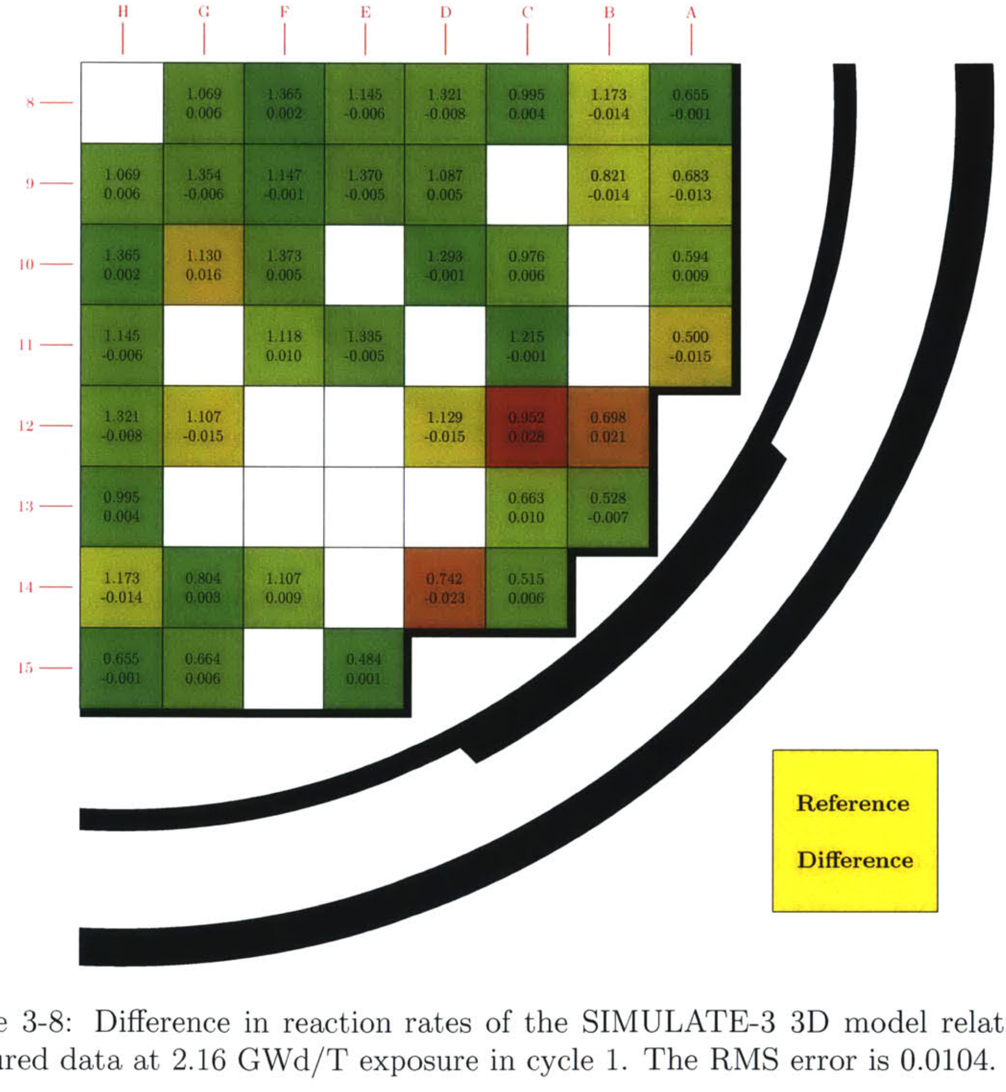

	H	G	F	E	D	C	B	A
8		1.069 0.006	1.365 0.002	1.145 -0.006	1.321 -0.008	0.995 0.004	1.173 -0.014	0.655 -0.001
9	1.069 0.006	1.354 -0.006	1.147 -0.001	1.370 -0.005	1.087 0.005		0.821 -0.014	0.683 -0.013
10	1.365 0.002	1.130 0.016	1.373 0.005		1.293 -0.001	0.976 0.006		0.594 0.009
11	1.145 -0.006		1.118 0.010	1.335 -0.005		1.215 -0.001		0.500 -0.015
12	1.321 -0.008	1.107 -0.015			1.129 -0.015	0.952 0.028	0.698 0.021	
13	0.995 0.004					0.663 0.010	0.528 -0.007	
14	1.173 -0.014	0.804 0.003	1.107 0.009		0.742 -0.023	0.515 0.006		
15	0.655 -0.001	0.664 0.006		0.484 0.001				

Figure 3-8: Difference in reaction rates of the SIMULATE-3 3D model relative to measured data at 2.16 GWd/T exposure in cycle 1. The RMS error is 0.0104.

Next, the 3D ARO model is compared with measured data and the error distribution is given in Fig. 3-9. The RMS error is comparable with that of the detailed 3D model but with slightly higher error, as expected.

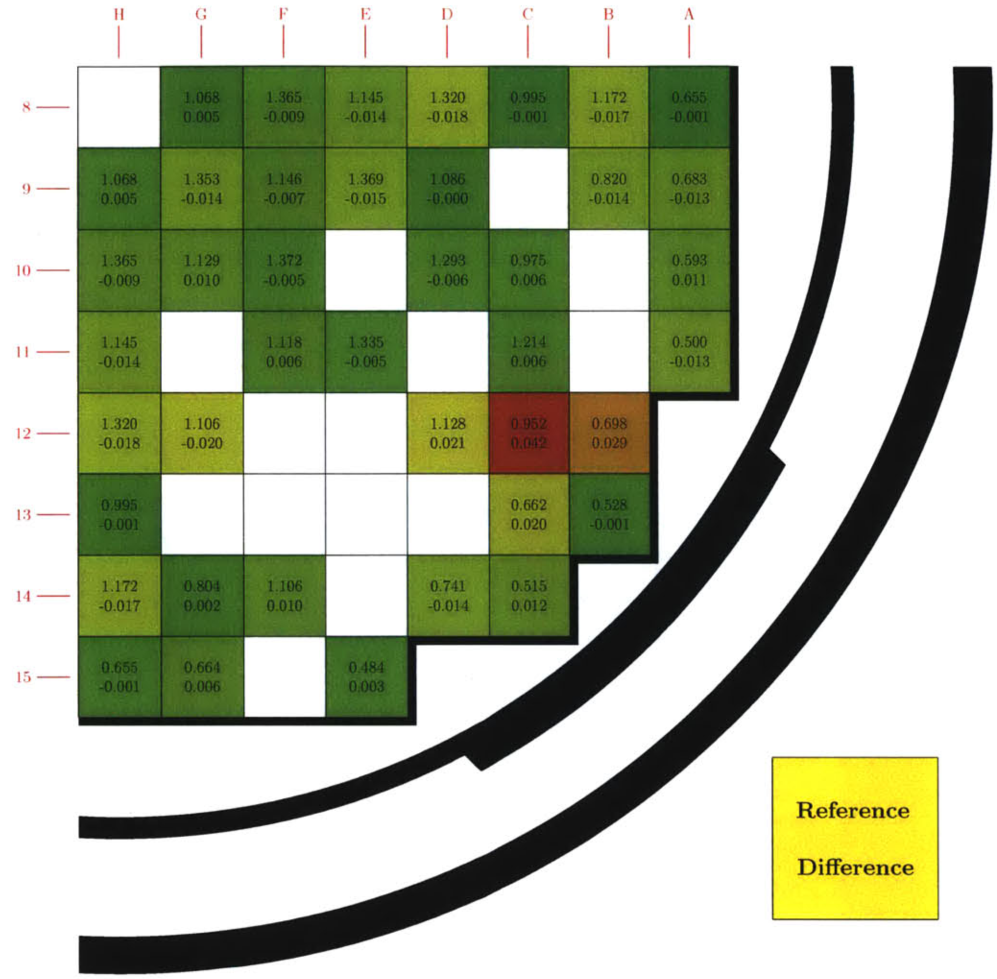

	H	G	F	E	D	C	B	A
8		1.068 0.005	1.365 -0.009	1.145 -0.014	1.320 -0.018	0.995 -0.001	1.172 -0.017	0.655 -0.001
9	1.068 0.005	1.353 -0.014	1.146 -0.007	1.369 -0.015	1.086 -0.000		0.820 -0.014	0.683 -0.013
10	1.365 -0.009	1.129 0.010	1.372 -0.005		1.293 -0.006	0.975 0.006		0.593 0.011
11	1.145 -0.014		1.118 0.006	1.335 -0.005		1.214 0.006		0.500 -0.013
12	1.320 -0.018	1.106 -0.020			1.128 0.021	0.952 0.042	0.698 0.029	
13	0.995 -0.001					0.662 0.020	0.528 -0.001	
14	1.172 -0.017	0.804 0.002	1.106 0.010		0.741 -0.014	0.515 0.012		
15	0.655 -0.001	0.664 0.006		0.484 0.003				

Figure 3-9: Difference in reaction rates of the SIMULATE-3 3D ARO model relative to measured data at 2.16 GWd/T exposure in cycle 1. The RMS error is 0.0137.

The final SIMULATE-3 model which we use to compare with CASMO-5 M×N is the 2D model with axial buckling as a function of burnup. The comparison with measured data at the HFP point is shown in Fig. 3-10. All temperature data used in the CASMO-5 models is edited from this model.

Now the CASMO-5 M×N models are analyzed and results using the model without axial buckling are given in Fig. 3-11. There is a significantly higher RMS error than the 2D SIMULATE-3 model.

With the addition of axial buckling we anticipate the RMS errors will significantly

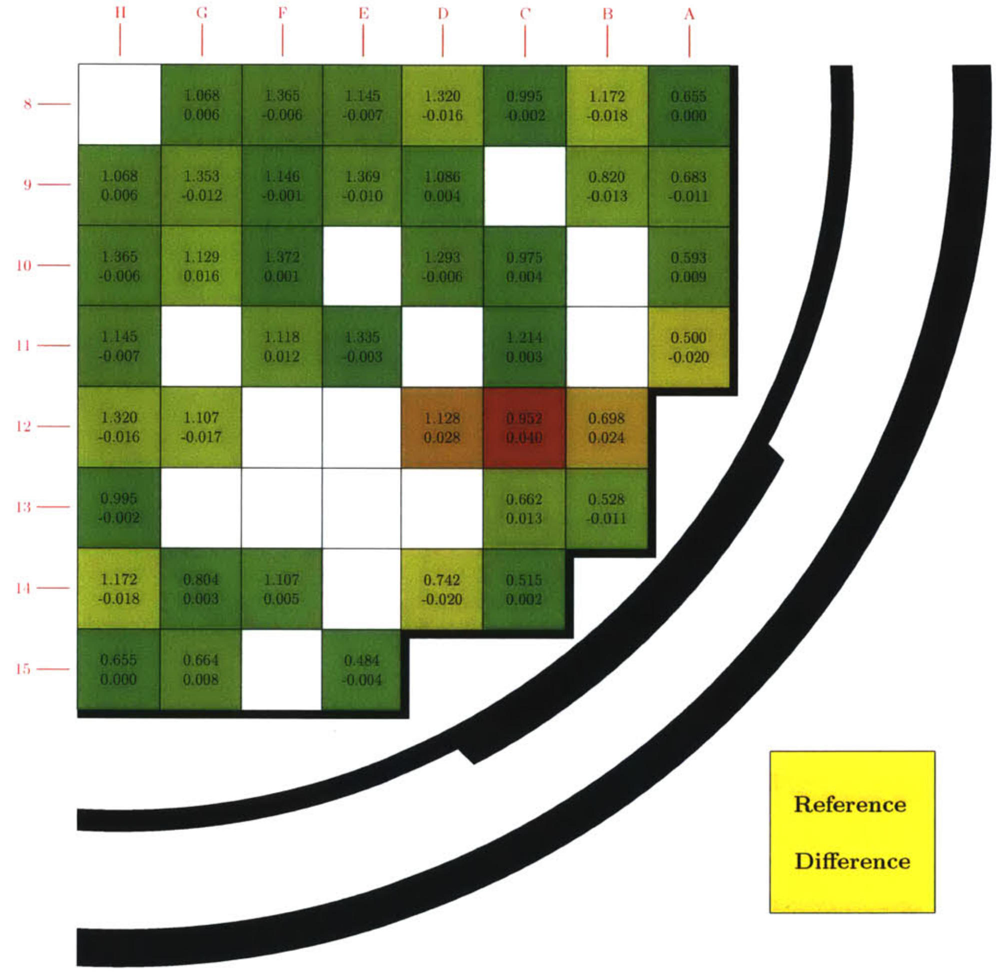

	H	G	F	E	D	C	B	A
8		1.068 0.006	1.365 -0.006	1.145 -0.007	1.320 -0.016	0.995 -0.002	1.172 -0.018	0.655 0.000
9	1.068 0.006	1.353 -0.012	1.146 -0.001	1.369 -0.010	1.086 0.004		0.820 -0.013	0.683 -0.011
10	1.365 -0.006	1.129 0.016	1.372 0.001		1.293 -0.006	0.975 0.004		0.593 0.009
11	1.145 -0.007		1.118 0.012	1.335 -0.003		1.214 0.003		0.500 -0.020
12	1.320 -0.016	1.107 -0.017			1.128 0.028	0.952 0.040	0.698 0.024	
13	0.995 -0.002					0.662 0.013	0.528 -0.011	
14	1.172 -0.018	0.804 0.003	1.107 0.005		0.742 -0.020	0.515 0.002		
15	0.655 0.000	0.664 0.008		0.484 -0.004				

Figure 3-10: Difference in SIMULATE-3 2D model reaction rates relative to measured data at 2.16 GWd/T exposure in cycle 1. The RMS error is 0.0131.

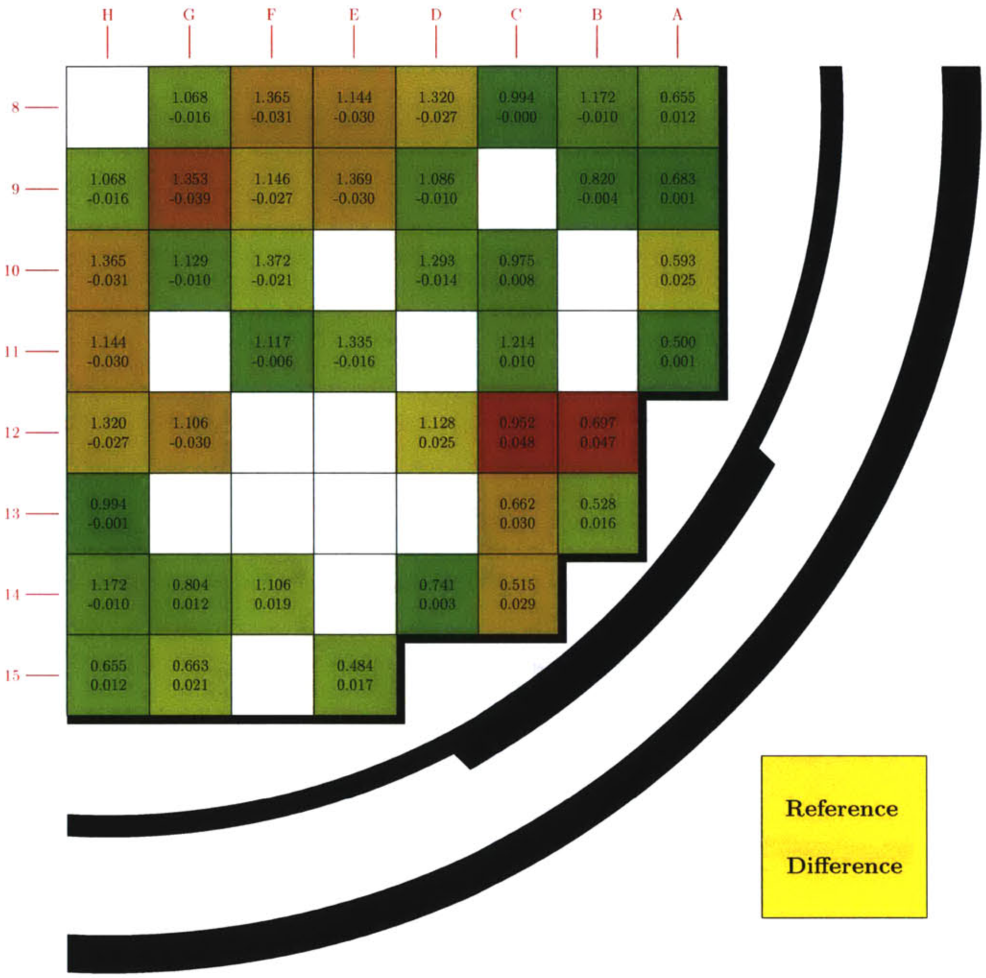

	H	G	F	E	D	C	B	A
8		1.068 -0.016	1.365 -0.031	1.144 -0.030	1.320 -0.027	0.994 -0.000	1.172 -0.010	0.655 0.012
9	1.068 -0.016	1.353 -0.039	1.146 -0.027	1.369 -0.030	1.086 -0.010		0.820 -0.004	0.683 0.001
10	1.365 -0.031	1.129 -0.010	1.372 -0.021		1.293 -0.014	0.975 0.008		0.593 0.025
11	1.144 -0.030		1.117 -0.006	1.335 -0.016		1.214 0.010		0.500 0.001
12	1.320 -0.027	1.106 -0.030			1.128 0.025	0.952 0.048	0.697 0.047	
13	0.994 -0.001					0.662 0.030	0.528 0.016	
14	1.172 -0.010	0.804 0.012	1.106 0.019		0.741 0.003	0.515 0.029		
15	0.655 0.012	0.663 0.021		0.484 0.017				

Figure 3-11: Difference in reaction rates of the CASMO-5 M×N model without axial buckling relative to measured data at 2.16 GWd/T exposure in cycle 1. The RMS error is 0.0224.

decrease. This model with the axial buckling is the final model selected for CASMO-5 M×N analysis. The comparison with measured data is shown in Fig. 3-12 and the RMS errors slightly increase. This is unfortunate, however we choose to continue with this model since the lower RMS error observed without axial buckling in Fig. 3-11 is likely from cancellation of error that may not occur at other statepoints.

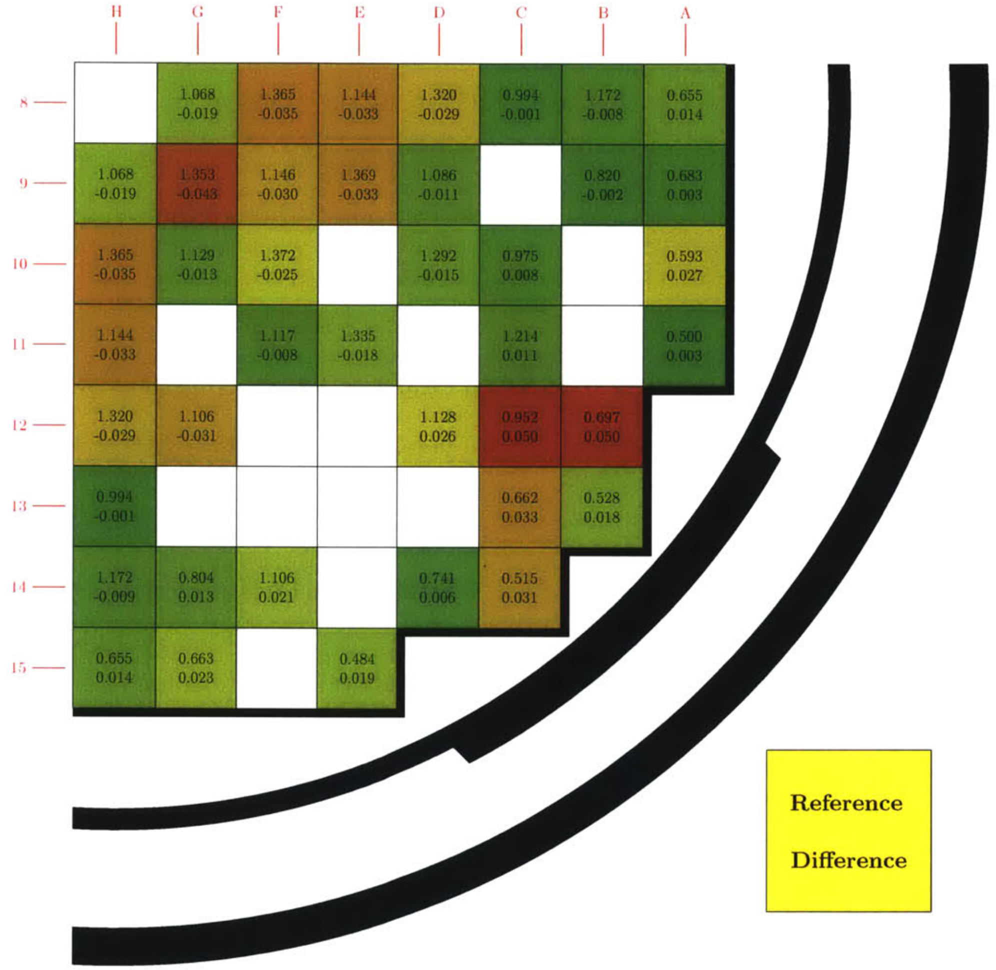

	H	G	F	E	D	C	B	A
8		1.068 -0.019	1.365 -0.035	1.144 -0.033	1.320 -0.029	0.994 -0.001	1.172 -0.008	0.655 0.014
9	1.068 -0.019	1.353 -0.043	1.146 -0.030	1.369 -0.033	1.086 -0.011		0.820 -0.002	0.683 0.003
10	1.365 -0.035	1.129 -0.013	1.372 -0.025		1.292 -0.015	0.975 0.008		0.593 0.027
11	1.144 -0.033		1.117 -0.008	1.335 -0.018		1.214 0.011		0.500 0.003
12	1.320 -0.029	1.106 -0.031			1.128 0.026	0.952 0.050	0.697 0.050	
13	0.994 -0.001					0.662 0.033	0.528 0.018	
14	1.172 -0.009	0.804 0.013	1.106 0.021		0.741 0.006	0.515 0.031		
15	0.655 0.014	0.663 0.023		0.484 0.019				

Figure 3-12: Difference in CASMO-5 M×N model reaction rates relative to measured data at 2.16 GWd/T exposure in cycle 1. The RMS error is 0.0244.

3.3 CASMO-5 M×N Geometry Considerations

CASMO-5 M×N is structured such that only reflected boundary conditions can be used. As mentioned in Chapter 2, this is not a significant issue for cycle 1 due to the octant core symmetry. This allows for quarter-core simulation with reflected boundary conditions to be accurate. However, in cycle 2 the core is loaded quarter-core rotationally symmetric. Therefore, we cannot use quarter-core simulations with reflected boundary conditions and we must use full-core simulation. This significantly increases the run-time. Therefore, cycle 2 is conducted with a lower number of polar angles. To compensate for potential loss of accuracy, the more accurate TY quadrature set [11] is used, which has been derived for 3 polar angles. Even with the computational work reduced with the reduction in the number of polar angles, the computational requirements for cycle 2 are still large. In cycle 1 the computational time per statepoint is $\approx$ 30 minutes, whereas in cycle 2 the computational time per statepoint is $\approx$ 150 minutes. Given that in this study approximately 600 statepoints calculations are needed ($\approx$ 250 depletion points plus 2 cycles × 3 flux maps per cycle × 3 batches per flux map × 20 perturbations per batch), the increase in run-time is significant. Simulation parameters of both cycles for CASMO-5 M×N are given in Table 3.1.

Table 3.1: CASMO-5 M×N Simulation Parameters

	Azimuthal Angles	Ray Spacing	Polar Angles	Polar Quadrature	Energy Groups	Geometry
Cycle 1	32	0.1 cm	5	Gauss-Legendre	35	quarter-core
Cycle 2	32	0.1 cm	3	TY	35	full-core

A graphical description of the modeling process is presented in Fig. 3-13. Notice that both the SIMULATE-3 and CASMO-5 M×N model start from the same 495 group cross-section library.

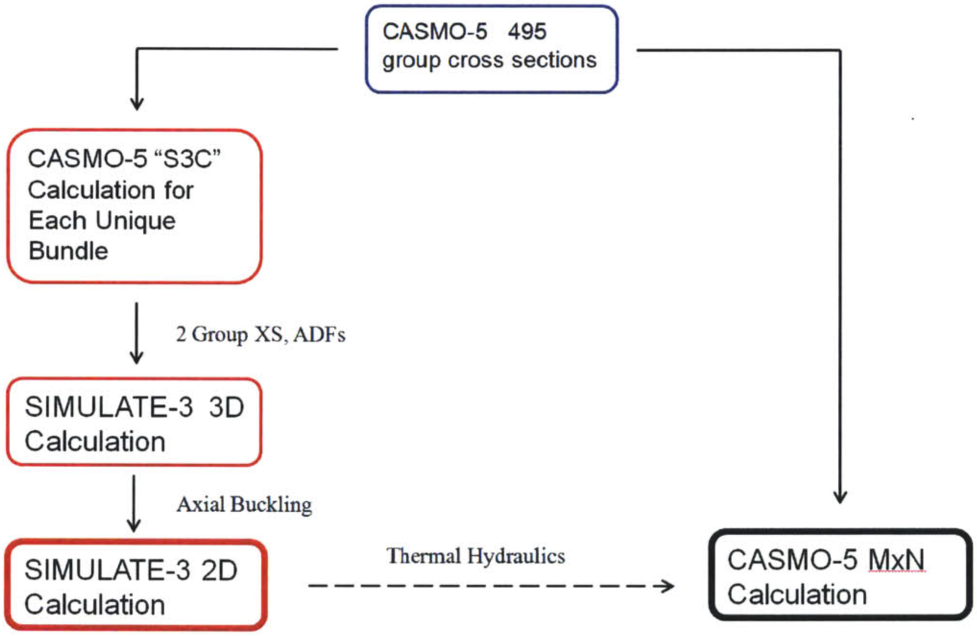

Figure 3-13: Flow chart for SIMULATE-3 and CASMO-5 M×N modeling. Note that CASMO-5 uses the 495 group structure for self-shielding calculations but collapses cross sections to a 35 group structure for transport calculations.

Chapter 4

Standard Model Results

The previous chapter concluded with comparisons of SIMULATE-3 model with measured data in Fig. 3-10 and CASMO-5 M×N with measured data in Fig. 3-12. In this chapter more comparisons with measured data are provided throughout cycles 1 and 2. This includes both hot zero power (HZP) results and HFP results at various depletion steps.

4.1 Hot Zero Power Results

The BEAVRS benchmark supplies critical boron data and measured fission rate distributions at HZP conditions. For cycle 1, the critical boron is documented to be 975 ppm. The most detailed model is the SIMULATE-3 3D model with full axial detail. Comparison with measured data is shown in Fig. 4-1.

Notice that the model is in reasonable agreement with measured data but the well-know tilt in measured radial fission rates makes the difference much larger at this HZP point than observed for later HFP fission rate maps [12]. Since the physical reactor description is nearly symmetric as instrument tube locations are the only known radial asymmetry and the computational models are all symmetric, the measured fission rates should be corrected for any gross geometrical tilt before comparing with calculations. One method for performing such a correction is to assume a planar tilt of fission rates and use the detector signals at symmetric geometrical positions to

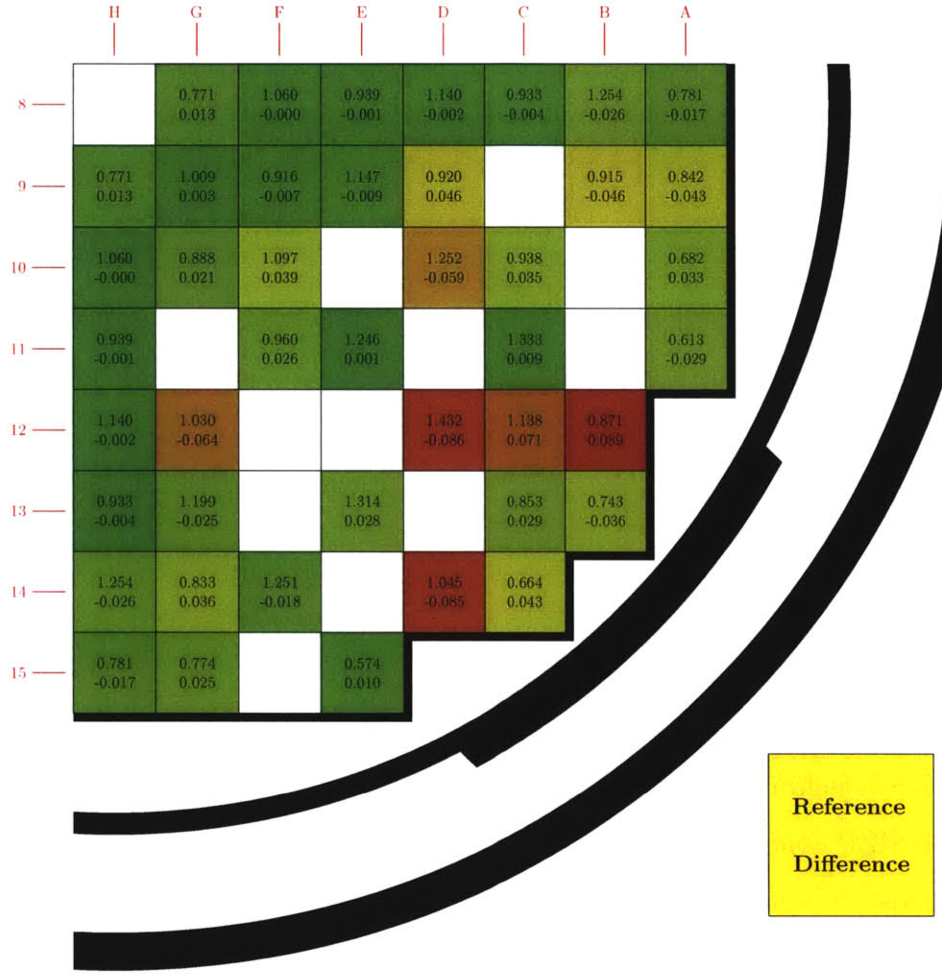

	H	G	F	E	D	C	B	A
8		0.771 0.013	1.060 -0.000	0.939 -0.001	1.140 -0.002	0.933 -0.004	1.254 -0.026	0.781 -0.017
9	0.771 0.013	1.009 0.003	0.916 -0.007	1.147 -0.009	0.920 0.046		0.915 -0.046	0.842 -0.043
10	1.060 -0.000	0.888 0.021	1.097 0.039		1.252 -0.059	0.938 0.035		0.682 0.033
11	0.939 -0.001		0.960 0.026	1.246 0.001		1.333 0.009		0.613 -0.029
12	1.140 -0.002	1.030 -0.064			1.432 -0.086	1.138 0.071	0.871 0.089	
13	0.933 -0.004	1.199 -0.025		1.314 0.028		0.853 0.029	0.743 -0.036	
14	1.254 -0.026	0.833 0.036	1.251 -0.018		1.045 -0.085	0.664 0.043		
15	0.781 -0.017	0.774 0.025		0.574 0.010				

Figure 4-1: Difference in reaction rates of the SIMULATE-3 3D model relative to measured data at hot zero power (HZP) conditions in cycle 1. The RMS error is 0.0364.

deduce the magnitude and orientation of the plane of tilt that minimizes deviations of symmetric detector fission rates relative to that plane.

Using this "tilt-correted" fission rate distribution, comparisons of SIMULATE-3 and measured fission rate distributions are displayed in Fig. 4-2.

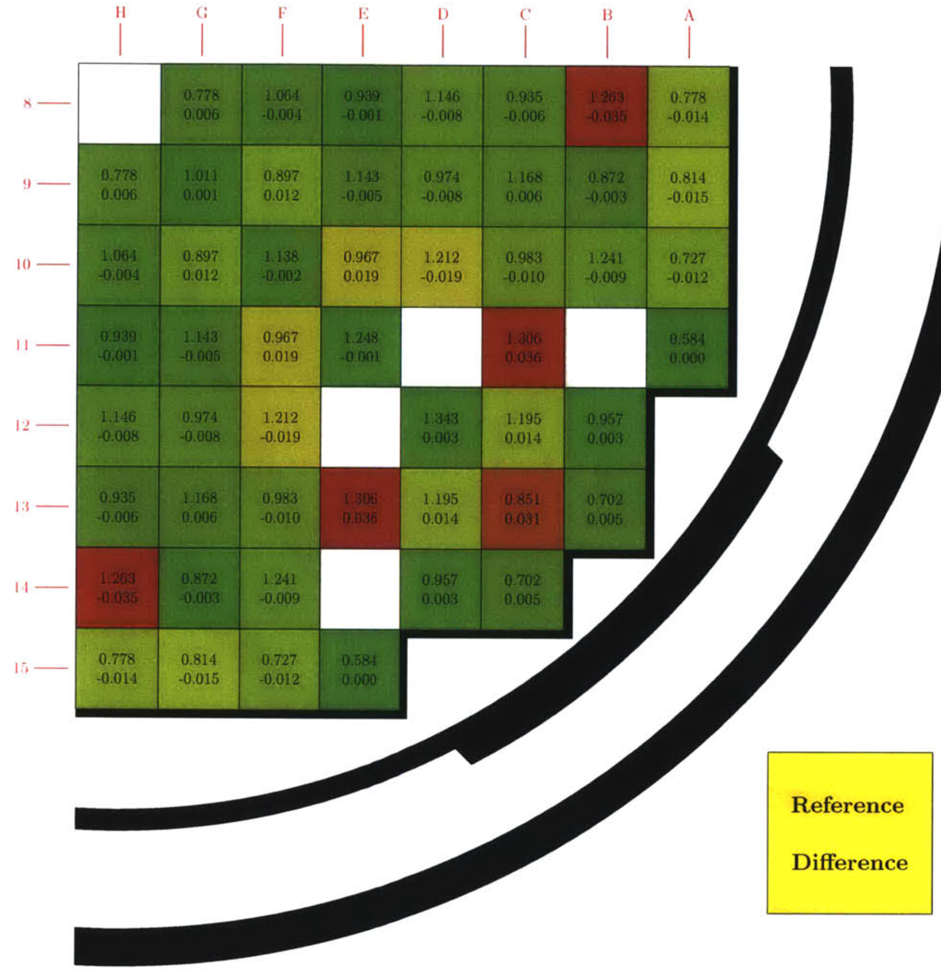

	H	G	F	E	D	C	B	A
8		0.778 0.006	1.064 -0.004	0.939 -0.001	1.146 -0.008	0.935 -0.006	1.263 -0.035	0.778 -0.014
9	0.778 0.006	1.011 0.001	0.897 0.012	1.143 -0.005	0.974 -0.008	1.168 0.006	0.872 -0.003	0.814 -0.015
10	1.064 -0.004	0.897 0.012	1.138 -0.002	0.967 0.019	1.212 -0.019	0.983 -0.010	1.241 -0.009	0.727 -0.012
11	0.939 -0.001	1.143 -0.005	0.967 0.019	1.248 -0.001		1.306 0.036		0.584 0.000
12	1.146 -0.008	0.974 -0.008	1.212 -0.019		1.343 0.003	1.195 0.014	0.957 0.003	
13	0.935 -0.006	1.168 0.006	0.983 -0.010	1.306 0.036	1.195 0.014	0.851 0.031	0.702 0.005	
14	1.263 -0.035	0.872 -0.003	1.241 -0.009		0.957 0.003	0.702 0.005		
15	0.778 -0.014	0.814 -0.015	0.727 -0.012	0.584 0.000				

Figure 4-2: Difference in SIMULATE-3 3D model reaction rates relative to measured data with a linear tilt correction at hot zero power (HZP) conditions in cycle 1. The RMS error is 0.0142.

With the linear correction to the measured data, the simulated fission rate errors are significantly lower. It is important to note that with the linear correction, the measured data is eighth-core symmetric. This causes the resulting error distribution to be symmetric. Since the linearly corrected data provides better insight into the accuracy of the HZP simulations, further HZP comparisons are relative to the linearly corrected data. Fission rate error distributions without the linear correction are presented in Appendix A.

Removing axial geometrical variation, the 3D ARO model at zero power is compared with the linearly corrected measured data and presented in Fig. 4-3. Notice the result is very similar to the model with full axial detail.

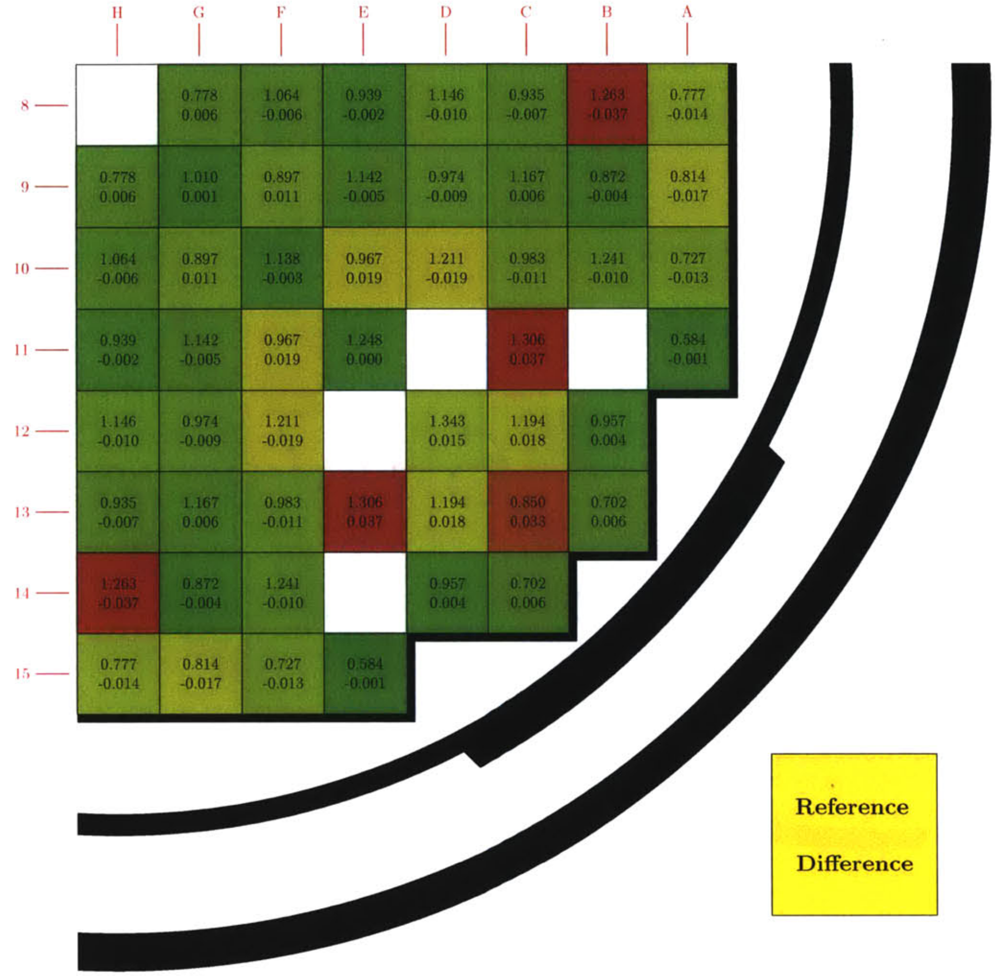

	H	G	F	E	D	C	B	A
8		0.778 0.006	1.064 -0.006	0.939 -0.002	1.146 -0.010	0.935 -0.007	1.263 -0.037	0.777 -0.014
9	0.778 0.006	1.010 0.001	0.897 0.011	1.142 -0.005	0.974 -0.009	1.167 0.006	0.872 -0.004	0.814 -0.017
10	1.064 -0.006	0.897 0.011	1.138 -0.003	0.967 0.019	1.211 -0.019	0.983 -0.011	1.241 -0.010	0.727 -0.013
11	0.939 -0.002	1.142 -0.005	0.967 0.019	1.248 0.000		1.306 0.037		0.584 -0.001
12	1.146 -0.010	0.974 -0.009	1.211 -0.019		1.343 0.015	1.194 0.018	0.957 0.004	
13	0.935 -0.007	1.167 0.006	0.983 -0.011	1.306 0.037	1.194 0.018	0.850 0.033	0.702 0.006	
14	1.263 -0.037	0.872 -0.004	1.241 -0.010		0.957 0.004	0.702 0.006		
15	0.777 -0.014	0.814 -0.017	0.727 -0.013	0.584 -0.001				

Figure 4-3: Difference in SIMULATE-3 3D ARO model reaction rates relative to measured data with a linear tilt correction at hot zero power (HZP) conditions in cycle 1. The RMS error is 0.0152.

Now the final 2D models in SIMULATE-3 and CASMO-5 M×N are examined. The HZP error distribution for the SIMULATE-3 model is shown in Fig. 4-4 and for the CASMO-5 M×N model in Fig. 4-5. The error distributions are very similar to the 3D models.

Notice that the CASMO-5 error is less than SIMULATE-3 when the linear correction is applied to the data. The linear tilt in the measured data naturally decreases with depletion of the core so its effect is less important. The presence of the tilt might be of concern for inferring the bias in reactivity decrement. However, since all reactivity perturbations conducted in this analysis are symmetric, the tilt should have little effect as a symmetric perturbation cannot remove the tilt.

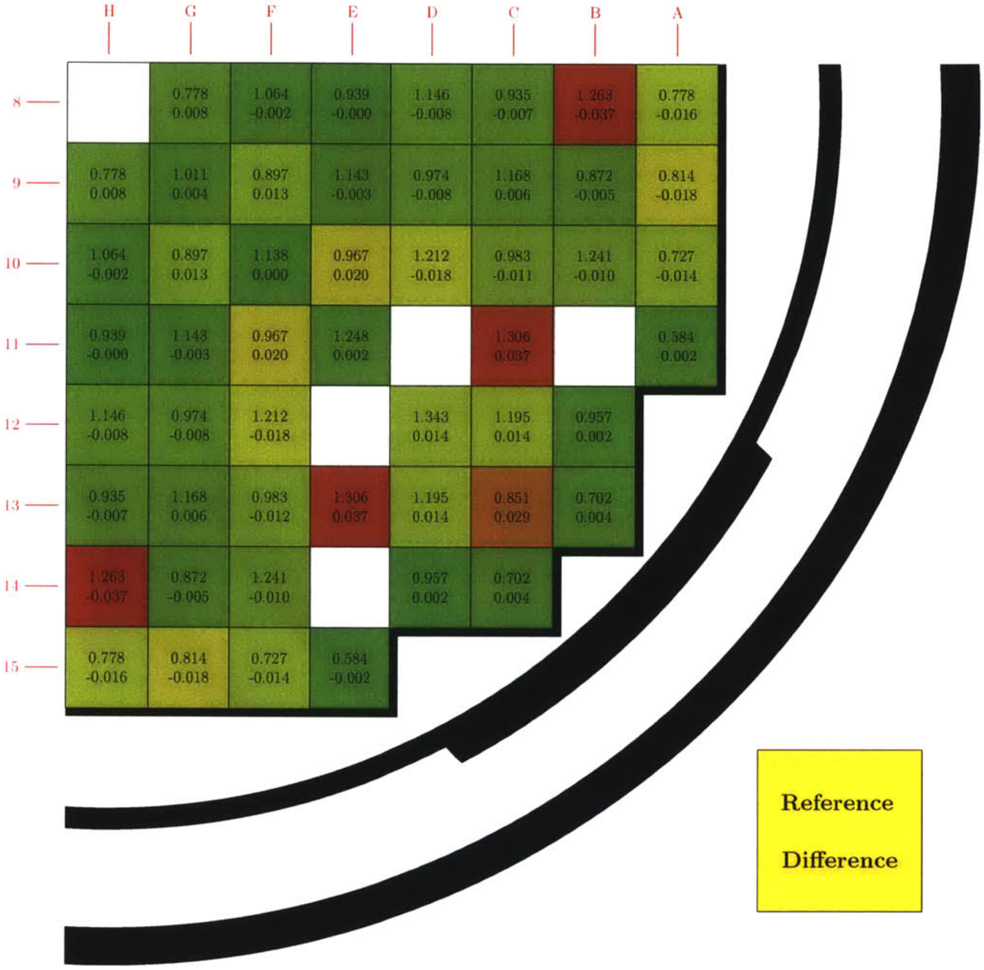

	H	G	F	E	D	C	B	A
8		0.778 0.008	1.064 -0.002	0.939 -0.000	1.146 -0.008	0.935 -0.007	1.263 -0.037	0.778 -0.016
9	0.778 0.008	1.011 0.004	0.897 0.013	1.143 -0.003	0.974 -0.008	1.168 0.006	0.872 -0.005	0.814 -0.018
10	1.064 -0.002	0.897 0.013	1.138 0.000	0.967 0.020	1.212 -0.018	0.983 -0.011	1.241 -0.010	0.727 -0.014
11	0.939 -0.000	1.143 -0.003	0.967 0.020	1.248 0.002		1.306 0.037		0.584 -0.002
12	1.146 -0.008	0.974 -0.008	1.212 -0.018		1.343 0.014	1.195 0.014	0.957 0.002	
13	0.935 -0.007	1.168 0.006	0.983 -0.012	1.306 0.037	1.195 0.014	0.851 0.029	0.702 0.004	
14	1.263 -0.037	0.872 -0.005	1.241 -0.010		0.957 0.002	0.702 0.004		
15	0.778 -0.016	0.814 -0.018	0.727 -0.014	0.584 -0.002				

Figure 4-4: Difference in SIMULATE-3 2D model reaction rates relative to measured data with a linear tilt correction at hot zero power (HZP) conditions in cycle 1. The RMS error is 0.0150.

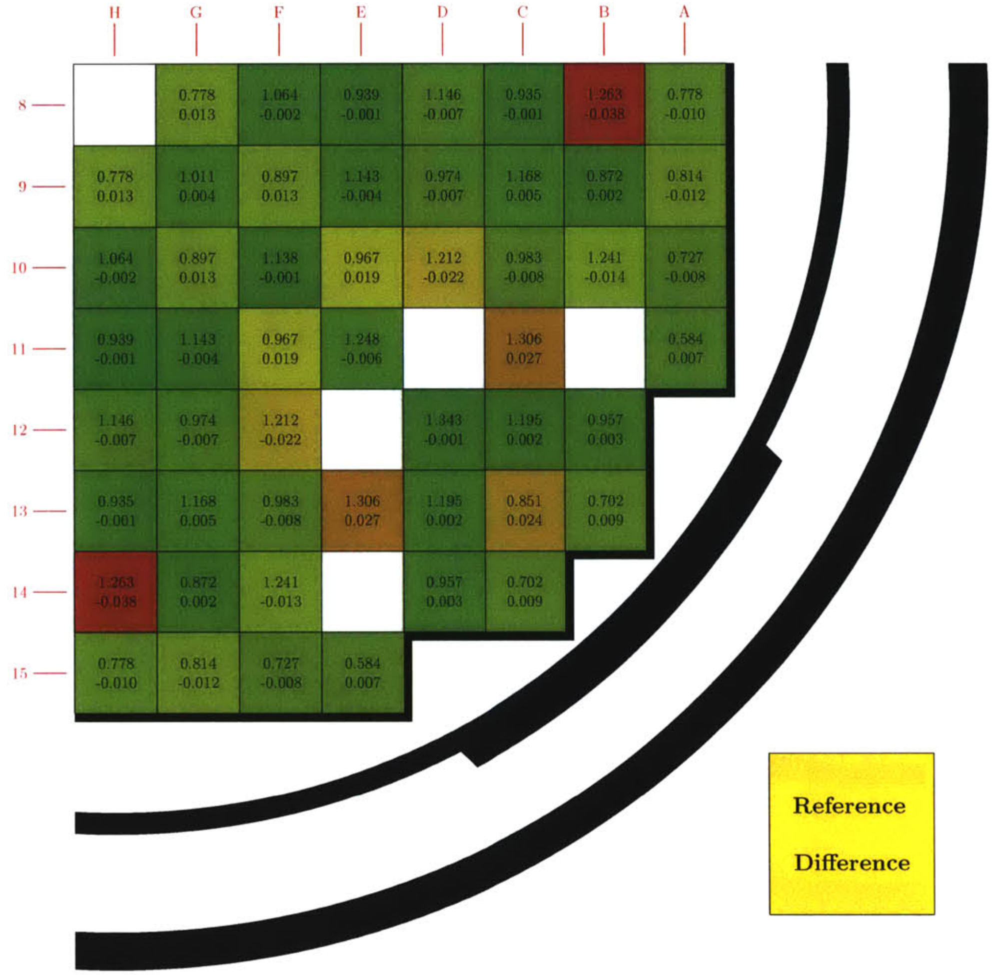

	H	G	F	E	D	C	B	A
8		0.778 0.013	1.064 -0.002	0.939 -0.001	1.146 -0.007	0.935 -0.001	1.263 -0.038	0.778 -0.010
9	0.778 0.013	1.011 0.004	0.897 0.013	1.143 -0.004	0.974 -0.007	1.168 0.005	0.872 0.002	0.814 -0.012
10	1.064 -0.002	0.897 0.013	1.138 -0.001	0.967 0.019	1.212 -0.022	0.983 -0.008	1.241 -0.014	0.727 -0.008
11	0.939 -0.001	1.143 -0.004	0.967 0.019	1.248 -0.006		1.306 0.027		0.584 0.007
12	1.146 -0.007	0.974 -0.007	1.212 -0.022		1.343 -0.001	1.195 0.002	0.957 0.003	
13	0.935 -0.001	1.168 0.005	0.983 -0.008	1.306 0.027	1.195 0.002	0.851 0.024	0.702 0.009	
14	1.263 -0.038	0.872 0.002	1.241 -0.013		0.957 0.003	0.702 0.009		
15	0.778 -0.010	0.814 -0.012	0.727 -0.008	0.584 0.007				

Figure 4-5: Difference in the CASMO-5 M×N model reaction rates relative to measured data with a linear tilt correction at hot zero power (HZP) conditions in cycle 1. The RMS error is 0.0134.

4.2 Cycle 1 HFP Results

Now we return to comparisons without the linear correction to measured data. Previously, HFP results for both the final SIMULATE-3 model and the final CASMO-5 M×N model were shown in Fig. 3-10 and Fig. 3-12 respectively for the beginning of cycle and now results from cycle depletion cases are analyzed. The total cycle length for cycle 1 is 13.6 GWd/T. Statepoints are selected to represent beginning, middle, and end of cycle behavior. These statepoints are chosen at burnups of 2.16, 7.51, and 11.08 GWd/T respectively. The middle of cycle result for CASMO-5 M×N is shown in Fig. 4-6.

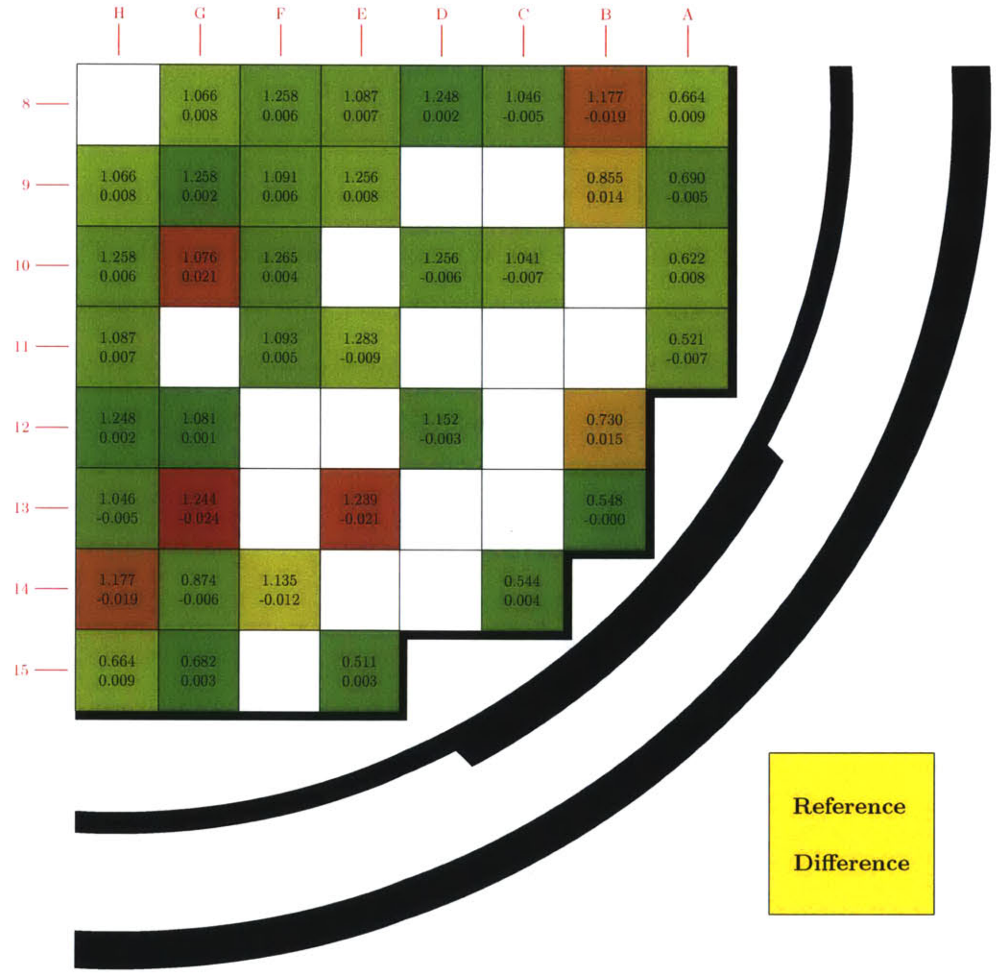

	H	G	F	E	D	C	B	A
8		1.066 0.008	1.258 0.006	1.087 0.007	1.248 0.002	1.046 -0.005	1.177 -0.019	0.664 0.009
9	1.066 0.008	1.258 0.002	1.091 0.006	1.256 0.008			0.855 0.014	0.690 -0.005
10	1.258 0.006	1.076 0.021	1.265 0.004		1.256 -0.006	1.041 -0.007		0.622 0.008
11	1.087 0.007		1.093 0.005	1.283 -0.009				0.521 -0.007
12	1.248 0.002	1.081 0.001			1.152 -0.003		0.730 0.015	
13	1.046 -0.005	1.244 -0.024		1.239 -0.021			0.548 -0.000	
14	1.177 -0.019	0.874 -0.006	1.135 -0.012			0.544 0.004		
15	0.664 0.009	0.682 0.003		0.511 0.003				

Figure 4-6: Difference in CASMO-5 M×N model reaction rates relative to measured data at 7.51 GWd/T exposure in cycle 1. The RMS error is 0.0100.

Results show that after significant depletion of the fuel, the RMS error significantly decreases. This is partly due to the tendency of error distributions to "burn out." If a model predicts a higher than actual fission rate in a certain region of the reactor core, that region will deplete more rapidly causing its reactivity to decrease. This causes the fission rate in that region to then eventually decrease and be more consistent with the actual behavior. However, the BEAVRS cycle 1 measured fission rates are noticeably tilted between the four different core quadrants, and this can not be captured in a quarter-core symmetric computational model. Additional fission rate comparisons with measured data can be found in Appendix B.

At each near HFP statepoint it is possible to present fission rate error distribution plots similar to those presented previously. When the RMS error of every statepoint is extracted, a description of model accuracy relative to measured data throughout the cycle can be formed, as presented in Fig. 4-7.

Notice that the CASMO-5 M×N model has a greater RMS error at the beginning of cycle as compared with SIMULATE-3 ARO models, both 2D and 3D. The BEAVRS measured quadrant tilt is responsible for much of the larger RMS deviations observed in the early cycle points, and the tilt rapidly diminishes during the cycle. By middle of cycle, the CASMO-5 M×N results are comparable with SIMULATE-3.

4.3 Cycle 2 HFP Results

For cycle 2 results in this section, we choose to focus on the beginning of cycle results. These results are shown in Fig. 4-8 and Fig. 4-9 for SIMULATE-3 and CASMO-5 M×N respectively.

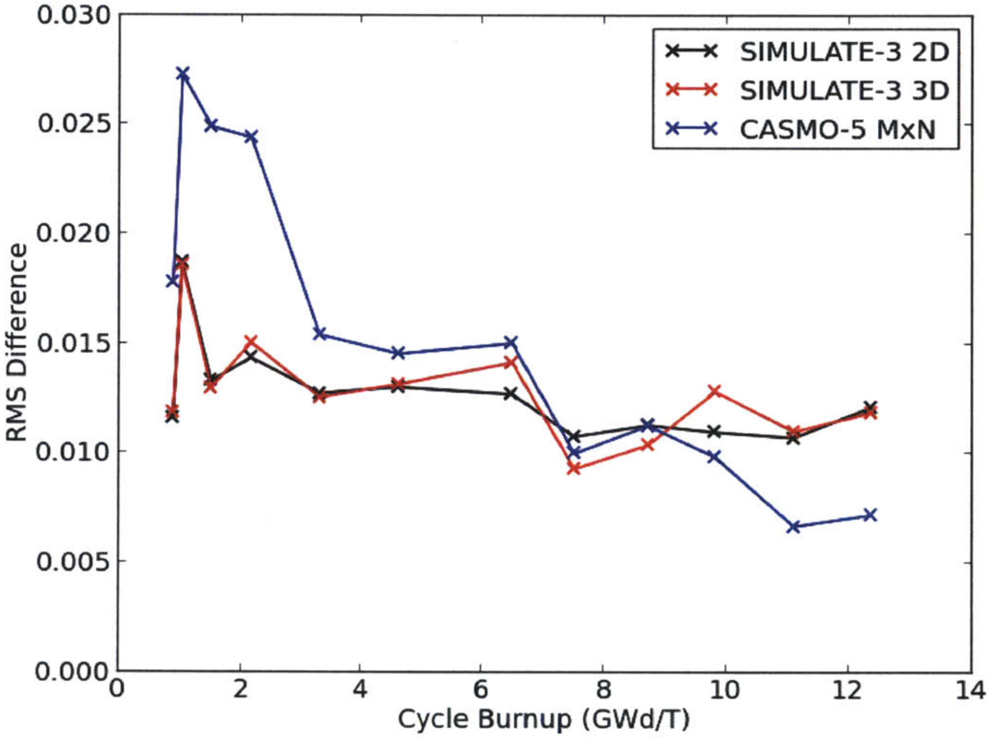

Figure 4-7: Normalized fission rate RMS error with respect to measured data in cycle 1 as a function of burnup.

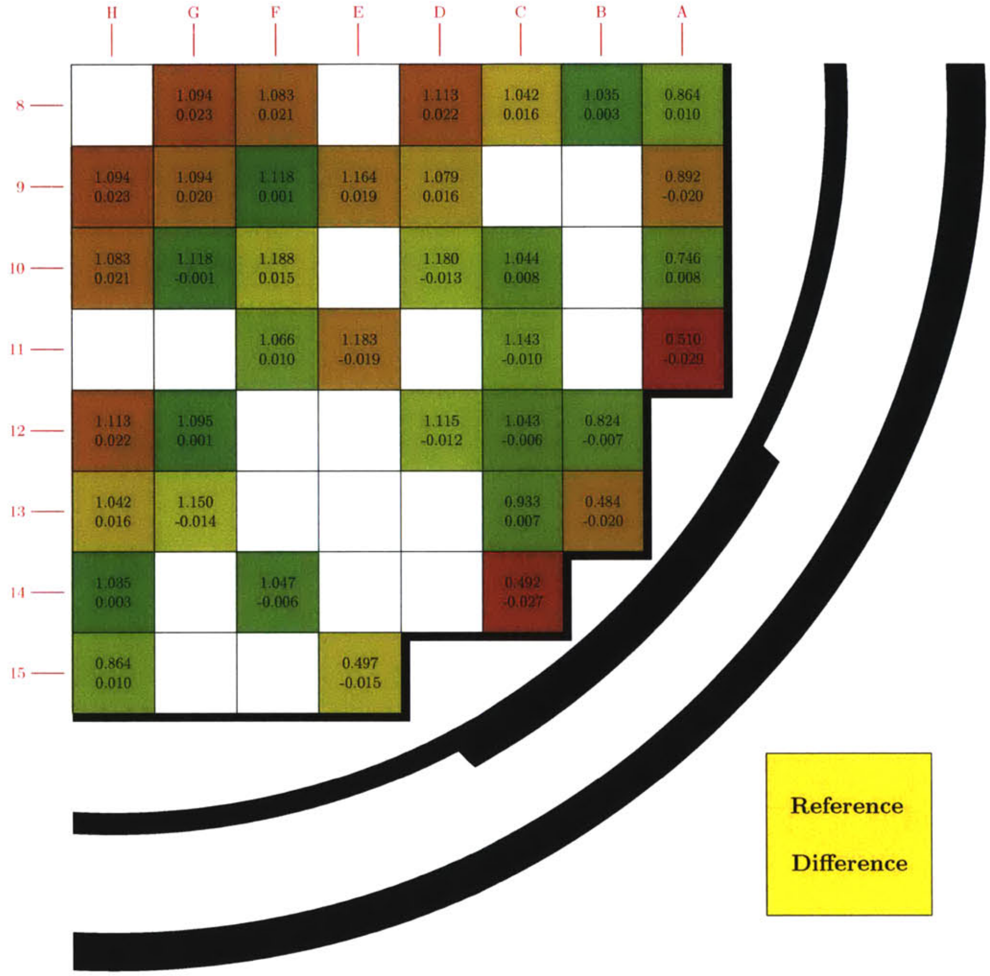

	H	G	F	E	D	C	B	A
8		1.094 0.023	1.083 0.021		1.113 0.022	1.042 0.016	1.035 0.003	0.864 0.010
9	1.094 0.023	1.094 0.020	1.118 0.001	1.164 0.019	1.079 0.016			0.892 -0.020
10	1.083 0.021	1.118 -0.001	1.188 0.015		1.180 -0.013	1.044 0.008		0.746 0.008
11			1.066 0.010	1.183 -0.019		1.143 -0.010		0.510 -0.029
12	1.113 0.022	1.095 0.001			1.115 -0.012	1.043 -0.006	0.824 -0.007	
13	1.042 0.016	1.150 -0.014				0.933 0.007	0.484 -0.020	
14	1.035 0.003		1.047 -0.006			0.492 -0.027		
15	0.864 0.010			0.497 -0.015				

Figure 4-8: Difference in SIMULATE-3 2D model reaction rates relative to measured data at 2.11 GWd/T cycle exposure in cycle 2. The RMS error is 0.0157.

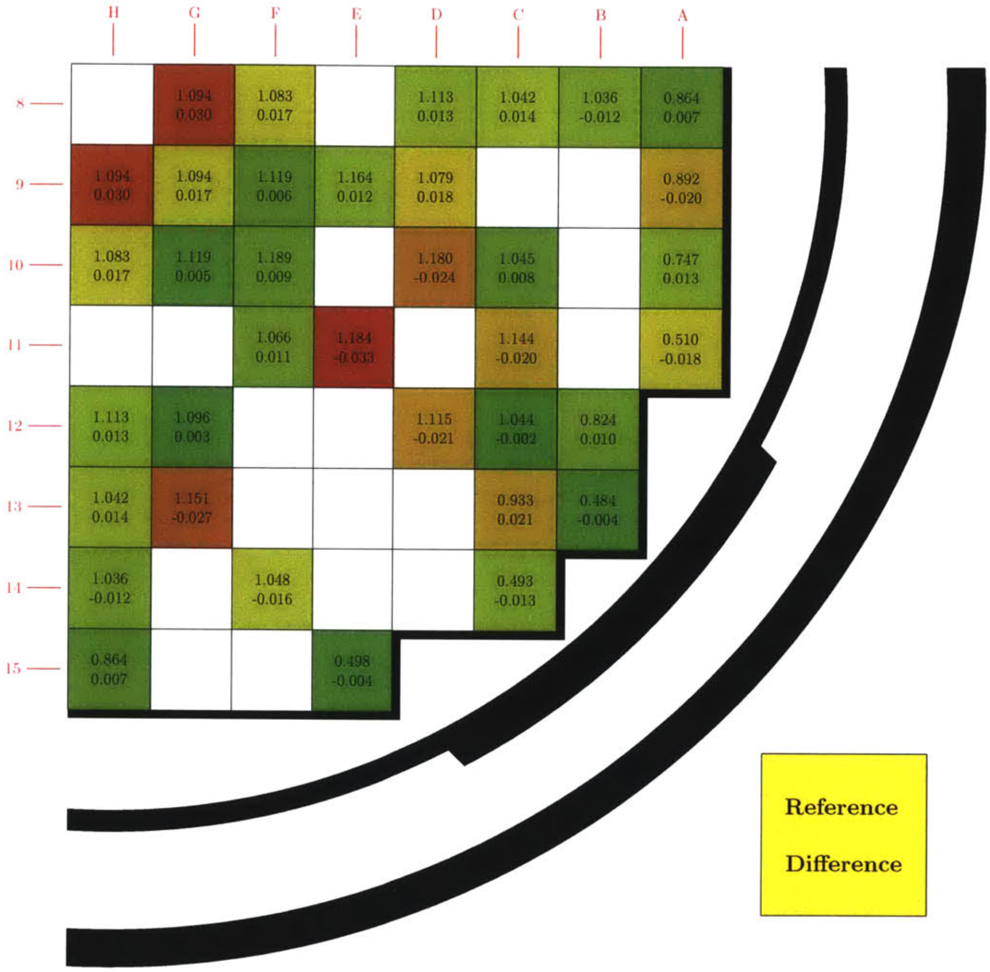

	H	G	F	E	D	C	B	A
8		1.094 0.030	1.083 0.017		1.113 0.013	1.042 0.014	1.036 -0.012	0.864 0.007
9	1.094 0.030	1.094 0.017	1.119 0.006	1.164 0.012	1.079 0.018			0.892 -0.020
10	1.083 0.017	1.119 0.005	1.189 0.009		1.180 -0.024	1.045 0.008		0.747 0.013
11			1.066 0.011	1.184 -0.033		1.144 -0.020		0.510 -0.018
12	1.113 0.013	1.096 0.003			1.115 -0.021	1.044 -0.002	0.824 0.010	
13	1.042 0.014	1.151 -0.027				0.933 0.021	0.484 -0.004	
14	1.036 -0.012		1.048 -0.016			0.493 -0.013		
15	0.864 0.007			0.498 -0.004				

Figure 4-9: Difference in CASMO-5 M×N model reaction rates relative to measured data at 2.11 GWd/T cycle exposure in cycle 2. The RMS error is 0.0165.

Notice that in cycle 2 the beginning of cycle RMS errors are very comparable between SIMULATE-3 and CASMO-5 M×N. Additional fission rate comparisons with measured data for cycle 2 can be found in Appendix ??. The RMS error trends during cycle 2 of the SIMULATE-3 and CASMO-5 M×N models are presented in Fig. 4-10. The error trends are far flatter in cycle 2 and CASMO-5 M×N is comparable with SIMULATE-3 results throughout all statepoints.

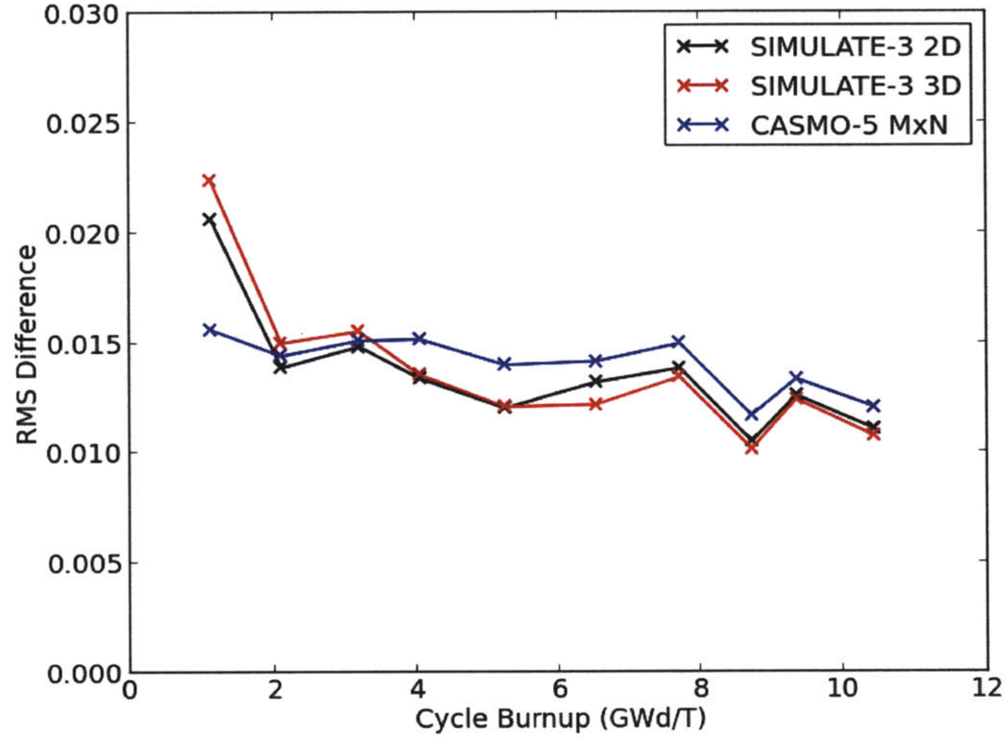

Figure 4-10: Normalized fission rate RMS error with respect to measured data in cycle 2 as a function of burnup. SIMULATE-3 3D refers to the SIMULATE-3 ARO model.

Chapter 5

Inferring Reactivity Decrements

Given the computational requirements for performing full-core CASMO-5 M×N cases, three flux maps from each cycle were selected to compare errors in inferred fuel reactivity depletion decrements using 2D SIMULATE-3 and 2D CASMO-5 M×N perturbation cases.

5.1 Methodology

In order to determine inferred reactivity of the fuel, a series of perturbations are conducted on sub-batch burnup as was done in the original EPRI study[2]. The perturbation which yields fission rates with closest agreement with measured data is assumed to correspond to the best estimate for the reactivity of the fuel. In particular, for a given statepoint the fuel from a particular sub-batch is loaded from an altered cycle burnup point. This allows the fuel reactivity to be altered to determine the sub-batch reactivity that produces the best agreement with measure fission rate distributions. The altered sub-batch burnup points are chosen to range from -1.0 GWd/T to +1.0 GWd/T relative to the unaltered burnup point in steps of 0.1 GWd/T. An example perturbation is shown in Fig. 5-1 where the closest agreement with measured data corresponding with minimal RMS error occurs three steps away from the unperturbed solution.

This method of sweeping the perturbed batch burnups in the vicinity of the pre-

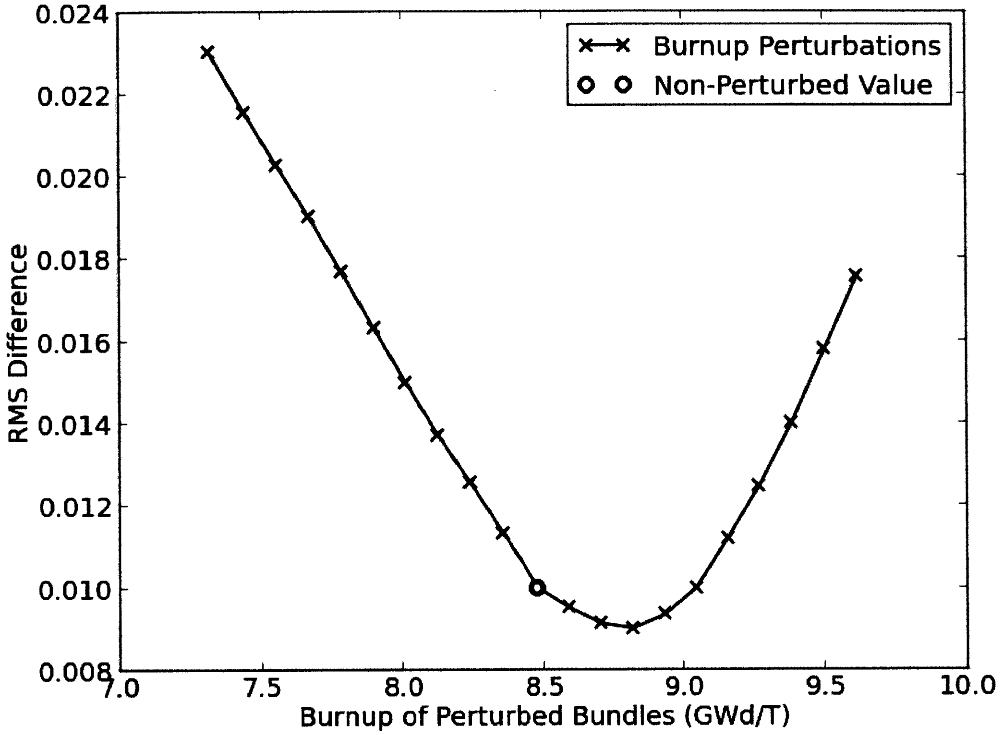

Figure 5-1: Root mean square (RMS) error in fission rate distribution as a function of perturbed fuel batch burnup.

dicted batch burnup is analogous to the procedure used by a previous EPRI/Studsvik study [2] where neutronic data for all nodes of the perturbed batch burnups were perturbed by directly altering nodal model burnups.

In the case of direct CASMO-5 M×N perturbations, pin-wise isotopics are perturbed by directly using pin-wise isotopics from an alternate cycle depletion point to achieve a similar effect to altering the perturbed assembly burnups. All non-perturbed assemblies employ pin-wise isotopics corresponding to the unperturbed flux map depletion state. It should be noted that in CASMO-5 M×N cases, the Xenon concentration of the perturbed states is taken directly from the depletion data unlike the SIMULATE-3 cases that compute equilibrium Xenon concentrations consistent with the perturbed power distributions. This slight difference in procedure is not believed to be significant.

Once the optimal burnup distribution of the fuel sub-batch corresponding to the lowest RMS error is discerned, the difference in burnup from the non-perturbed solution is calculated. This difference is then multiplied by the reactivity worth of burnup to yield the difference in reactivity. The reactivity decrement error $\Delta k_{bias}^{lattice}$ is described in Eq. 5.1

$$\Delta k_{bias}^{lattice}\left(\bar{E}_{base}^{lattice}\right) = -\left(\bar{E}_{min}^{lattice} - \bar{E}_{base}^{lattice}\right)\left(\frac{dk}{dE}\frac{1}{k^2}\right)\Bigg|_{\bar{E}_{base}^{lattice}}^{lattice} \tag{5.1}$$

where k refers to the core critical eigenvalue at the measured boron concentration, E refers to the exposure, $\bar{E}_{base}^{lattice}$ is the average exposure of the fuel batch of interest, and $\bar{E}_{min}^{lattice}$ is the average exposure of the batch after the optimal perturbation (producing the smallest RMS error). The quantity $\left(\frac{dk}{dE}\frac{1}{k^2}\right)\Big|_{\bar{E}_{base}^{lattice}}^{lattice}$ is computed from lattice physics calculations. More specifically, k-infinity as a function of burnup is edited from lattice physics calculations. An example is shown in Fig. 5-2 for a fuel assembly containing 12 burnable poisons. Notice that due to the presence of burnable poisons, reactivity (k-infinity) rises at the beginning of life while the depletion of the burnable poison has a large positive reactivity effect.

There is also an abrupt increase in reactivity when burnable poisons are pulled. With this curve, the quantity $\frac{dk}{dE}\frac{1}{k^2}$ can then be calculated using the central difference approximation. The result is shown in Fig. 5-3, which we generally refer to as the burnup worth.

Similar curves were produced for every unique assembly in the core. By interpolating this curve for the desired burnup step, burnup worth for a particular assembly can be calculated. However, due to varied number of burnable poisons in assemblies, each sub-batch contains several types of unique assemblies and each unique assembly has its own burnup worth. An average burnup worth is calculated for the sub-batch by weighting by the number of each type of unique assembly in the sub-batch.

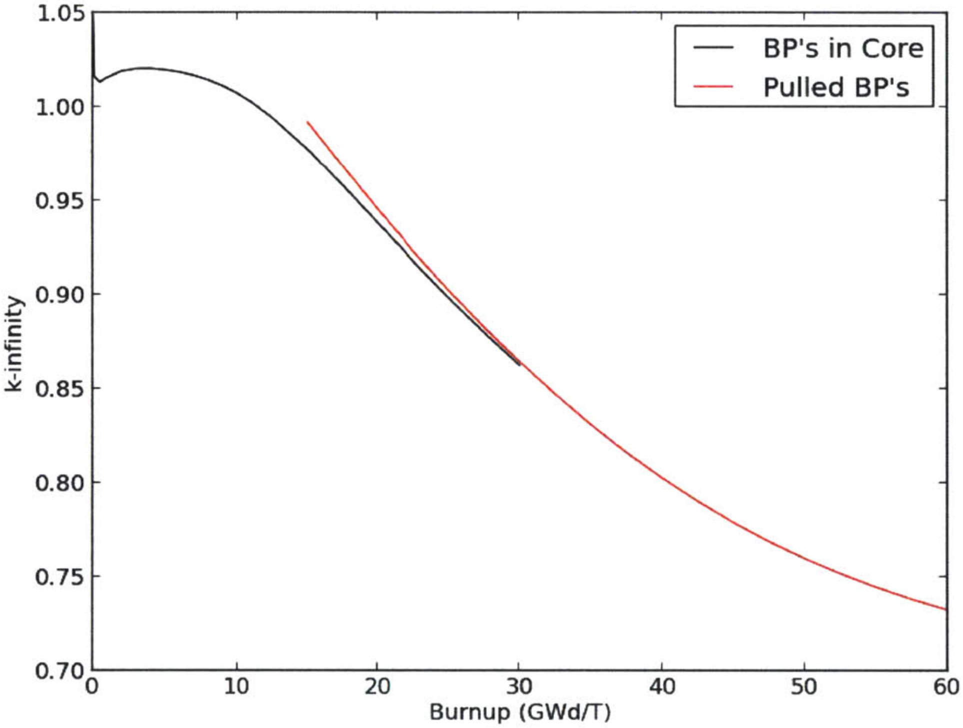

Figure 5-2: Reactivity of an assembly with 2.4% enriched fuel and 12 burnable poisons as a function of burnup.

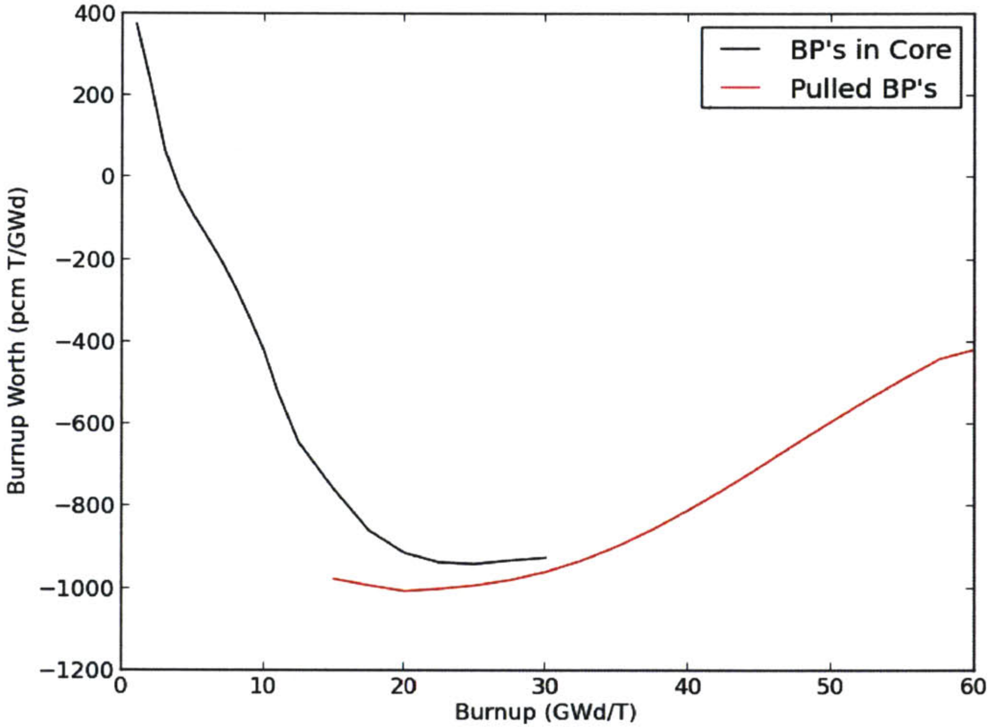

Figure 5-3: Assembly reactivity burnup gradient of an assembly with 2.4% enriched fuel and 12 burnable poisons as a function of burnup.

5.2 Calculating Exposure Differences

After gathering the lattice physics results for reactivity gradient, the optimal burnup distribution needs to be inferred. This is calculated by perturbing the burnup in fuel sub-batches which each consist of 64 assemblies. With these two results, Eq. 5.1 can be used to calculate the bias in reactivity decrement.

5.2.1 Cycle 1 Results

In cycle 1 the three burnup points that are chosen to infer reactivity are 2.16, 7.51, and 11.08 GWd/T. The unperturbed fission rate error distributions were previously shown in Chapters 3 and 4. With these burnup points, our first candidate fuel sub-batch is the 2.4% enriched fuel. As seen from the enrichment distribution presented in Fig. 2-1, the 2.4% enriched fuel is distributed rather evenly throughout the core in 64 assemblies. Resulting RMS trends are shown in Fig. 5-4.

The trend shows the optimal sub-batch burnup is quite far from the unperturbed simulated value. This is due to two effects. First, the RMS error at the beginning of cycle 1 was quite large. Second, due to the presence of many burnable absorbers in the 2.4% enriched fuel, the reactivity decrement attributed to burnup is quite low early in the cycle. As the fuel burns out in assemblies with burnable poisons, so does the burnable poison. These two effects counteract each other leading to a much lower reactivity gradient for low fuel assembly burnups.

Regardless, notice that the perturbation is in the same direction for both CASMO-5 and SIMULATE-3. When a perturbation to higher burnup is observed in CASMO-5, a perturbation to higher burnup is also observed in SIMULATE-3. In addition, the curve shapes and magnitude of perturbation are quite similar.

The next sub-batch is 3.1% enriched fuel which resides mainly along the periphery of the reactor core. The results from these perturbations are presented in Fig. 5-5.

Since fission rate errors present themselves largely in the form of in-out tilts, the slope of the RMS difference curve with perturbed burnup is much greater. In addition, notice that since the CASMO-5 beginning of cycle results involved a large in-out tilt,

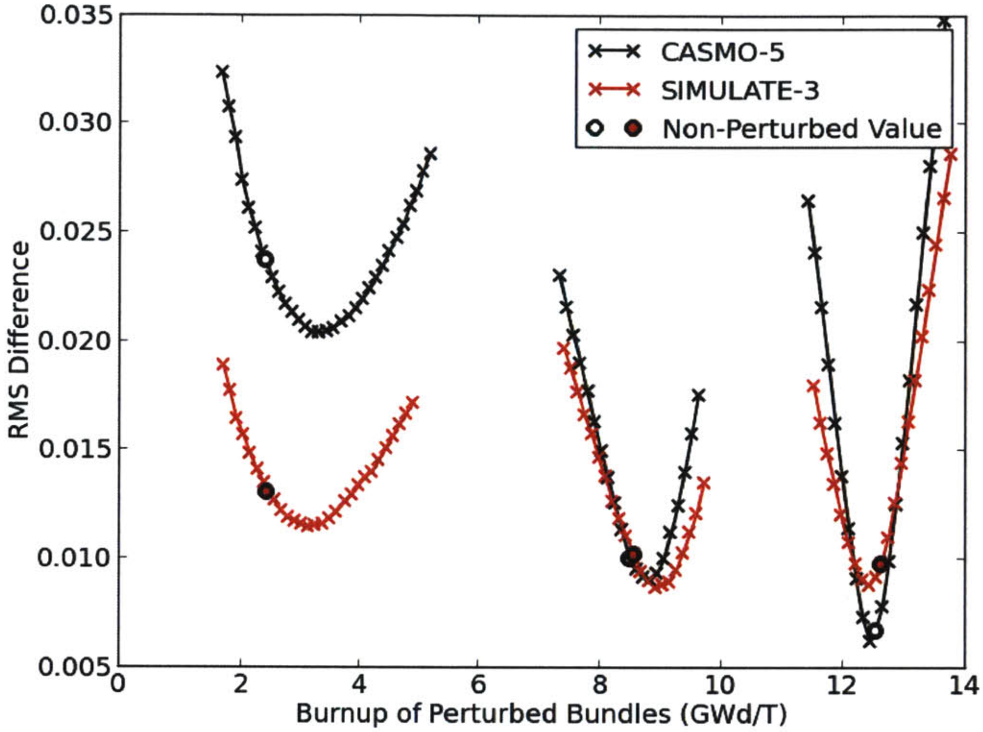

Figure 5-4: Root mean square (RMS) error in fission rate distribution as a function of perturbed fuel batch burnup for 2.4% enriched fuel in cycle 1.

significant improvement in the RMS error can be realized by significantly altering the reactivity in the 3.1% enriched fuel.

The last perturbation set combines 2.4% and 3.1% enriched fuel. In particular, the burnup of 3.1% enriched fuel is set to that which produces the minimum RMS shown in Fig. 5-5 and the burnup of the 2.4% enriched fuel is perturbed. The intuition is to first perturb the 3.1% enriched fuel to correct the in-out tilt, then perturb the 2.4% enriched fuel to correct internal errors. The resulting trends are shown in Fig. 5-6.

Since the perturbation of 3.1% fuel significantly changes the distribution, not much improvement can be obtained by perturbing the 2.4% enriched fuel.

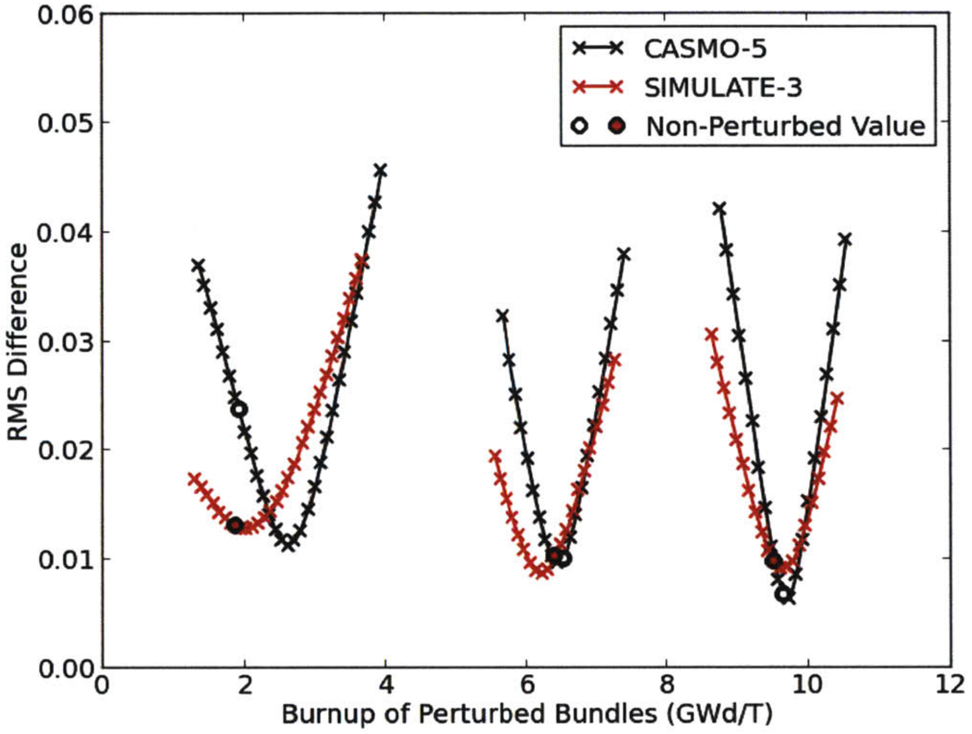

Figure 5-5: Root mean square (RMS) error in fission rate distribution as a function of perturbed fuel batch burnup for 3.1% enriched fuel in cycle 1.

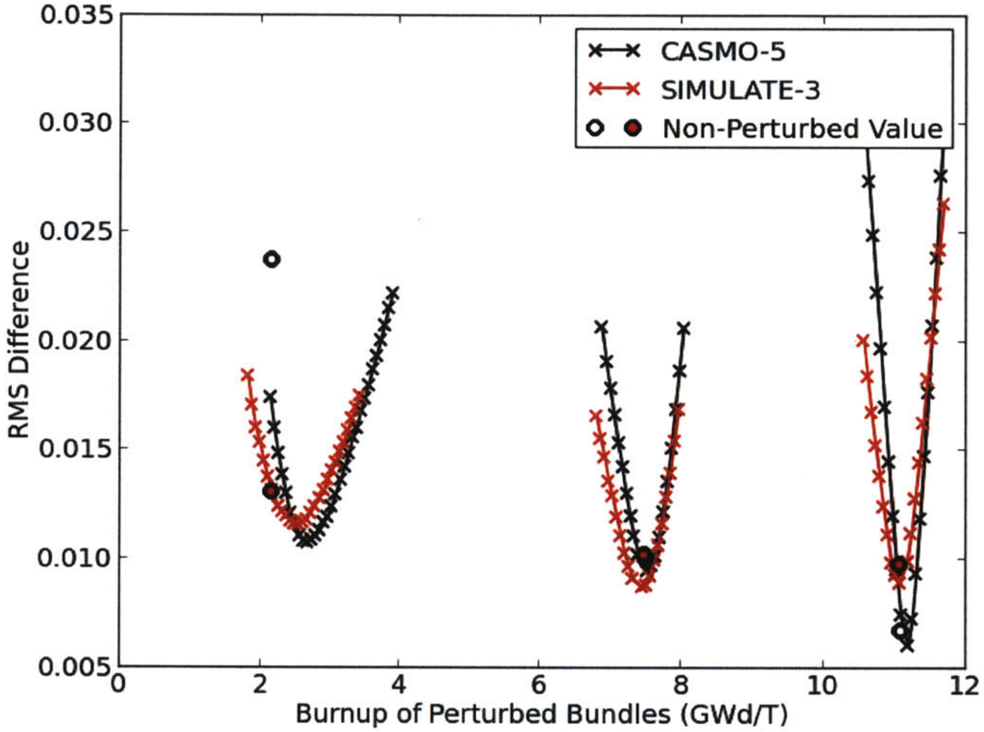

Figure 5-6: Root mean square (RMS) error in fission rate distribution as a function of perturbed fuel batch burnup for 2.4% enriched fuel with 3.1% enriched fuel burnup at its isolated minimum RMS error in cycle 1. Note that the unperturbed points are not necessarily connected to the curve as the perturbation of 3.1% fuel has already decreased the error, moving the computed curves to lower RMS values.

5.2.2 Cycle 2 Results

In cycle 2, we perform a similar investigation. Cycle 2 is shorter than cycle 1, but the burnup steps are once again chosen to reflect beginning, middle, and end of cycle. The chosen cycle burnup steps are 2.11, 5.23, and 9.35 GWd/T. Once again, our first sub-batch candidate is the reloaded 2.4% enriched fuel from cycle 1 which is spread throughout the core but with some fuel assemblies placed on the periphery. The results of perturbing burnup on this sub-batch are shown in Fig. 5-7. Once again, the CASMO-5 and SIMULATE-3 perturbations are in the same direction and similar in magnitude.

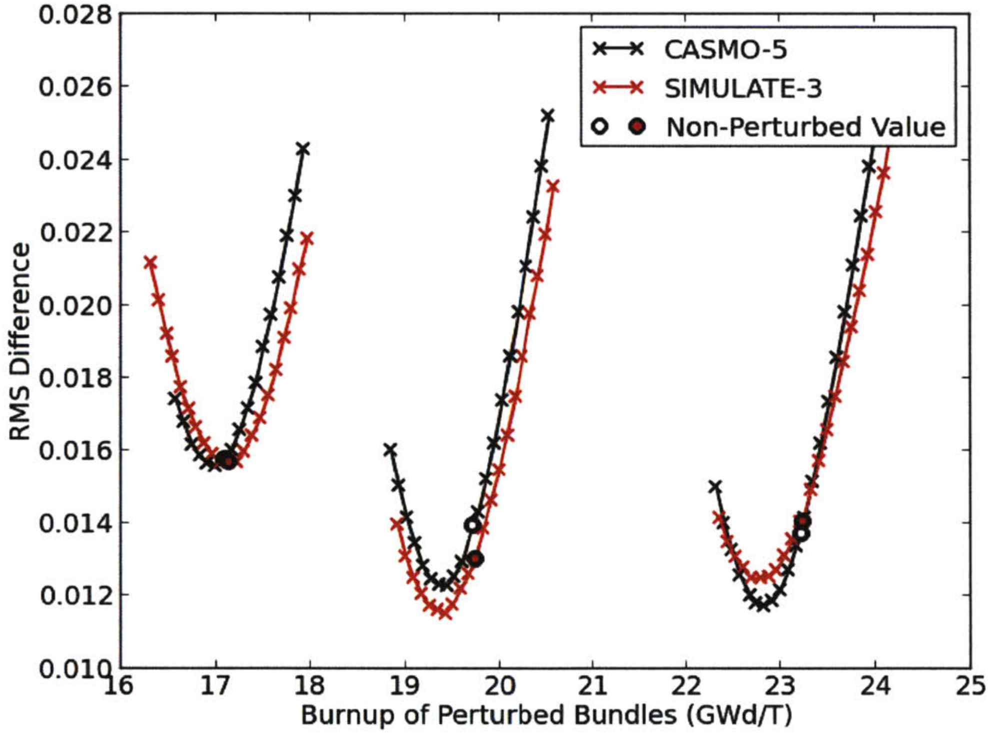

Figure 5-7: Root mean square (RMS) error in fission rate distribution as a function of perturbed fuel batch burnup for reloaded 2.4% enriched fuel in cycle 2.

Just as in cycle 1, the next sub-batch candidate is the reloaded 3.1% enriched fuel. This fuel is largely grouped together near the center of the core with additional groups ranging further from the center. This is an important difference with the cycle 1 perturbations and the cycle 2 perturbations of 2.4% enriched fuel. Those sub-batches were largely checkered and did not have large groups clustered together. The results of perturbing the burnup of the reloaded 3.1% enriched fuel are shown in Fig. 5-8.

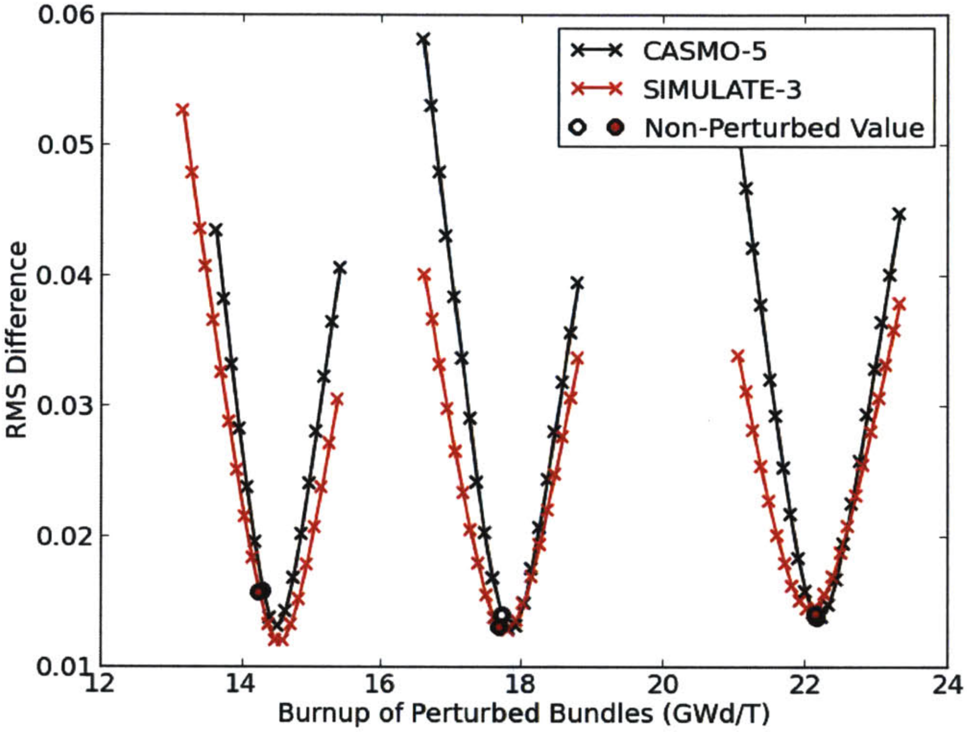

Figure 5-8: Root mean square (RMS) error in fission rate distribution as a function of perturbed fuel batch burnup for reloaded 3.1% enriched fuel in cycle 2.

Note that the gradient of the RMS curve is very steep. This is due to the fuel assemblies in the sub-batch being clustered. A small perturbation to clustered fuel will have a large perturbation on the fission rates within that region.

The last sub-batch is the fresh fuel with enrichments of 3.2% and 3.4%. This fuel is loaded primarily near the periphery of the reactor core. The results are presented in Fig. 5-9 showing very little room for improving the RMS error through perturbation of the fuel even though the core is very sensitive to the fuel sub-batch reactivity.

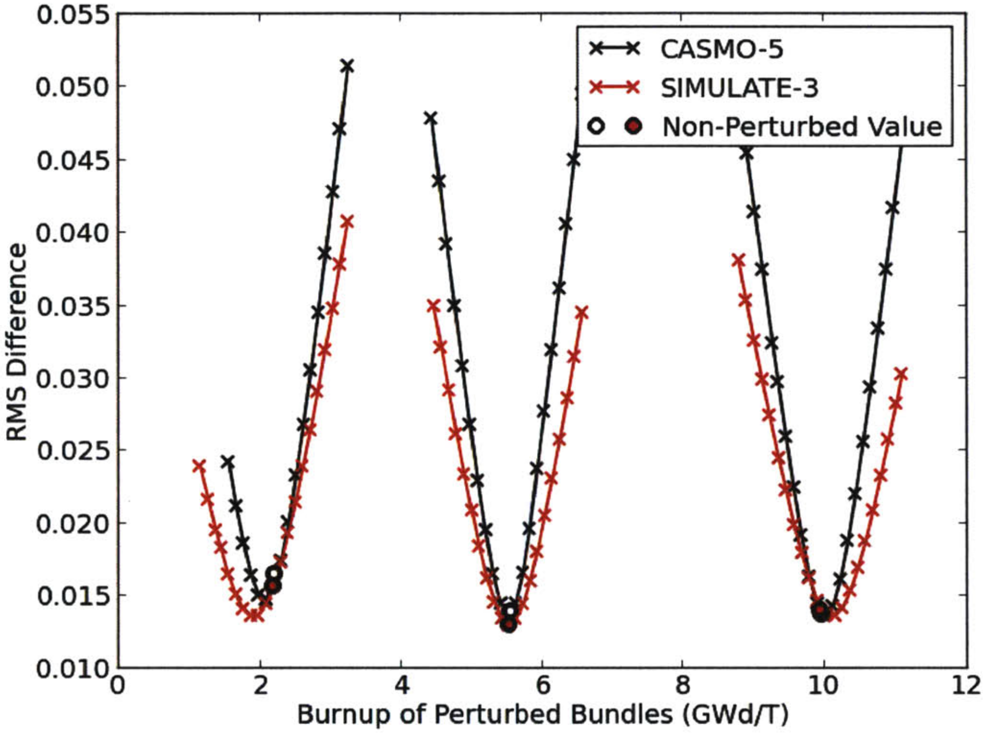

Figure 5-9: Root mean square (RMS) error in fission rate distribution as a function of perturbed fuel batch burnup for fresh fuel in cycle 2.

5.3 Calculated Reactivity Decrements

Using the reactivity gradients from the lattice physics calculations and the results gathered for the optimal sub-batch burnup distribution in section 5.2 for cycles 1 and 2, the bias in reactivity decrement can be calculated using Eq. 5.1. These results are summarized in Table 5.1 for all the perturbation sets tested.

Table 5.1: Inferred CASMO-5 M×N Fuel Batch Reactivity Bias in Comparison with SIMULATE-3

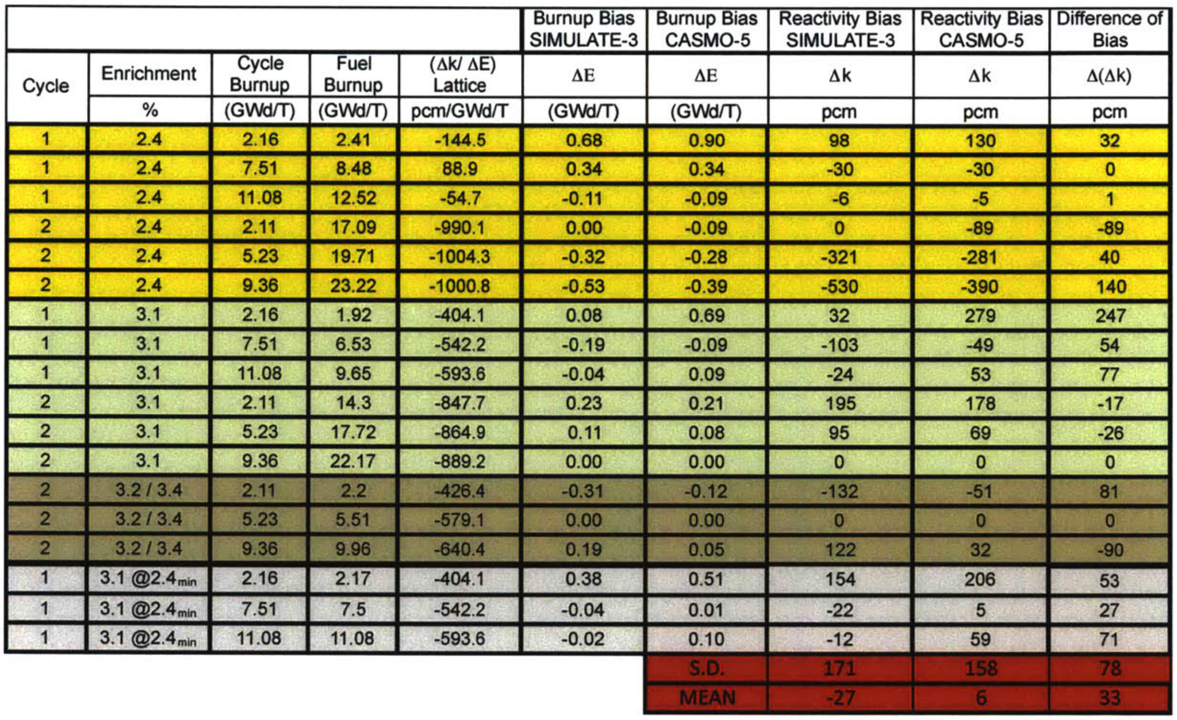

					Burnup Bias SIMULATE-3	Burnup Bias CASMO-5	Reactivity Bias SIMULATE-3	Reactivity Bias CASMO-5	Difference of Bias
Cycle	Enrichment	Cycle Burnup	Fuel Burnup	$(\Delta k/ \Delta E)$ Lattice	ΔE	ΔE	Δk	Δk	$\Delta(\Delta k)$
	%	(GWd/T)	(GWd/T)	pcm/GWd/T	(GWd/T)	(GWd/T)	pcm	pcm	pcm
1	2.4	2.16	2.41	-144.5	0.68	0.90	98	130	32
1	2.4	7.51	8.48	88.9	0.34	0.34	-30	-30	0
1	2.4	11.08	12.52	-54.7	-0.11	-0.09	-6	-5	1
2	2.4	2.11	17.09	-990.1	0.00	-0.09	0	-89	-89
2	2.4	5.23	19.71	-1004.3	-0.32	-0.28	-321	-281	40
2	2.4	9.36	23.22	-1000.8	-0.53	-0.39	-530	-390	140
1	3.1	2.16	1.92	-404.1	0.08	0.69	32	279	247
1	3.1	7.51	6.53	-542.2	-0.19	-0.09	-103	-49	54
1	3.1	11.08	9.65	-593.6	-0.04	0.09	-24	53	77
2	3.1	2.11	14.3	-847.7	0.23	0.21	195	178	-17
2	3.1	5.23	17.72	-864.9	0.11	0.08	95	69	-26
2	3.1	9.36	22.17	-889.2	0.00	0.00	0	0	0
2	3.2 / 3.4	2.11	2.2	-426.4	-0.31	-0.12	-132	-51	81
2	3.2 / 3.4	5.23	5.51	-579.1	0.00	0.00	0	0	0
2	3.2 / 3.4	9.36	9.96	-640.4	0.19	0.05	122	32	-90
1	3.1 @2.4$_{min}$	2.16	2.17	-404.1	0.38	0.51	154	206	53
1	3.1 @2.4$_{min}$	7.51	7.5	-542.2	-0.04	0.01	-22	5	27
1	3.1 @2.4$_{min}$	11.08	11.08	-593.6	-0.02	0.10	-12	59	71
						S.D.	171	158	78
						MEAN	-27	6	33

Results show the predictions of reactivity decrement for SIMULATE-3 and CASMO-5 are similar. The maximum difference in reactivity decrement between SIMULATE-3 and CASMO-5 is less than 250 pcm. Moreover, the standard deviation of the difference between SIMULATE-3 and CASMO-5 is 78 pcm. Notice the reactivity bias produced when avaeraged accross all cases is lower for CASMO-5. In addition the deviation in reactivity bias across all cases is also lower for CASMO-5. This study focused on low burnup data since all cases fall within the range of 2.0 GWd/T to 23.0 GWd/T.

Chapter 6

Summary

6.1 Conclusions

The results of this investigation demonstrate that the inferred reactivity decrement errors using 2D full-core transport methods are slightly smaller than those inferred from analogous nodal diffusion methods. However, the difference in reactivity errors are very similar as all calculations yielded differences of less than 250 pcm. The most important outcome of this study is that nodal method approximations have now been demonstrated to contribute insignificantly to individual batch reactivity errors. Consequently, nodal methods do not contribute significantly to inferred reactivity decrement biases and uncertainties.

The original EPRI/Studsvik report [2] which formed the basis for much of this work relied on SIMULATE-3 3D nodal diffusion models. Ideally, 3D transport models would be used to verify the reliability of 3D nodal diffusion models with respect to the accuracy of reactivity decrement calculations. However, 3D transport models are currently infeasible for such an investigation. Therefore, in this report we focused on the comparison of 2D models - both nodal diffusion and transport. We expect that since the 2D models were comparable, we would observe similar behavior in a comparison of 3D nodal diffusion with 3D transport as the underlying physical assumptions are the same.

The EPRI/Studsvik report postulated errors in reactor models arising from a variety of sources. Two of these sources were differences in batch spectra relative to the CASMO lattice assumption of zero leakage and differences in intra-assembly spatial flux distributions relative to the lattice assumption. The full-core transport solution demonstrated in this investigation (CASMO-5 M×N) does not incorporate such assumptions. These two potential sources of error can now be eliminated since they are only present in nodal solutions.

Three additional sources of error cited in the report involved SIMULATE-3 physics model assumptions. In particular, potential errors in nodal and detector physics models, potential errors in cross section data fitting models, and the approximation of homogenized fuel assemblies were cited. These sources can also be eliminated from consideration since there are no such approximations in the full-core transport solution.

Remaining sources of modeling errors and sources of reactivity decrement biases and uncertainties are:

1. Errors in fundamental neutron cross section data

2. Errors in CASMO-5 computed nuclide inventory vs. fuel burnup

3. Imperfect knowledge of reactor operating power history

4. Imprecision in iterative analysis method, particularly for low sensitivity batches

Results of this study further substantiate the previous EPRI/Studsvik study's assertion that the Kopp Memo 5% reactivity decrement uncertainty assumption, often applied in Spent Fuel Pool criticality analysis, is both valid and conservative for cold SFP reactivities computed with CASMO-5.

6.2 Future Work

6.2.1 Improved Thermal Hydraulic Modeling in an MOC Solver

Due to the lack of a thermal hydraulic feedback model in CASMO-5 M×N, temperatures were extracted from SIMULATE-3 output. For improved accuracy and less dependence on SIMULATE-3 results, a sub-channel thermal hydraulic feedback model and a pin-wise fuel temperature feedback model should be implemented directly in an MOC code. The more direct thermal hydraulic modeling would allow for accurate MOC results. In addition, the results between SIMULATE-3 and CASMO-5 M×N would be more independent.

6.2.2 Investigate Different Methods for Perturbing Sub-batch Reactivity

In the investigation presented here, fuel burnup was perturbed to alter the sub-batch reactivity. The difference of computed results relative to measured data was used to infer fuel reactivity. However, there are other ways of perturbing reactivity. For instance, fuel temperatures could be perturbed instead of burnup. This is particularly advantageous for fuel assemblies with burnable poison pins at low burnup where the competing reactivity effects of fuel depletion and burnable poison depletion cause burnup perturbations to be less effective.

6.2.3 3D Comparison of Nodal and Transport Methods

Early in this study the decision was made to evaluate 2D nodal methods against 2D transport methods. While 3D modeling is certainly more accurate, 2D modeling was chosen due to the computational burden of 3D transport methods. However, if a 3D transport method algorithm can be shown to be less computationally cumbersome a much more accurate comparison of nodal approximations could be conducted. This could be a 3D MOC solver or even a 3D Monte Carlo solver. However, the 3D transport algorithm would need to solve approximately 600 full-core statepoint calculations in a reasonable time frame for a proper investigation.

Appendix A

Additional Cycle 1 HZP Fission Rate Error Maps

This section provides additional fission rate error maps relative to measured data without any linear correction.

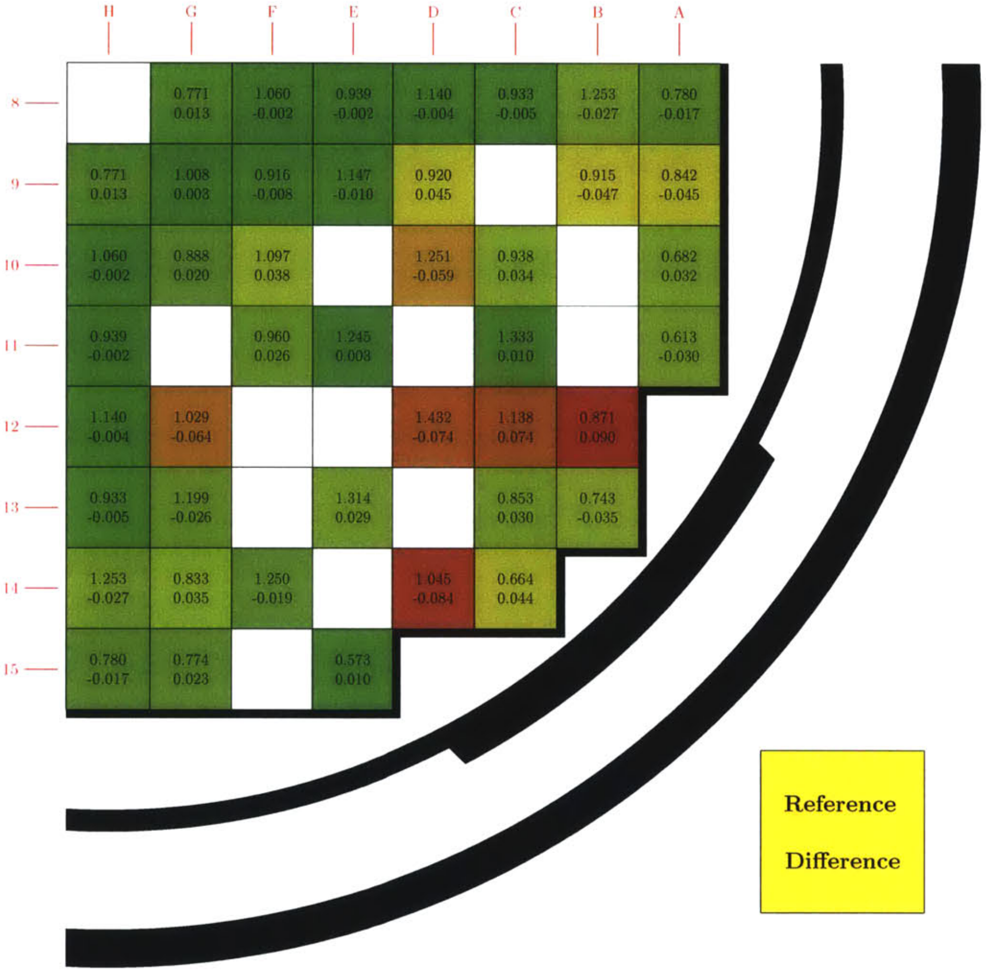

	H	G	F	E	D	C	B	A
8		0.771 0.013	1.060 -0.002	0.939 -0.002	1.140 -0.004	0.933 -0.005	1.253 -0.027	0.780 -0.017
9	0.771 0.013	1.008 0.003	0.916 -0.008	1.147 -0.010	0.920 0.045		0.915 -0.047	0.842 -0.045
10	1.060 -0.002	0.888 0.020	1.097 0.038		1.251 -0.059	0.938 0.034		0.682 0.032
11	0.939 -0.002		0.960 0.026	1.245 0.003		1.333 0.010		0.613 -0.030
12	1.140 -0.004	1.029 -0.064			1.432 -0.074	1.138 0.074	0.871 0.090	
13	0.933 -0.005	1.199 -0.026		1.314 0.029		0.853 0.030	0.743 -0.035	
14	1.253 -0.027	0.833 0.035	1.250 -0.019		1.045 -0.084	0.664 0.044		
15	0.780 -0.017	0.774 0.023		0.573 0.010				

Figure A-1: Difference in reaction rates of the SIMULATE-3 3D ARO model relative to measured data at hot zero power (HZP) conditions in cycle 1. The RMS error is 0.0362.

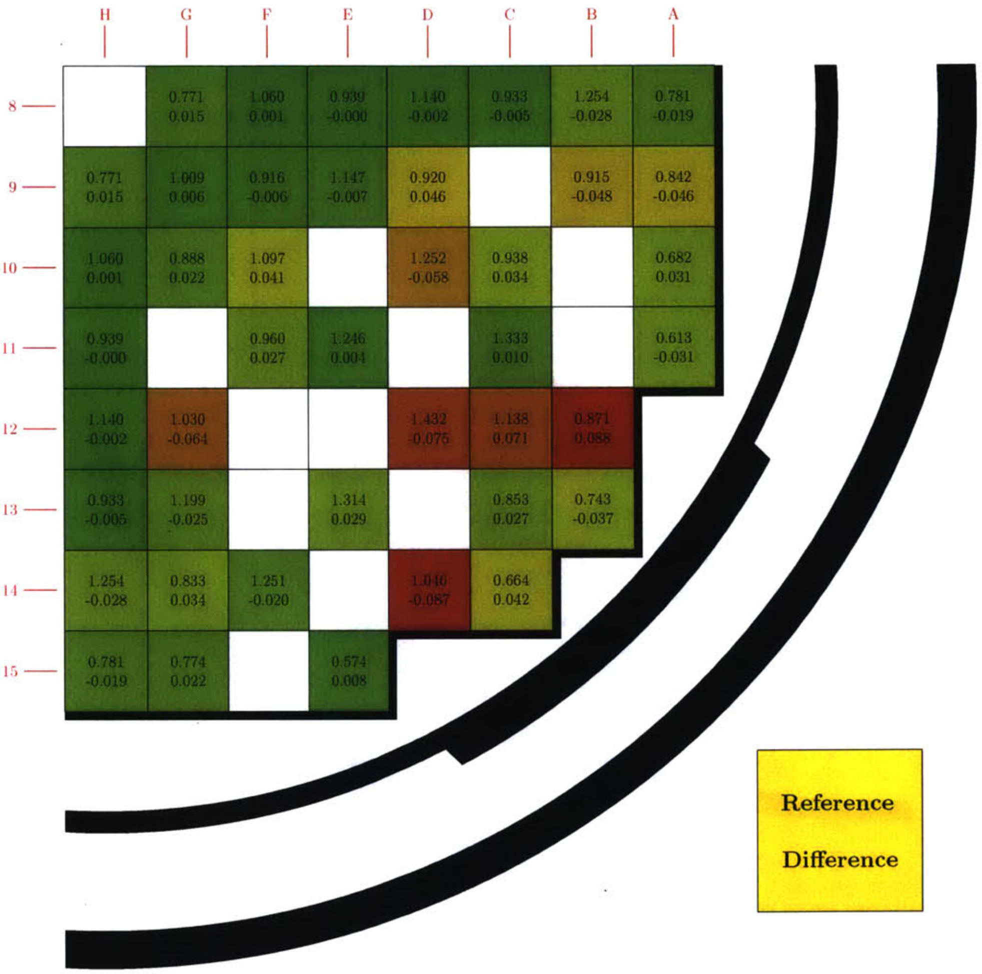

	H	G	F	E	D	C	B	A
8		0.771 0.015	1.060 0.001	0.939 -0.000	1.140 -0.002	0.933 -0.005	1.254 -0.028	0.781 -0.019
9	0.771 0.015	1.009 0.006	0.916 -0.006	1.147 -0.007	0.920 0.046		0.915 -0.048	0.842 -0.046
10	1.060 0.001	0.888 0.022	1.097 0.041		1.252 -0.058	0.938 0.034		0.682 0.031
11	0.939 -0.000		0.960 0.027	1.246 0.004		1.333 0.010		0.613 -0.031
12	1.140 -0.002	1.030 -0.064			1.432 -0.075	1.138 0.071	0.871 0.088	
13	0.933 -0.005	1.199 -0.025		1.314 0.029		0.853 0.027	0.743 -0.037	
14	1.254 -0.028	0.833 0.034	1.251 -0.020		1.046 -0.087	0.664 0.042		
15	0.781 -0.019	0.774 0.022		0.574 0.008				

Figure A-2: Difference in reaction rates of the SIMULATE-3 2D model relative to measured data at hot zero power (HZP) conditions in cycle 1. The RMS error is 0.0361.

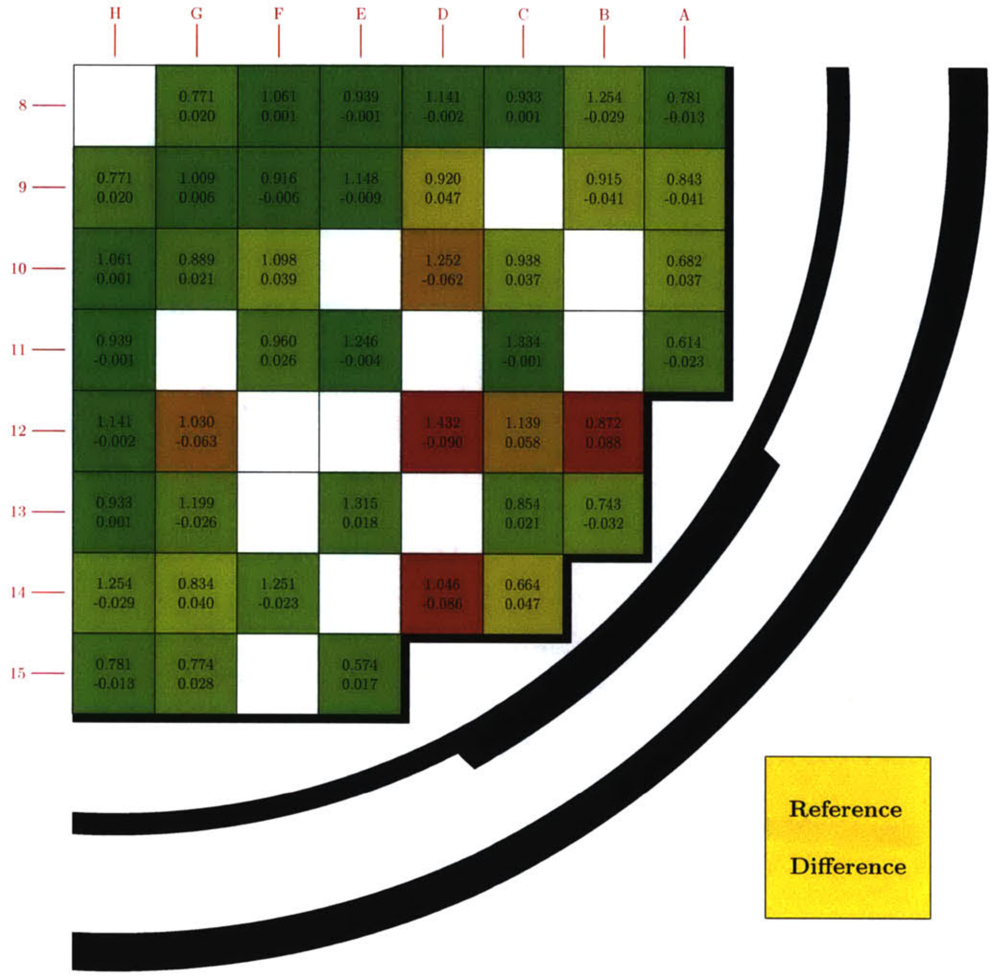

	H	G	F	E	D	C	B	A
8		0.771 0.020	1.061 0.001	0.939 -0.001	1.141 -0.002	0.933 0.001	1.254 -0.029	0.781 -0.013
9	0.771 0.020	1.009 0.006	0.916 -0.006	1.148 -0.009	0.920 0.047		0.915 -0.041	0.843 -0.041
10	1.061 0.001	0.889 0.021	1.098 0.039		1.252 -0.062	0.938 0.037		0.682 0.037
11	0.939 -0.001		0.960 0.026	1.246 -0.004		1.334 -0.001		0.614 -0.023
12	1.141 -0.002	1.030 -0.063			1.432 -0.090	1.139 0.058	0.872 0.088	
13	0.933 0.001	1.199 -0.026		1.315 0.018		0.854 0.021	0.743 -0.032	
14	1.254 -0.029	0.834 0.040	1.251 -0.023		1.046 -0.086	0.664 0.047		
15	0.781 -0.013	0.774 0.028		0.574 0.017				

Figure A-3: Difference in reaction rates of the CASMO-5 M×N model relative to measured data at hot zero power (HZP) conditions in cycle 1. The RMS error is 0.0364.

Appendix B

Additional Cycle 1 HFP Fission Rate Error Maps

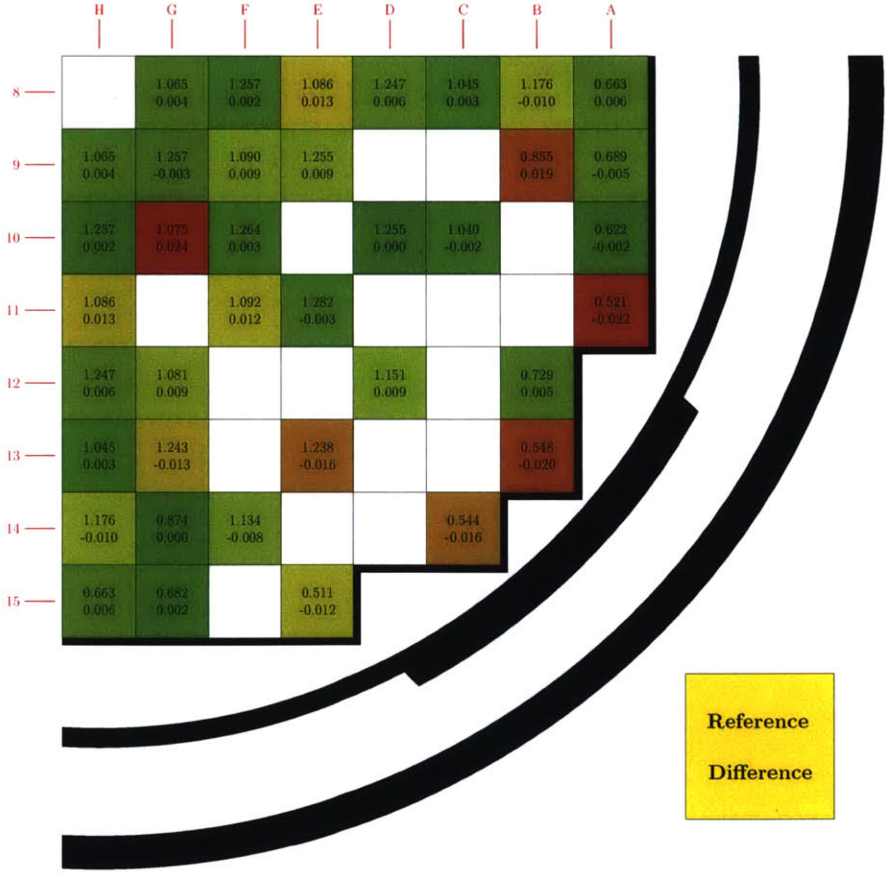

	H	G	F	E	D	C	B	A
8		1.065 0.004	1.257 0.002	1.086 0.013	1.247 0.006	1.045 0.003	1.176 -0.010	0.663 0.006
9	1.065 0.004	1.257 -0.003	1.090 0.009	1.255 0.009			0.855 0.019	0.689 -0.005
10	1.257 0.002	1.075 0.024	1.264 0.003		1.255 0.000	1.040 -0.002		0.622 -0.002
11	1.086 0.013		1.092 0.012	1.282 -0.003				0.521 -0.022
12	1.247 0.006	1.081 0.009			1.151 0.009		0.729 0.005	
13	1.045 0.003	1.243 -0.013		1.238 -0.016			0.548 -0.020	
14	1.176 -0.010	0.874 0.000	1.134 -0.008			0.544 -0.016		
15	0.663 0.006	0.682 0.002		0.511 -0.012				

Figure B-1: Difference in SIMULATE-3 2D model reaction rates relative to measured data at 7.51 GWd/T exposure in cycle 1. The RMS error is 0.0102.

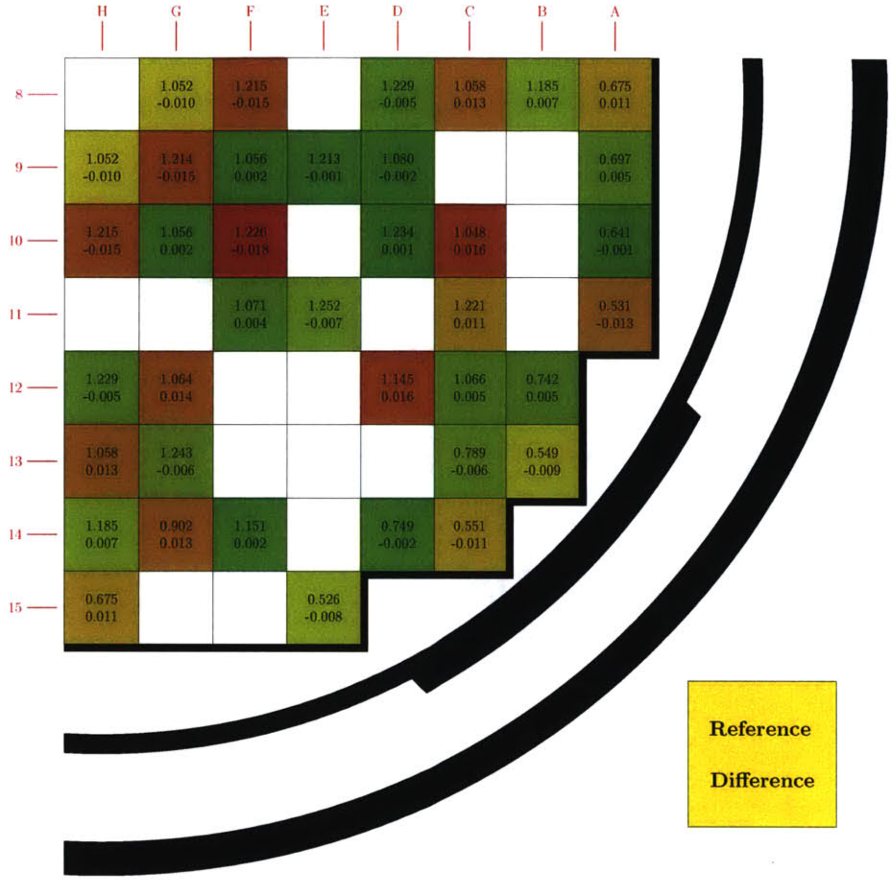

	H	G	F	E	D	C	B	A
8		1.052 -0.010	1.215 -0.015		1.229 -0.005	1.058 0.013	1.185 0.007	0.675 0.011
9	1.052 -0.010	1.214 -0.015	1.056 0.002	1.213 -0.001	1.080 -0.002			0.697 0.005
10	1.215 -0.015	1.056 0.002	1.220 -0.018		1.234 0.001	1.048 0.016		0.641 -0.001
11			1.071 0.004	1.252 -0.007		1.221 0.011		0.531 -0.013
12	1.229 -0.005	1.064 0.014			1.145 0.016	1.066 0.005	0.742 0.005	
13	1.058 0.013	1.243 -0.006				0.789 -0.006	0.549 -0.009	
14	1.185 0.007	0.902 0.013	1.151 0.002		0.749 -0.002	0.551 -0.011		
15	0.675 0.011			0.526 -0.008				

Figure B-2: Difference in SIMULATE-3 2D model reaction rates relative to measured data at 11.08 GWd/T exposure in cycle 1. The RMS error is 0.0097.

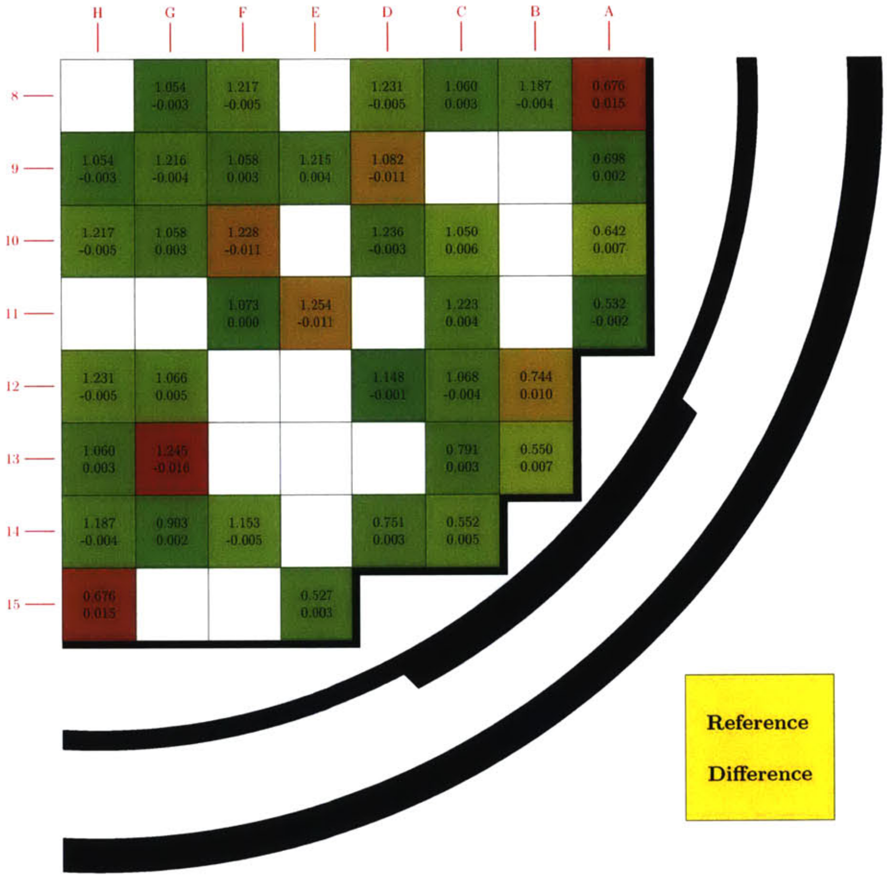

	H	G	F	E	D	C	B	A
8		1.054 -0.003	1.217 -0.005		1.231 -0.005	1.060 0.003	1.187 -0.004	0.676 0.015
9	1.054 -0.003	1.216 -0.004	1.058 0.003	1.215 0.004	1.082 -0.011			0.698 0.002
10	1.217 -0.005	1.058 0.003	1.228 -0.011		1.236 -0.003	1.050 0.006		0.642 0.007
11			1.073 0.000	1.254 -0.011		1.223 0.004		0.532 -0.002
12	1.231 -0.005	1.066 0.005			1.148 -0.001	1.068 -0.004	0.744 0.010	
13	1.060 0.003	1.245 -0.016				0.791 0.003	0.550 0.007	
14	1.187 -0.004	0.903 0.002	1.153 -0.005		0.751 0.003	0.552 0.005		
15	0.676 0.015			0.527 0.003				

Reference

Difference

Figure B-3: Difference in CASMO-5 M×N model reaction rates relative to measured data at 11.08 GWd/T exposure in cycle 1. The RMS error is 0.0067.

Bibliography

[1] L. Kopp, NRC memorandum from L. Kopp to T. Collins, "Guidance on the Regulatory Requirements for Criticality Analysis of Fuel Storage at Light-Water Reactor Power Plants," (ADAMS Accession No. ML003728001), dated August 19, (1998).

[2] K. Smith, et al, "Benchmarks for Quantifying Fuel Reactivity Depletion Uncertainty," EPRI, Palo Alto, CA, Technical Report Number 1022909 (2011).

[3] Boyd, William. "Massively Parallel Algorithms for Method of Characteristics Neutral Particle Transport on Shared Memory Computer Architectures." Master's thesis, Massachusetts Institute of Technology, 2014.

[4] J. L. Eller, Letter, "Reference: Fuel, Core, and Operational Data to Support Core Physics Benchmark Analyses," DPC-1553.05.00.0222, Rev 0, March (2011).

[5] J. Rhodes, et al., "CASMO-5 Development and Applications," PHYSOR-2006, Vancouver, BC, Canada. September 10-14, (2006)

[6] J. Cronin, et al., "SIMULATE-3 Methodology Manual," STUDSVIK/SOA-95/18, Studsvik of America, Inc. (1995).

[7] N. Horelik, B. Herman, B. Forget, and K. Smith. "Benchmark for Evaluation and Validation of Reactor Simulations (BEAVRS), v1.0.1," Proc. Int. Conf. Mathematics and Computational Methods Applied to Nuc. Sci. & Eng., Sun Valley, Idaho, (May 2013).

[8] D. Hagrman, et al., "INTERPIN-4 Model Improvements and Verification," SSP-07/445 Rev 0, Studsvik Scandpower, Inc. (2007).

[9] T. Bahadir, et al., "CMSLINK User's Manual," STUDSVIK/SOA-97/04, Studsvik of America, Inc. (1997).

[10] K. Smith, "Topical Report on Studsvik's Core Management System (CMS)," SSP-09/477-C, Rev 0, Studsvik Scandpower, Inc. (2010).

[11] A. Yamamoto, et al, "Derivation of optimum polar angle quadrature set for the method of characteristics based on approximation error for the Bickley function" (2007) Journal of Nuclear Science and Technology, 44 (2) , pp. 129-136.

[12] D. Kelly, et al, "Analysis of select PWR benchmark cycle 1 results using MC21 and OpenMC," *in Proc. Int. Conf. on the Reactor Physics, PHYSOR 2014*, Kyoto, Japan, (September 2014).

[13] Los Alamos National Laboratory report LA-UR-12-27079 (Dec 2012). Original Author: R. E. MacFarlane, Contributing Authors: D. W. Muir, R. M. Boicourt, A. C. Kahler, Current Editor: A. C. Kahler.

[14] Lawrence, R. D. "Three-Dimensional Nodal Diffusion and Transport Methods for the Analysis of Fast-Reactor Critical Experiments." International Seminar Finite Element and Allied Methods for Reactor Physics and Shielding Calculations. London, England 1986.

[15] Smith, K. S. "Spatial Homogenization Methods for Light Water Reactor Analysis." Doctoral dissertation, Massachusetts Institute of Technology, 1980.